UNIVERSITY OF CAPE TOWN
IYUNIVESITHI YASEKAPA • UNIVERSITEIT VAN KAAPSTAD

MECHANICAL CHARACTERISATION OF FLOAT AND LAMINATED GLASS

ADEBOWALE EBENEZER ADENIRAN

Supervisor:
Mr. Sa-aadat Parker

Thesis presented for the Degree of
Master of Science
in the Department of Mechanical Engineering
Faculty of Engineering and the Built Environment
University of Cape Town

Blast Impact and Survivability Research Unit
Department of Mechanical Engineering
University of Cape Town

Declaration

I, Adebowale Ebenezer Adeniran , hereby:

(a) grants the University of Cape Town a free license to reproduce the above thesis in whole or in part, for the purpose of research;

(b) declare that:

  (i) the above thesis is my unaided work, both in concept and execution and apart from the normal guidance from my supervisor, I have received no assistance apart from that explicitly stated in the Acknowledgements.

  (ii) neither the substance nor any part of the above thesis has been submitted in the past, or is being, or is to be submitted for a degree at this University or any other university.

I am now presenting the report for examination for the degree of MSc Eng (Mechanical).

Adebowale Adeniran

20 January, 2025

Abstract

In recent years, glass has experienced growth in its application within engineering and architecture, especially for structural applications [1]. It has been used as various components such as balcony walls, staircases, floors, roofs, and façades. As demand for secure and safe construction continues to grow, there is an increasing interest in the mechanical characterisation of glass, particularly laminated glass (LG) and float glass (FG), which are the most commonly used types in various applications. Despite its growth, the understanding of the structural behaviour of glass and mechanical properties is still not as advanced as that of other construction materials like concrete, steel, and wood [2]. During production, glass undergoes several processes, including melting of raw materials, annealing, cutting, and transportation. These processes introduce micro-flaws on the edges and surfaces of the glass. Also, the exposure of glass to mechanical stress, temperature fluctuations, impacts, or improper handling and installation further contributes to the formation of these micro-flaws [3, 4]. The quantity of these micro-flaws often depends on the geometry of the glass and plays an essential role in evaluating glass failure stress, which ultimately affects its structural integrity and safety.

The fracture strength of glass materials is highly sensitive to micro-flaws, which act as stress concentrators and initiate cracks [5]. For a given flaw density, as the volume increases, the number of flaws, and, in particular, the number of flaws of critical length, increases [6]. This gives rise to the size effect, where the fracture strength of the specimen will decrease as the size of the specimen increases [7]. The study is set to determine the influence of the size of the loading span on the fracture strength of FG and LG when subjected to the four-point bend test (FPBT) and the ring-on-ring (ROR) test. This will aid in developing guidelines that account for size effects in structural design, ensuring safer and more reliable use of glass materials in engineering and architectural applications. The FPBT setup strictly adhered to ASTM C158-02 guidelines, while the ROR test followed ASTM C1499-19 standards.

The tests reveal that both FG and LG demonstrate elastic behaviour with no plastic deformation, and mainly fail through brittle fracture. In both the FPBT and ROR tests, it is observed that the fracture strength of FG and LG is higher with smaller loading spans compared to larger loading spans. Additionally, the ROR results show more variability than the FPBT results. The study reveals that the Weibull distribution is suitable for describing the fracture strength of glass materials under stress. Moreover, the experimental fracture strengths were calculated analytically and confirmed using finite element analysis (FEA). The study provides important information about the performance and reliability of both FG and LG in real-world applications, especially in construction and automotive industries where durability and safety are paramount.

Acknowledgements

My sincere gratitude goes to my supervisor, Mr. Sa-aadat Parker, for his constant support, guidance, and motivation, which were inspirations throughout my MSc journey. His mentorship has inspired me and also brightened my path with invaluable insights. The profound impact of his teachings will remain with me for the rest of my life. I am deeply thankful for the opportunity to benefit from his vast knowledge and expertise, which will continue to enhance my academic endeavours.

Also, I want to thank all the members of my esteemed research group, Blast Impact and Survivability Research Unit (BISRU) as well as the entire academic and non-academic staff in the Mechanical Engineering Department. Their motivation and opportunities for learning have been instrumental in my academic growth. I extend special thanks to Malcolm and Matthew for their guidance with SolidWorks software, and to Penny Louw, the Senior Technical Officer at the Centre for Materials Engineering (CME), for her generous support and guidance in using the Zwick machine at the CME lab. My heartfelt appreciation also goes to the MasterCard Foundation for their generous scholarship, which has made my master's degree journey possible. I am grateful to my mentor, Dr. Omisakin Ayomide, for his support and contribution to my success in life.

My time at the University of Cape Town was made memorable by the harmony of colleagues, and excellent minds who provided support. Special thanks to Abiodun, Emmanuel, Ajibola, Modupe, Mr Samson Fatukasi, Mr Raymond, pastor Okafor and Mr Tanimu for transforming the University of Cape Town into another home for me.

To my parents, Mr. and Mrs. Abraham and Deborah Adeniran, I am deeply grateful for your endless prayers, encouragement, and understanding from the start to the end of my MSc journey. Also, I want to express gratitude to my siblings - my two elder sisters, Julianna Adedokun and Rebecca Olanrewaju, and my younger brother and sister, Taiwo and Kehinde Adeniran, for their constant prayers and support. Special appreciation goes to my lovely wife, Olaide Adeniran, and my amazing gift from God, Oluwafiirefunmi Adeniran, for their prayers, support and understanding during this period.

To the Folorunso family, friends, and loved ones who have checked in on me and offered their prayers and support, I am truly grateful for your kindness and encouragement.

Contents

List of Figures

List of Tables

Chapter 1

Introduction

This report provides an analysis of the mechanical characterisation of glass. The purpose is to improve our understanding of fracture strength associated with float glass (FG) and laminated glass (LG). The introductory section of this report contains background information, the problem statement, research objectives, the significance of the study, and any limitations that may apply.

1.1 Background Information

Glass has become more widely used in engineering and architecture, particularly in structural applications [1]. It has been utilised for balcony walls, staircases, floors, roofs, and façades, as shown in Figure 1.1. The understanding of how glass behaves structurally is not as developed as it is for other structural materials such as concrete, steel and wood [2]. Glass undergoes several processes during both production and post-production stages, such as melting raw materials, annealing, cutting, and transportation. These processes introduce micro-flaws into the glass. Also, exposure of glass to mechanical stress, excessive temperature differentials, impact, or improper handling and installation further generates micro-flaws on the edges and surface of the glass [3, 4]. The micro-flaws may not be visible to the naked eye but are the source of weakness in glass, which leads to further cracking or breakage over time [3, 8]. This overall affects the structural integrity and safety of the glass structure.

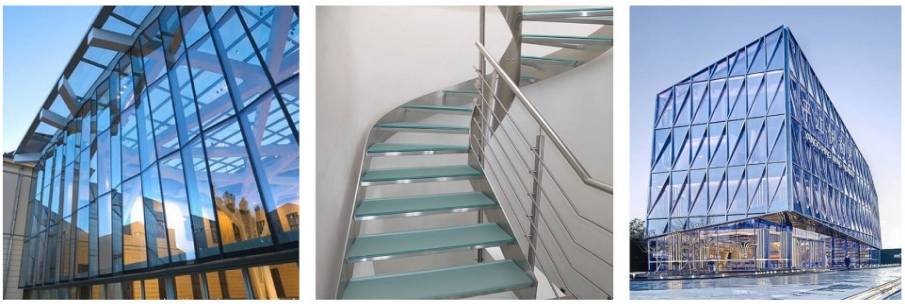

Figure 1.1 Structural components in buildings made of laminated glass [9]

Glass, being a brittle material, fails catastrophically when it fractures [10]. Glass that has not been heat-treated shatters into long, sharp shards, which can cause serious injuries.

whereas, tempered glass, which is heat-treated to increase its strength by inducing surface compressive stresses to close micro-flaws, breaks into smaller, blunt, rounded pieces, thereby reducing the risk of harm [11, 12]. Also, laminated glass, consisting of two or more glass panes fused together by one or more polymer interlayers, shown in Figure 1.2, retains its structural integrity when fractured [1, 13]. The interlayer, typically an elastomeric polymer, serves as a safety feature [14], holding the glass fragments in place, preventing them from becoming hazardous and minimising the risk of injury from flying shards [1, 13]. Figure 1.3 illustrates this effect, showing a broken car windshield where the interlayer has prevented the glass fragments from becoming projectiles.

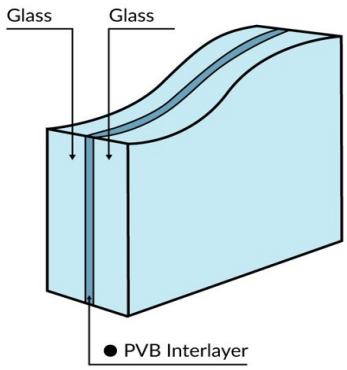

Figure 1.2 Image of laminated glass [13]

As shown in Figure 1.2, the PVB (polyvinyl butyral) interlayer is an elastomeric polymer that provides both adhesion and flexibility, allowing the glass to retain its structural integrity after cracking.

Figure 1.3 Broken windscreen of a car [13]

1.1.1 Application of Laminated Glass

The use of glass has been successfully employed in the construction sector. Figure 1.4a displays the longest glass bridge in China, which is 526 meters long and was opened in 2017 [15]. Figure 1.4b shows the complete glass structure of the Apple store in China. Organisations like the Occupational Safety and Health Administration (OSHA) mandates

the usage of LG in potentially hazardous situations to prevent people from being injured by shards of glass [16].

a. China's longest glass bridge [15]

b. structure made completely of glass (Apple store, located in Shanghai) [17]

Figure 1.4 Structural glass applications

The awareness of the capacity of LG to reduce the risk of damage and injury in various applications, such as automobile and aeroplane windshields, as well as bullet-resistant glass, has increased its usage over the years [18, 19]. Behr et al. [20] noted that laminated glass, while capable of fracturing, can resist complete breakage due to the presence of its interlayer, which holds the glass fragments together and provides security against theft and vandalism, making it an ideal material for high-security buildings, such as banks and museums, where enhanced protection is of high importance. In addition, because laminated glass can offer better sound insulation than monolithic float glass [21], it is a sought-after material for areas with high levels of noise, such as urban environments. Also, due to the ultraviolet (UV) absorption properties of the interlayer material, such as polyvinyl butyral (PVB) or ethylene-vinyl acetate (EVA), used in LG, it can be used to prevent fading and damage to artwork and interior furniture [22, 23]. Müller et al. [23] reported that laminated glass can filter up to 99% of damaging UV radiation. Therefore, the distinct advantages of laminated glass have attracted significant attention, positioning it as a material of choice for a wide range of applications in various architectural and construction design settings.

Despite LG many benefits, industries still find the use of LG as a structural load-bearing material challenging. This is primarily due to the difficulties in predicting its real-world behaviour, as laminated glass combines the brittleness and rigidity of glass with the flexibility and low stiffness of the interlayer [1, 24]. The structural behaviour of LG is affected by several factors, such as the material properties of its layers, as well as variations in its shape and size [25]. To use LG as a load-bearing material on a larger scale in the construction sector, it is important to have a deep understanding of its mechanical and structural behaviour. This knowledge will aid in the accurate determination of the structural design strength of LG.

1.1.2 Research Gaps

The increasing demand for secure and safe structural designs in the use of glass has sparked a keen interest to delve into the mechanical characterisation of glass, particularly laminated glass and float glass. Wang et al. [26] conducted a study examining the mechanical response of float glass under both three-point loading and impact loading. The study revealed the influence of loading rate on the deformation and failure modes of the float glass. Similarly, Osnes et al. [27] explored the behaviour of glass under various loading conditions and identified loading rate as a factor affecting flexural strength and crack propagation rate. Despite these commendable efforts, several gaps in understanding the mechanical characterisation of glass still exist. One notable gap is the behaviour of glass under biaxial stress states (glass being loaded in two directions). Glass may experience combined strains from multiple directions in real-world situations, such as structural components subjected to different complex loading conditions. Further study is required to understand how glass performs under biaxial stress and investigate the deformation and failure modes under this stress state. Another aspect that requires in-depth scientific understanding is the influence of loading span on the mechanical properties of glass. Given the high probability of locating multiple micro-flaws over a large span of a glass sheet, understanding the influence of loading span on its mechanical properties becomes necessary. Addressing these knowledge gaps holds great significance, as it can contribute to the enhanced usage of glass material.

1.2 Problem Statement

As the mechanical properties of glass are largely influenced by the presence of micro-flaws, and since the quantity of micro-flaws is expected to depend on the size of the glass material, it is essential to conduct a mechanical analysis of glass in relation to various loading spans under different types of load.

Various studies [10, 17, 28] have been reported on mechanical testings of glass using both three-point and four-point bending test methods. However, because of the fracture initiation that often occurs at the edges of the tested glass specimens during these tests, there is a belief that the edge flaws, which occur as a result of the cutting process, primarily influence the flexural strength of the glass tested with these methods. Thus in this study, both the four-point bend test (FPBT) and the ring-on-ring (ROR) test (a test where the applied loading region is distant from the edge) are used to evaluate the fracture strength of glass, specifically float glass (FG) and laminated glass (LG). FG and LG are considered in this study because they are the most utilised types of glass in various applications.

1.3 The Aim and Objectives of the Study

The study aims to investigate the effect of loading spans on the fracture strength of FG and LG when subjected to FPBT and ROR test. To achieve this, FPBT and ROR test experiments were conducted with three different loading spans. The main objectives of the study are as follows:

- Measure the flexural strength of FG and LG using three different loading spans in the FPBT.
- Evaluate the equibiaxial strength of FG and LG using three different loading rings in the ROR test.
- Compare the fracture strength obtained from the ROR test with that from the FPBT.
- Use the obtained fracture strength from the FPBT and the ROR test to calculate the critical flaw sizes using fracture mechanics.
- Analyse the fracture strength and fracture probability with the Weibull distribution.
- Use finite element analysis (FEA) to verify the stress obtained with an analytical method.

1.4 Significance of the Research

The mechanical characterisation of laminated and float glass is a vital area of study with profound implications for engineering applications, and public safety. This study has notable theoretical and practical contributions. The contributions are as follows:

- This study has the potential to provide an understanding of the proper application of FG and LG. Consequently, it reduces the sudden collapse of glass structures.
- This study contributes to the development of more sustainable and eco-friendly materials. Improved FG and LG applications can lead to longer lifespans for glass structures, reducing waste and the need for frequent replacements.
- This research addresses the inherent hazards and obstacles associated with FG and LG by bridging the knowledge gaps in understanding how loading spans influence their fracture strength.
- In the analysis of glass failure, the Weibull distribution is an important statistical tool. It provides a robust method for predicting the probability of failure in glass and how these probabilities scale with specimen volume. By applying Weibull distribution analysis, the experimental data can be interpreted more effectively, failure probabilities can be predicted, and glass designs can be tailored to meet specific safety and performance criteria.

- The finite element analysis in the study provides virtual prototypes for the FPBT and ROR test, which enable rapid modifications in the experimental setup.

1.5 Limitations of the Study

With the significance of this research, it is important to acknowledge and address its potential limitations. First, the emphasis of this study was only on FG and LG; hence, generalisations of the results to all glass products are limited. Also, the experimental testing parameters, such as environmental conditions and loading rate, employed in this study might not adequately represent the various usage circumstances for glass. These limitations may affect the general applicability of the results to real-world applications for all glass products. This suggests the need for further research to expand the scope and depth of the study on the structural behaviour of glass.

1.6 Outline of the Thesis

The introduction chapter summarises the thesis, beginning with a brief background study, a description of the problem, and the aim and objectives. It also includes the significance and limitations of the study. The literature review chapter summarises various concepts related to the study, such as glass material and its production, different classes of glass, interlayer materials and their properties, the mechanical behaviour of glass, LG behaviour under load, post-breakage behaviour, mechanical testing methods, fracture toughness of glass, and the study of Weibull distribution. The experimental methods chapter provides a detailed explanation of the experimental procedure used, incorporating specimens preparation, glass surface identification, experimental design, test procedure, simulation approach, and Weibull parameters evaluation process. The results from the tests are presented in the results chapter. The discussion chapter covers the analysis of the objectives of the research. The conclusion chapter of this thesis presents an overview of the research outcomes. Also, the recommendation chapter includes directions for future investigations.

Chapter 2

Literature Review

This chapter provides a review of the literature on glass, covering its history as a material, production processes, and various types of glass. It explores the mechanical behaviour of glass, laminated glass (LG), and interlayer materials, detailing their properties. Additionally, the chapter discusses the behaviour of LG under mechanical loads, the post-breakage behaviour of glass, mechanical testing methods, fracture toughness, and the Weibull distribution.

2.1 The Glass Material

Generally, glass is a hard and brittle material. It is non-crystalline or amorphous, which means its atomic structure is not organised in a regular repeating pattern. This distinguishes glass from crystalline solids [5, 29, 30]. Unlike many other substances, glass does not have a well-defined melting point [5, 31]. Instead, it undergoes a glass transition, shifting from a liquid to a solid state across a range of temperatures. For certain glasses, this range is between 140°C and 370°C, though the exact transition temperature is determined by the exact structure and composition of the glass [32]. The strong chemical resistance feature of glass makes it a valuable material, as it can withstand harsh conditions and resist degradation [33]. Depending on their usage, many varieties of glass exhibit different chemical and physical characteristics. Typically, glass consists of sand (which contains silica), soda ash, and limestone as its main constituents [34]. A small number of other additives may also be present [35].

2.1.1 History of Glass

For many years, glass has played a significant role in human history. The dark volcanic glass known as obsidian was particularly crucial in ancient times [36, 37]. This naturally occurring glass forms when silica-rich volcanic lava cools rapidly [37]. Its ability to produce razor-sharp edges made it highly valuable for making blades and arrowheads [38]. Glass production is thought to have been discovered around 3000 BC, possibly as a by-product of metallurgy or as a natural improvement from a ceramic material called faience [36, 39]. Initially, glass was produced from a relatively undeveloped state, as production methods and chemical compositions advanced, glass products gradually improved, broadening their

potential applications [37]. The changes in glass composition are explained in the following sections to show the function of each element that makes up glass.

2.1.1.1 Soda-lime Glass

The glass produced from the combination of soda (Na_2O), lime (CaO), and silica (SiO_2) is often referred to as soda-lime glass, regardless of the proportion of each constituent [40, 41]. The chemical composition of glass varies widely, giving rise to a multitude of chemical and physical characteristics that have a direct impact on its potential applications. Moreover, apart from the raw materials utilised, the characteristics of glass are also influenced by the heating procedure, precise temperature regulation, and the specific method and speed of cooling, which is commonly referred to as annealing [37, 42].

Soda-lime glass, which is the main material in the glass production industry and widely used in construction applications like windows, has seen changes in its composition over time [40]. To improve its chemical resistance, thermal stability and mechanical properties, the modern composition of soda-lime glass incorporates magnesia (magnesium oxide, MgO) and alumina (aluminium oxide, Al_2O_3) [37]. According to the European standard EN 572 [43], soda-lime silicate glass has the following standardised composition: 69-74% silica, 10-16% soda, 5-14% lime, 0-6% magnesia, 0-3% alumina, and 0-5% miscellaneous components. The EN 572-1 standard, titled "Glass in building - Basic soda-lime silicate glass products," provides comprehensive information on the chemical composition, important mechanical and physical properties, and general quality control criteria for this type of glass.

2.1.1.2 Aluminosilicate Glass

Aluminosilicate glass differs from soda-lime glass by having a significantly higher alumina content, typically ranging from 10% to 25% of its composition, with over 10% lime [37, 44]. This glass type is characterised by elevated transition temperatures and enhanced mechanical properties like scratch resistance and hardness. The higher presence of alumina and lime in the glass composition is crucial for facilitating efficient ion exchange [36, 45]. Section 2.3.4 provides a more detailed discussion of the process of ion exchange, which greatly improves the surface compressive strength of the glass. Apart from silica and other two substances (alumina and lime) mentioned earlier, aluminosilicate glass often contains boric oxide (B_2O_3), barium oxide (Bao), and magnesia [46]. Aluminosilicate glasses can be categorised into two groups based on their additional components. One of these groups is the alkaline earth aluminosilicate glass. It is purposefully designed for high-temperature applications like halogen lamps [37, 44]. It incorporates alkaline earth metals, which ensure its suitability for such applications. Another group of aluminosilicate glass is the alkali aluminosilicate glass, which serves various purposes such as display screens in electronics and telecommunications, optical glass in medical devices, and windshields and windows in vehicles [44].

2.2 Production Method of Glass

Glass production involves a sequence of five main steps: batching, melting, fining, shaping, and post-processing [47]. Although the first three steps are common to most glass manufacturing processes, the two final stages vary depending on the type of glass being made [48].

Float glass (FG), also known as annealed glass (ANG), is primarily composed of soda-lime glass and is the most commonly used type of glass, produced through the float process. The float process, illustrated in Figure 2.1, accounts for 90% of the production of glass in flat form [5, 49]. In the process, molten glass is floated on a bath of liquid tin. The thickness of the resulting glass is determined by adjusting the speed at which the glass is extracted from the tin bath [50]. After this, the glass is gradually cooled in a long tunnel oven, known as the annealing lehr [4, 50, 51]. While annealing in metals involves a heat treatment to modify the microstructure, in glass it specifically refers to a controlled slow cooling from above the glass transition temperature to below it. This controlled cooling prevents residual stresses from developing in the glass sheet, which would otherwise make it prone to fracture. Before shipping the glass to the consumer, the glass must first undergo inspection and cutting. Through this float process, the glass is given a flat surface on both sides, resulting in large, uniform sheets of glass suitable for various usage.

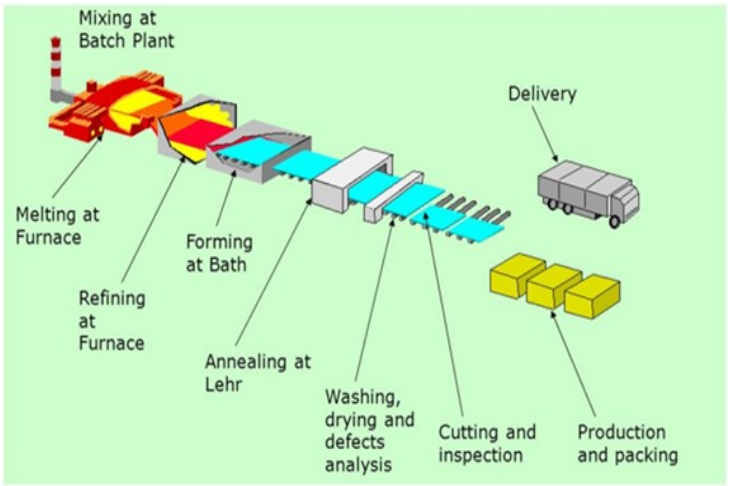

Figure 2.1 Method of producing float glass [52]

FG can undergo further processes to produce various types of glass, such as heat-treated glass and LG. Figure 2.2 depicts the glass composition as well as other glass modifications that can be made.

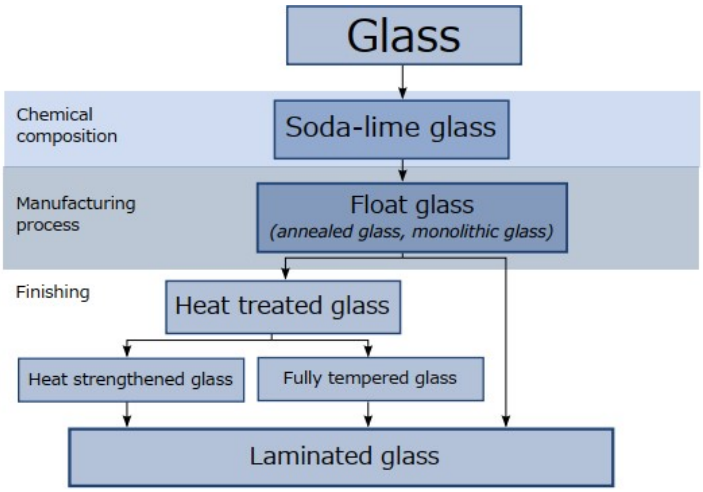

Figure 2.2 Flow chart of glass types and its modifications [5]

2.2.1 Air-side vs Tin-side of the Glass

The properties of the glass are not the same on both sides, although the glass may look identical to the naked eye [3]. As mentioned in Section 2.2, glass can be produced through the float process, in which the glass surface that comes into direct contact with the tin bath and transport rollers is usually called the "tin-side." This side has a thin layer of tin oxide deposited on it during the production process [10, 53, 54]. The other surface of the glass is called the air-side. Each surface is exposed to different temperature conditions during the production process, resulting in varying properties and different distributions of micro-flaws on each surface [3, 11]. On the tin-side, the process of ion exchange with silicon allows tin to disperse into the glass [55, 56]. This can result in tin penetration ranging from 10 μm to 50 μm, often leading to the formation of large micro-flaws on the tin-side surface [56]. Conversely, on the air-side, micro-flaws are typically smaller than those on the tin-side by a factor of around 1.5 to 2.0 [4, 57]. The air-side tends to have greater flexural strength, potentially up to twice that of the tin-side [57, 58].

The air-side and tin-side of the glass react differently to cleaning chemicals. Cleaning products containing acid or alkali can damage the tin-side of the glass, as these substances readily dissolve the tin oxide layer [59, 60]. While the air-side does not have a tin oxide layer to be affected, it is generally more resistant to cleaning agents [59, 60]. Also, the two sides of the glass differ significantly in their light reflection properties, with the tin-side reflecting more light than the air-side [59, 60]. To prevent unwanted reflections, many manufacturers print their logos or other information on the air-side of the glass.

Understanding these differences is important for making informed decisions about how to handle and use glass products. Tests that can be used to identify the air-side and tin-side are outlined below for better understanding.

2.2.1.1 Ultraviolet Light Test

By shining ultraviolet (UV) light, such as a UV lamp, on glass, it is possible to identify the tin-side. Due to the different light reflection properties of the two sides of glass, the tin-side will glow brightly and turn a milky white when exposed to UV light. However, the air-side has minimal or no reflectance [54]. Figure 2.3 displays this approach.

Figure 2.3 Image of ultraviolet test [54]

2.2.1.2 Water Drops Test

The water test is another method used to differentiate the tin-side from the air-side because the tin-side and air-side of glass have different surface tensions. To conduct this test, a water droplet is applied to the glass surface from approximately 2-3 cm height. If the water spreads out, it indicates the air-side, which has higher surface energy, leading to stronger adhesive forces between the surface and the water compared to the cohesive forces within the water. Otherwise, if the droplet remains more intact, it indicates the tin-side, which has lower surface energy [53]. Figure 2.4 displays this explanation.

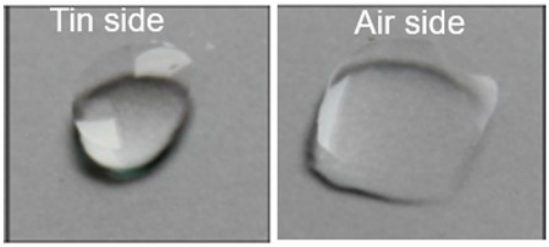

Figure 2.4 Image of water drops test [53]

2.3 Types of Glass

Commercial glass can be categorised into various classifications based on its chemical composition, such as soda-lime glass, silica glass, borosilicate glass, lead-alkali silicate glass and other variants [60, 61]. However, the processing and post-processing stages allow for

the production of different types of glass with distinct properties, which enhance their versatility as materials in the building sector. The following are a few examples of glass based on processing and post-processing techniques:

- Float glass or annealed glass
- Fully tempered glass (Toughened glass)
- Heat-strengthened glass.
- Chemical tempered glass
- Laminated glass

2.3.1 Float or Annealed Glass (ANG)

FG is manufactured through the float process described in section 2.2. During the manufacturing, FG is gradually cooled from high temperatures, which results in low or insignificant residual stress within the glass material [50, 61]. FG remains relatively fragile and can break when subjected to stresses beyond its design limits or if improperly installed. When it does break, it shatters into sharp, pointed fragments [1, 61]. The lack of residual stress in FG contributes to the dangerous shards that can cause piercing or cutting injuries. The low or complete absence of residual strength in FG has a significant impact on its post-fracture behaviour. Float glass lacks the capacity to bear heavy weight, which could lead to the following: [61]:

- Complete or partial collapse of the FG structure.
- Penetration through the FG structure.
- Falling glass fragments are particularly risky when FG is used at height.

The lack of capacity to bear heavy weight prevents monolithic FG from being utilised as a structural material under high stress [62–64]. According to EN 572-1 [43], FG has a typical bending strength of 45 MPa. However, FG can be processed into various types of glass that are stronger with improved breakage properties or enhanced safety post-fracture properties. These processed glass types are usually laminated glass, toughened glass, and heat-strengthened glass. The manufactured FG must meet certain quality standards as outlined in EN 572-1, ASTM C 1036, and EN 572-2 [43, 65, 66].

2.3.2 Heat-Strengthened Glass (HSG)

HSG can be obtained from FG through a regulated heating and cooling process, which makes it more resistant to mechanical and thermal stresses compared to regular FG [2]. The fundamental concept used during heat treatment is to establish a state of compression at the surface and edges of the glass. This state is acquired by initially heating the glass, followed by rapid surface cooling, leaving the core relatively hot [2, 61]. As the core cools

down, it applies pressure to the edges and surfaces, resulting in compression. Therefore, before any chance of breakage can take place, applied loads such as thermal stresses, missile impact, or wind pressure must first overcome this compression [60]. This process creates permanent internal tensile stress and permanent compressive surface stress in the HSG, resulting in improved bending strength and a reduced risk of glass fracture [2]. The flexural strength of HSG is a mixture of FG strength and the surface compressive stress introduced during heat treatment. The residual compressive surface stress of HSG typically ranges from 24 MPa to 70 MPa [61, 67]. This variability is influenced by surface conditions, load duration, environmental factors, and the extent of heat treatment [67]. Quality standards for HSG are outlined in ASTM C1048 and EN 1863-1 [68, 69]. ASTM C1048 defines HSG based on the degree of residual stress that occurs on the edges or surface of the glass during the manufacturing process, while EN 1863-1 defines it based on fracture properties and should exhibit a characteristic strength of at least 75 MPa at a 95% confidence level. Heat-strengthened procedures are employed in the production of high-strength glass, which results in a favourable residual stress distribution across the thickness of the HSG [2, 5, 61]. This distribution is marked by tensile stress in the inner and compressive stress at the surfaces as illustrated in the tempered glass part of Figure 2.5.

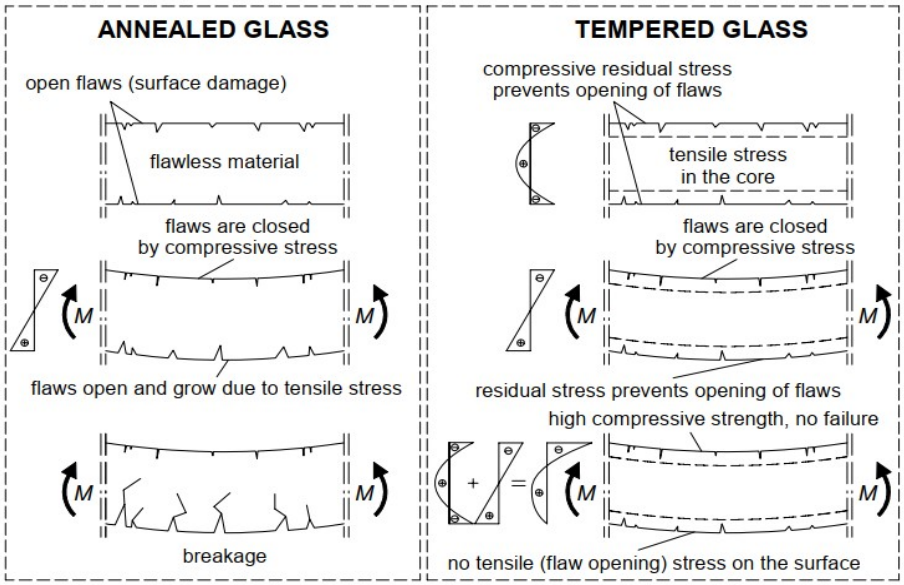

Figure 2.5 Fundamental concept behind heat treated glass [2]

The left side of the Figure 2.5 shows annealed glass, which is produced via the float glass process (see section 2.3.1). In this state, surface flaws are more exposed to tensile stresses and can propagate readily, making the glass vulnerable to fracture. In contrast, the right side of the figure depicts tempered (or heat-strengthened) glass, where a compressive stress is developed on the surface through rapid cooling. This compressive layer counteracts surface flaws, effectively "closing" any cracks that might form and thereby significantly enhancing the overall strength of the glass.

2.3.3 Fully Tempered Glass (Toughened Glass)

Toughened glass and heat-strengthened glass both undergo similar processing, with differences in their cooling rates. Toughened glass is cooled more rapidly, which results in higher compressive surface stress and higher bending strength than heat-strengthened glass [2]. Due to exposure to elevated stress levels during manufacturing, toughened glass is more resistant to both mechanical and thermal stresses, which makes it less prone to breakage [63, 70]. Like heat-strengthened glass discussed in Section 2.3.2, a bending fracture cannot occur in a toughened glass until the residual compressive surface stresses are neutralised. Toughened glass typically has residual compressive surface stress of more than 70 MPa [63]. However, as can be seen in Figure 2.6c, when toughened glass breaks, it usually shatters into tiny, rounded pieces of glass called dice. These tiny fragments could have an aspect ratio of one [63, 71]. Although these fragments lack sharp and dangerous edges, they can accumulate into clumps with blunt edges and pose a risk of injury [63, 71]. Therefore, precautions are necessary to mitigate the risk of injury from glass fragments in the event of a fracture. Quality specifications for fully tempered glass are outlined in ASTM C 1048 and EN 12150-1 [69, 72]. ASTM C 1048 defines toughened glass based on the residual stress levels induced during production, while EN 12150-1 [72] specifies that toughened glass should fracture into small pieces and must possess a minimum strength of 120 MPa, with a 95% confidence level. Figure 2.6 displays the comparison of fracture patterns observed in float, heat-strengthened, and toughened glasses.

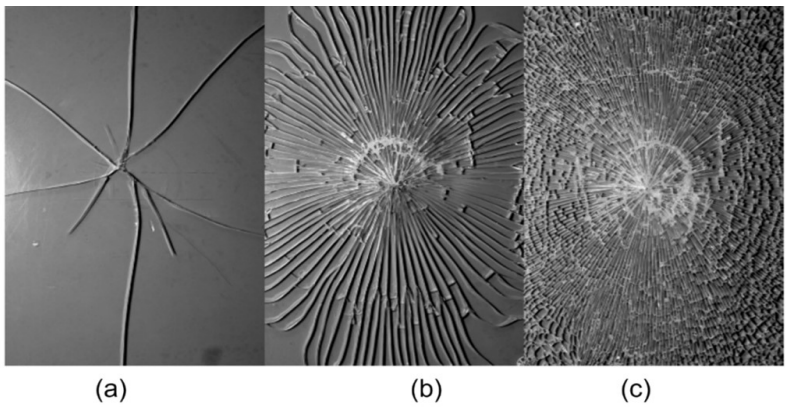

Figure 2.6 Comparison of fracture patterns: (a) float glass (b) heat-strengthened glass (c)toughened glass [2]

2.3.4 Chemical Tempered Glass

Glass can be chemically tempered through a process called ion exchange, during which smaller ions on the surface of the glass are exchanged for larger ones, resulting in the creation of residual compressive stress [2]. In this process, the glass is submerged in a solution rich in potassium ions (K+) and heated to temperatures below its transformation point, which is approximately 400°C [1, 2]. This leads to the replacement of sodium

ions on the glass surface with potassium ions. Such treatment can increase the residual compressive stress level up to 800 MPa or even 1,000 MPa, which leads to a significant enhancement in the strength of the glass [1]. While chemically tempered glass offers substantial strength enhancements, its utilisation in construction is presently restricted due to its high cost of production and size limitations [62]. However, as technology and methodologies advance, these limitations are expected to decrease, potentially leading to broader and more affordable use of chemically tempered glass in the construction industry. Aluminosilicate glass is often chosen for chemical tempering due to its high alumina content, which facilitates the improved and accelerated diffusion of alkali ions [73].

2.3.5 Overview of Tempered Glass

Figure 2.7 illustrates the stress profile of tempered glass, while Table 2.1 summarises the differences among various types of processed glass.

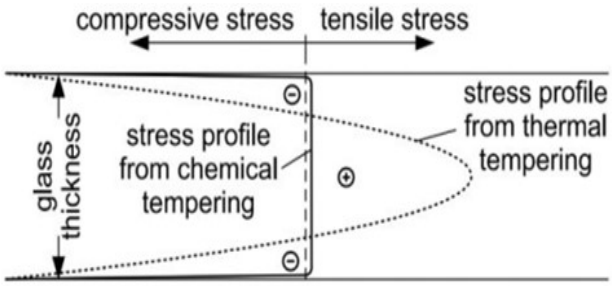

Figure 2.7 Stress profile of tempered glass [10]

Table 2.1 *Types of glass and their characteristics*

Types of Glass	Bending Strength	Minimum Required Characteristic Strength	Residual Compressive Surface Stress	Fracture Behaviour
Annealed Glass	Low	45 MPa [43]	-	Sharp-edged, pointed fragments [1]
Heat Strengthened Glass	Higher than Float Glass	75 MPa [68]	24 – 70 MPa [21,61]	Similar to annealed glass [63]
Toughened Glass	Higher than Heat Strengthened Glass	120 MPa [72]	Over 80 MPa [63]	Break into tiny relatively blunt glass fragments called dice [63]
Chemical Tempered Glass	Similar to Toughened Glass	Above 150 MPa [2]	Up to 800 MPa [1, 31]	Similar to toughened glass [2]

2.4 Mechanical Behaviour of Glass

Glass generally exhibits elastic behaviour up until the point at which it is stretched above its flexural strength limit. At this point, it will fracture in a brittle manner [51, 60]. Thus, it is crucial to identify the magnitude of all stress peaks within the glass, as any stress peak that surpasses the strength of the glass can trigger fracture. At standard room temperature, glass is a brittle and isotropic material that lacks inherent ductility [1, 2]. The graph that illustrates how ductile materials like steel and brittle materials such as glass react to stress and strain is seen in Figure 2.8. Glass exhibits no plastic behaviour in comparison to steel. Therefore, if the glass is utilised as a structural element, catastrophic collapse can occur when glass fracture happens [2, 70]. The durability of glass diminishes over time when it is under a load, resulting in a decline in its strength [1, 74]. Micro-flaws or defects are crucial in determining its mechanical strength. Due to these micro-flaws, the design value for the mechanical strength of glass is always lower than the actual or practical maximum mechanical strength [3]. The stiffness and strength of glass are covered individually in the next paragraphs because they are more complicated and critical for structural applications.

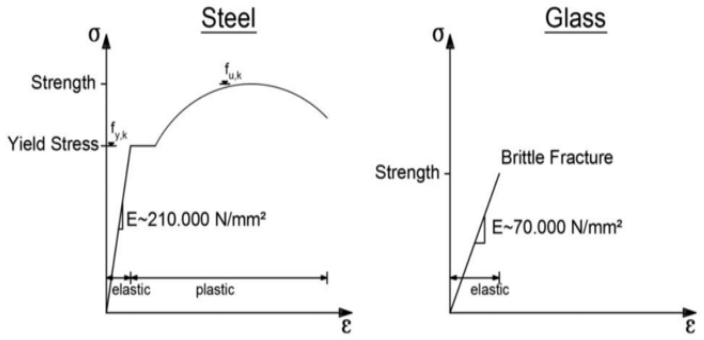

Figure 2.8 Graphs of stress-strain behaviour of steel vs annealed glass [51]

2.4.1 Stiffness

Glass stiffness refers to its ability to resist deformation when subjected to an external load [1, 2]. This property is typically quantified using Young's modulus, which measures the ratio of applied stress to the resulting strain in the elastic region [17]. The Young's modulus values for glass range from 50,000 to 90,000 MPa [2]. Several factors can influence glass stiffness, including composition, temperature, and the presence of impurities or micro-flaws [25, 75]. To ensure uniform and predictable stiffness in glass components, close monitoring of their chemical composition, manufacturing process, and handling is essential. Understanding and controlling the factors that influence glass stiffness is important to ensure the reliable function of glass components and prevent sudden fracture under stress [1].

2.4.2 Strength

The strength of glass cannot be precisely measured by considering the properties of its constituent materials alone [75, 76]. Factors such as size, shape, processing methods, and environmental conditions also significantly influence its strength [62, 64]. Consequently, the strength of a glass component is often ambiguous and difficult to quantify as it depends on specific circumstances rather than being totally depend on the inherent property of the component it is made of [1, 2]. The discrepancy between their theoretical strength (which is based on molecular bonding) and their actual strength is largely influenced by surface and edge micro-flaws [70, 75].

In a bending test of a glass specimen, the top surface undergoes compression, while the bottom surface is subjected to tension, as illustrated in Figure 2.9. During the bending test, the bottom surface fractured first because of the limited ability of the glass to withstand significant tensile stresses. The compressive strength of the glass is much higher than its tensile strength [1].

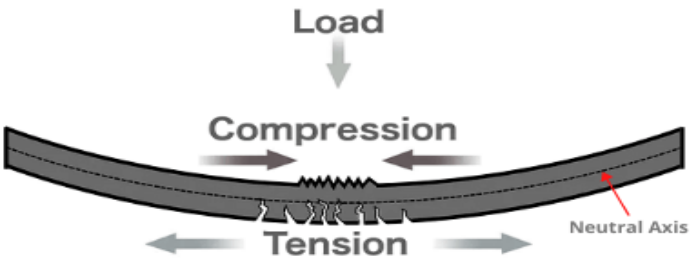

Figure 2.9 Diagram showing compression on top, tension below during a bending test [77]

2.5 Laminated Glass (LG)

LG is a composite material that is composed of multiple layers of glass fused with polymer interlayers [10, 28]. It is commonly utilised in architectural applications, like the crafting of glass beams, stair treads, landings, and columns [28, 78, 79]. Beyond architectural applications, LG is also found in automotive windshields and aircraft windows, which highlights its widespread usage [28,79]. Typically, LG incorporates two or more glass panels, bonded to one or more plastic interlayers [28, 61]. Figure 2.10 displays the configuration of laminated glass.

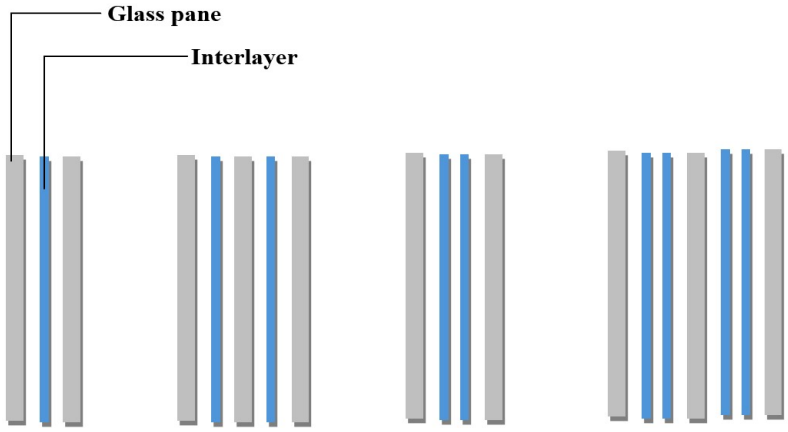

Figure 2.10 Potential configurations for laminated glass [10]

Figure 2.11 illustrates the composition of laminated glass components. LG can be made using different types of glass, like annealed glass, tempered glass, or a combination of both, with different interlayers like polyvinyl butyral (PVB), ethylene vinyl acetate (EVA) and sentryGlas plus (SGP) in between [21, 51]. The glass panes and interlayers can have different thicknesses.

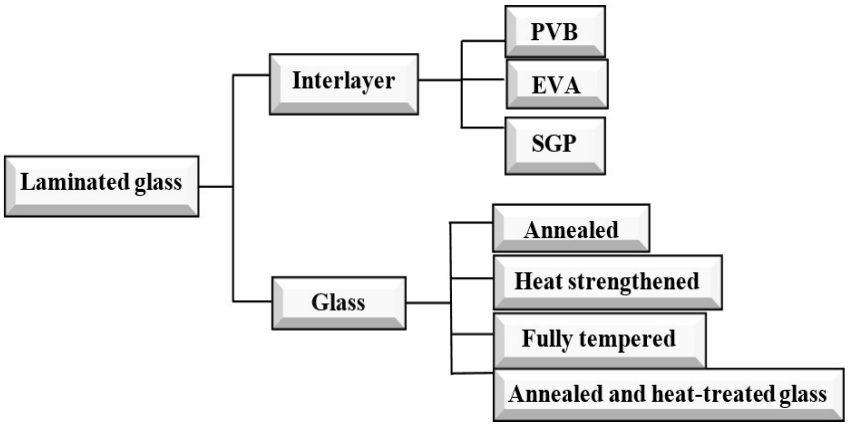

Figure 2.11 Flow-chat of laminated glass composition components

A defining feature of laminated glass is its safety: even when broken, the interlayer retains the glass fragments, mitigating the risk of injury and enhancing its post-breakage behaviour [1, 2]. Its combination of safety and security features, along with its improved post-breakage behaviour, makes it the preferred choice for various structural applications [51, 60]. Also, in contrast to annealed glass, which behaves elastically until it fractures, LG typically exhibits viscoelastic behaviour due to its interlayer [60]. This means that LG will experience creep under static loading and will relax when continuous deformation is removed [61]. The mechanical properties of LG are greatly influenced by its viscoelastic nature, which is influenced by various factors, such as temperature, loading rate, and loading duration [7, 80].

2.5.1 The Production Method of Laminated Glass

LG can be manufactured through two methods: the autoclave method [51], and the Ultraviolet (UV) curing method [60]. In some instances, a combination of both methods may be utilised [60]. The layout of the production methods are illustrated in Figure 2.12

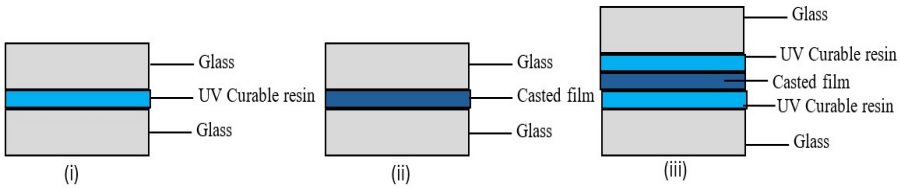

Figure 2.12 Pictures of LG production layout by different methods: (i) UV curing method, (ii) autoclave method; (iii) combination of UV and autoclave methods [60]

2.5.1.1 Autoclave Method

The autoclave technique has been in use since the 1930s [14]. The process typically involves inserting a polymer film between two pieces of glass and then removing the air in a clean environment using specialised nip rollers or a vacuum [51]. The final bonding

takes place within autoclaves, hydraulic presses, or any similar devices, which subject the combination to high temperature and pressure, resulting in the fusion of the film to the glass [14]. This bonding process typically occurs at temperatures ranging between 110°C and 140°C, with pressures around 0.8 MPa, and lasts approximately 70 minutes in the autoclave [14, 60].

This technique requires significant capital investment and labour. The size of the autoclave needed depends on the dimensions of the laminated glass to be produced, which contributes to the overall cost of the product [31]. LG produced through this method may exhibit residual stresses resulting from the heat-bonding process [60]. This process is illustrated in Figure 2.13.

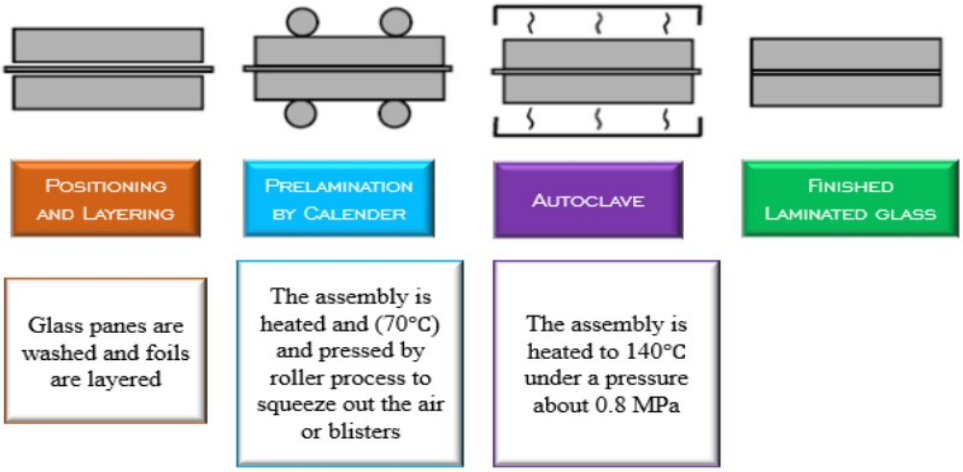

Figure 2.13 Lamination procedure through autoclave method [14]

2.5.1.2 Ultraviolet Curing Method

LG can be produced by using a liquid-based interlayer system, which is cured with UV radiation at room temperature [60, 81]. The production process involves thoroughly cleaning the glass panes, creating a space between them using double-sided tape, and then filling the space with the resin (which serves as the interlayer) through an automated metering pump system. Finally, the resin is cured by exposing it to UV radiation [60].

Compared to autoclaved methods, UV-based laminating methods are not only cost-effective but also offer numerous advantages. These include a rapid filling and curing process, enabling the production of high-quality LG in a shorter timeframe [60]. The use of UV-curable interlayers does not require mixing, which makes the resulting LG product more consistent. Additionally, these interlayers have an unlimited storage life until they are exposed to UV light [60, 81].

2.6 Interlayer Materials

There are numerous interlayers available on the market that are suitable for various LG applications. Interlayers have the potential to enhance the visual appeal of a structure with a distinct aesthetic look through the use of coloured or patterned variations [4, 82]. Some interlayers are specifically designed to improve thermal performance and security properties [4]. Regulating the adhesive bond between the glass pane and the interlayer is necessary to help achieve optimum performance in LG [60]. Sometimes, additives like silanes are used to achieve the required bonding [58]. Schimmelpenningh et al. [83] developed a LG structure that can withstand severe wind and impact. It was discovered that striking a balance between the softness of the interlayer and its adhesion to the glass is important. If the interlayer is too soft or does not adhere well to the glass, the LG will not be strong enough to withstand high wind loads after impact. However, if the interlayer is too stiff and adheres too tightly to the glass, such LG will not have a high level of impact resistance [83]. Various types of polymeric materials can be employed as interlayers during the production of LG [51]. The following sections discuss a few examples of the most common interlayer used for LG.

2.6.1 Polyvinyl Butyral (PVB)

PVB is a material that has remarkable properties such as strong adhesion, optical clarity, resistance to sunlight, tear resistance, and impact absorption [4, 84]. Its primary purpose in LG is to mitigate the damage or injury that can occur during a forceful impact, preventing objects or persons within an enclosed area from being harmed [84]. During the boom of the automotive industry, it was important to enhance the safety of automobile windshields by improving their post-fracture behaviour. The goal was to create windshields capable of absorbing impact during collisions, thereby reducing the risk of severe passenger injuries and preventing ejection through broken glass [34, 85]. Although PVB is primarily made from a rigid copolymer resin, the addition of plasticisers has allowed it to meet the critical safety criteria [21]. Its high tear strength and resilience serve as a safety net, which absorbs sufficient energy to prevent penetration from projectiles or a vehicle occupant's head [60].

The extensive use of PVB for LG in the automotive sector has led to its subsequent incorporation into the construction industry. PVB has been a dominant material in LG production for over 90 years, with only slight modifications made to it to meet specific application needs [21, 79]. Polyvinyl butyral (PVB) evenly adheres to both the tin and air surfaces [60].

2.6.2 Ethylene Vinyl Acetate (EVA)

In addition to various PVB variations, modern polymer materials like EVA have also been utilised to create LG. EVA presents several advantages over PVB, including high flexibility, better clarity, optical properties, durability and a simplified lamination process [21, 86].

EVA laminated glass is versatile, finding applications in building façades, skylights, and automotive windshields. The high flexibility of EVA makes it especially suitable for curved or bent LG applications [87]. In comparison to PVB laminated glass, laminated glass with EVA provides superior sound insulation, making it ideal for buildings situated in noisy areas [21]. Additionally, the clarity of EVA laminated glass surpassed that of PVB laminated glass, resulting in improved visibility and reduced distortion [21]. This feature is highly important for automotive windshields, where clarity is crucial for safe driving. Given these significant advantages, EVA stands out as an excellent laminating interlayer material for various applications across different industries. It is a valuable alternative to PVB.

2.6.3 SentryGlas Plus (SGP)

The SentryGlas Plus (SGP) interlayer is a high-performance material known for its superior strength, durability, and excellent post-breakage performance. This makes SGP a prime choice for applications requiring high security, structural glazing, bomb blast resistance, ballistics protection, and use in marine vessels [70, 84]. Over time, SGP has changed in composition and is currently being promoted as a structural interlayer material that possesses enhanced edge stability, as well as provides resistance against bomb blasts [84].

SGP falls under the ionoplast category [34]. An ionoplast is a durable sheet crafted from copolymers of ethylene and methacrylic acid, supplemented with small quantities of metal salts [34]. This robust sheet not only forms a permanent bond with glass but also boasts Young's modulus of over 100 MPa [84]. This enables it to maintain integrity even at temperatures up to 50°C [78, 84].

When laminating the float glass with SentryGlas Plus, the preference is to bond the tin-side of the glass with the SGP, as the tin-side has a stronger bond with SGP than the air-side due to the different distribution of micro-flaws [88]. However, if this is not possible, an adhesion promoter such as silanes will be used to ensure that appropriate bonding occurs between the interlayer and the glass [58].

2.7 Properties of Interlayer Materials

The interlayer materials discussed in Section 2.6 exhibit mechanical behaviour that is dependent on temperature and time [86, 89]. These materials can demonstrate elastic, viscoelastic or viscous behaviour at different temperatures. Most interlayer materials used for construction applications exhibit viscoelastic behaviour when subjected to temperatures ranging between -20°C and + 80°C [89]. Viscoelastic materials are sensitive to load, temperature and time, which can influence their properties in various ways. For instance, when subjected to heavy loads and prolonged loading times, the interlayer creeps and becomes weaker as the temperature increases [4,90]. Therefore, it is essential to measure the mechanical properties of the interlayers at various temperatures and times. The mechanical properties of the interlayer influence the performance and durability of laminated glass under different temperature conditions [4]. An examination of the mechanical properties of the materials will facilitate the selection of an appropriate interlayer, which will ensure the optimal performance and durability of LG products. Table 2.2 shows the properties of some interlayer materials at a set temperature.

Table 2.2 *Comparison of interlayer properties: PVB vs. EVA vs. SGP [86]*

Property	**PVB**	**EVA**	**SGP**
Density (kg/m^3)	1070	930	950
Tensile strength (N/mm^2)	> 20	$10 - 25$	34.5
Maximum elongation (%)	> 250	> 500	400
Coefficient of thermal expansion (10^{-6} K^{-1})	468	90	100-150
Glass transition temperature (°C)	20	-20	55

2.8 Laminated Glass Behaviour under Load

LG has distinct behaviour under load compared to monolithic float glass due to the presence of a plastic interlayer within its structure [14]. This interlayer acts as a shock absorber, dispersing the load across a larger surface area and preventing hazardous glass shattering [91].

The load-bearing performance of LG is influenced by the thickness of both the glass panes and the interlayers [84, 92]. Using thicker components enhances the strength and durability of LG but also results in increased weight and manufacturing costs [4]. Moreover, the type of load applied—whether static, like the weight of a building, or dynamic, like the impact from bullets or explosions—also determines how LG responds [84].

The inherent flexibility of the interlayer material equips the LG with the capacity to bend and deform to some extent without breaking [91]. This attribute renders it exceptionally suitable for scenarios where the LG may encounter wind forces or other significant external loads.

According to Xiufeng et al., the presence of the interlayer in the LG adds complexity to its stress behaviour [9]. The interlayer is capable of absorbing energy, which affects the distribution of stress across the LG which can be seen in Figure 2.14. Two models have been frequently used in earlier research to explain the structural behaviour of LG [9, 93]. The first model, known as the effective thickness model or equivalent monolithic glass plate model, operates on the assumption that the two layers of glass are seamlessly fused, with the shear modulus approaching infinity, thereby establishing a perfect bond. There is full shear transfer because shear stress is fully transferred between the upper and lower layers, as depicted in Figure 2.14a. This conceptualisation simplifies the LG into a single monolithic layer possessing an effective thickness (Figure 2.15a). The flexural inertia in this model is determined based on the combined thickness of the LG components [94, 95].

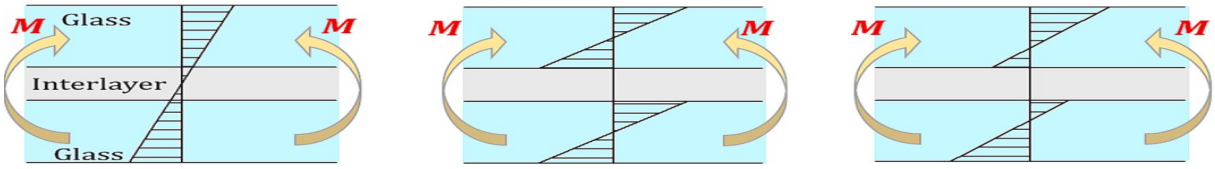

a. Full shear stress **b.** No shear stress **c.** Partial shear stress

Figure 2.14 Bending stress distribution for laminated glass subjected to bending [9]

a. Monolithic boundary **b.** Layered boundary **c.** Intermediate configuration

Figure 2.15 Laminated glass behaviour boundary [93]

In the second model called the layered glass unit model, it is considered that the LG has plies that can freely slide, with the shear modulus of the interlayer tending to zero. No shear transfer occurs because shear stress cannot be transferred between the layers, leading to the bending stress distribution illustrated in Figure 2.14b. In this model, the flexural inertia is determined by combining the inertia of each ply, while considering both the properties of the individual glass sheets and the interlayer (Figure 2.15b). These two models establish the highest and lowest stiffness boundaries for LG: the equivalent monolithic glass plate model determines the highest boundary, while the layered glass

unit model sets the lowest boundary. In general, the real behaviour of LG units falls somewhere between these two cases (Figure 2.15c), and can be determined using the finite element method or by using the effective thickness method [95]. Partial shear transfer can occur, where only a portion of the interlayer shear stress is transferred; the corresponding situation is depicted in Figure 2.14c. Behr et al [96] demonstrated that as the temperature increased the LG went from a monolithic plate to a layered glass unit with a decrease in interlayer stiffness.

2.9 Glass Post-Breakage Behaviour

The post-breakage behaviour of LG is observed when at least one glass sheet is fractured, but the glass pieces remain attached to the interlayer, preventing the shards from becoming a projectile and causing injury. This makes LG a safer option compared to other glazing materials [92, 97]. That is why LG has been the preferred material for automobile windshields for many years. When glass is laminated with a polymer interlayer, it exhibits improved post-failure behaviour due to the presence of the interlayer.r [21]. This enhances its ability to absorb energy during an impact, thereby reducing the risk of injury. On the other hand, float glass (FG), which is glass that does not contain any plastic interlayer, has a brittle post-fracture behaviour that can be hazardous in case of accidents [17, 60]. Figure 2.16 illustrates the differences in the post-breakage behaviour of FG and LG.

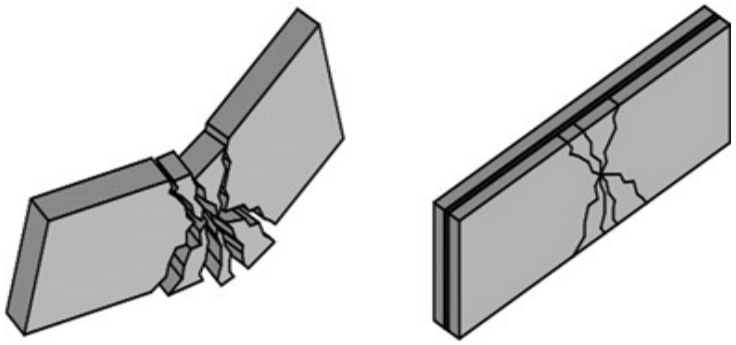

Figure 2.16 Behaviour of different types of glass after impact: float glass (on the left) and laminated glass (on the right) [17]

Figure 2.17 shows the stress distribution on LG to illustrate its breakage behaviour, which occurs in three stages. During the initial phase (Stage 1) in LG, both glass sheets experience tension at the bottom and compression at the top. The bottom glass sheet is more vulnerable to crack propagation because, unlike the top sheet, its tension side is not supported by interlayer bonding. As a result, the bottom sheet fractures first when its flexural strength is exceeded. In Stage 2, where only one glass layer is intact (the top layer), this layer bears all the bending loads. The bending moment capacity decreases due to the reduced second moment of area [10, 98]. This leads to a sharp change between Stage 1 and 2 in the moment-curvature relationship because the bending moment that

leads to a fracture in Stage 1 is not maintainable in Stage 2 when subjected to static loading [10, 98]. In Stage 3, after the fracturing of both glass layers, the tension resistance is lost, but the interlayer remains elastic. The bending resistance at this stage comes from the combined action of the interlayer in tension and the compressive stresses from the bonded glass fragments [10, 98]. Nevertheless, the remaining bending ability is minimal, as laminated glass can collapse when both glass layers fracture. This was confirmed by the analytical study of Galuppi and Royer-Carfagni [99], who observed a drastic decrease in bending stiffness after fracture. Fragment detachment of the LG can occur after the failure of the two glass layers, especially when LG is used for ceilings or roofs. The likelihood of detachment is high when LG is made of toughened glass, as it breaks into tiny fragments that can easily detach from the interlayer. Therefore, using toughened glass as the only glass pane in LG is not recommended. Instead, toughened glass can be combined with FG or heat-strengthened glass [1].

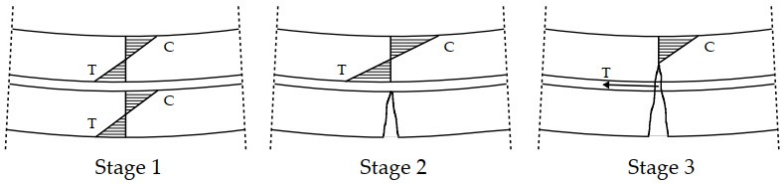

Figure 2.17 Image of breakage behaviour and stress distribution of LG in three stages: T stands for tension and C for compression [10]

Various studies have shown that LG with larger fragments when fractured exhibits better post-breakage behaviour than LG with smaller fragments [2, 5, 60]. This is illustrated in Figure 2.18, which demonstrates that LG made with annealed glass exhibits the highest post-breakage performance because it fractures into large fragments. Despite this, it offers the lowest structural performance and impact resistance before it fractures. In contrast, LG made with fully tempered/toughened glass displays the lowest post-breakage performance, primarily because toughened glass breaks into tiny fragments. However, it has the highest structural performance and impact resistance before it fractures [60].

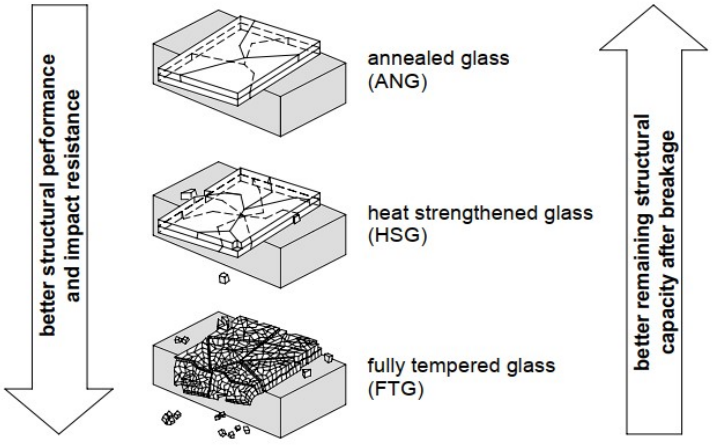

Figure 2.18 Performance of LG made with different types of glass [2]

In addition, when LG fractures, the post-failure capacity is influenced by the properties of the interlayer, which makes the stiffness and tensile strength of the interlayer an important feature for the post-breakage capacity of LG [5, 60]. The study by Feirabend et al. showed that replacing PVB with a stiffer interlayer, such as a SGP, increases the residual bending resistance of LG [100].

Therefore, the amount of weight that LG can support after it breaks depends on various factors, such as the degree of glass fragmentation, the type of interlayer used, the adhesion between the glass and the interlayer, the type of glass and the laminating method [1,5].

2.10 Mechanical Tests

This section looks into a comparative exploration of mechanical testing methods commonly used in assessing the fracture strength of glass materials. Three key tests are covered here: the three-point bend test (TPBT), the four-point bend test (FPBT), and the ring-on-ring (ROR) test.

2.10.1 Three-Point Bend Test (TPBT)

The TPBT is one of the methods used to assess the fracture strength of materials like glass. To conduct this test, a material specimen is positioned horizontally on two support points, creating a simple beam setup. A load is applied perpendicular to the surface of the specimen at a single point located at the midpoint between the two supports, creating a bending action. The setup measures how much force the material can withstand before it breaks or deforms [17, 28]. Figure 2.19 shows the bending beam analysis for the three-point bend test. The highest bending stress is typically located under the loading point [7, 101].

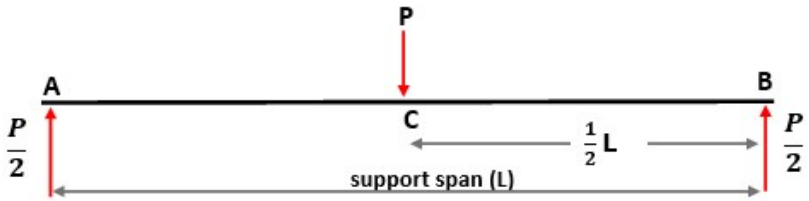

a. Free body diagram

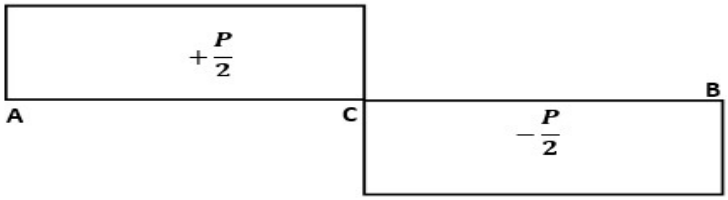

b. Shear force diagram

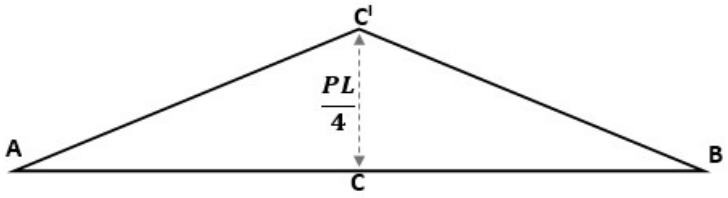

c. Bending moment diagram

Figure 2.19 Bending beam for analysis of three-point bend test

where:

P = the applied load,

L = the support span.

The formula for flexural strength is derived from the theory of bending of beams, and is defined as:

$$\sigma = \frac{Mc}{I} \tag{2.1}$$

where :

M = the maximum bending moment,

c = the distance from the centre of the specimen to the outer of the specimen (i.e., distance from the neutral axis),

I = the moment of inertia of the cross-section.

For a bar with a rectangular cross-section, the following can be applied:

$$c = \frac{h}{2} \tag{2.2}$$

where :

h is the thickness of the specimen

$$I = \frac{bh^3}{12} \tag{2.3}$$

where:

b is the width of the specimen.

From the bending beam diagram in Figure 2.19, the maximum bending moment for TPBT is at point C' and the maximum bending moment can be calculated as:

$$M = \frac{PL}{4} \tag{2.4}$$

Substituting equations 2.2, 2.3 and 2.4 into equation 2.1, the following equation is obtained:

$$\sigma = \frac{\left(\frac{PL}{4}\right)\frac{h}{2}}{\frac{bh^3}{12}}$$

$$\sigma = \frac{3PL}{2bh^2} \tag{2.5}$$

The flexure strength of the specimen subjected to the three-point bend test can be determined with Equation 2.5.

2.10.2 Four-Point Bend Test (FPBT)

In a FPBT, the load is applied to the specimen at two points symmetrically between two supports. The shear force diagram (SFD) and the bending moment diagram (BMD) for this loading configuration are shown in Figure 2.20. The shear force is zero between the two load points in the central section because the applied loads are equal and symmetrically distributed. The bending moment increases linearly from the supports toward the load points but becomes constant in the central section. This constant bending moment in the middle region is a unique feature of the FPBT, differentiating it from the TPBT, where shear forces are present throughout the specimen. The absence of shear force in the middle region of the FPBT indicates that the stresses are purely due to bending. This means that the central section experiences only normal stresses from bending, with compressive stress on the top surface and tensile stress on the bottom surface [91, 102]. This makes the FPBT ideal for analysing flexural strength, as the central section experiences a uniform stress state, isolated from the influence of shear forces.

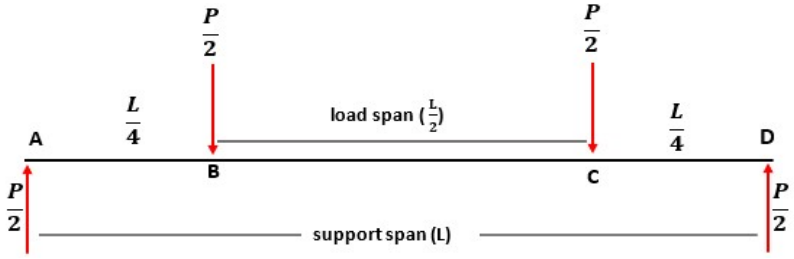

a. Free body diagram

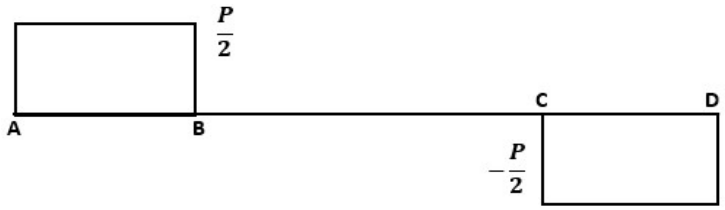

b. Shear force diagram

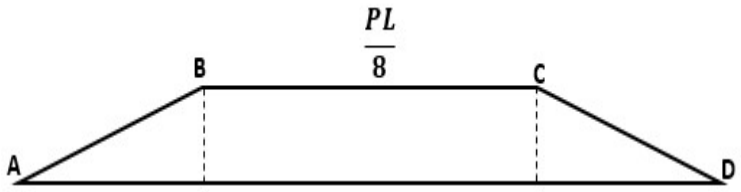

c. Bending moment diagram

Figure 2.20 Bending beam analysis of the FPBT set-up

From the bending beam diagram in Figure 2.20, the maximum bending moment for FPBT is from point B to point C, and the maximum bending moment can be calculated as:

$$M = \frac{PL}{8} \tag{2.6}$$

Similarly, by substituting equations 2.2, 2.3, and 2.6 into equation 2.1, the following equation is obtained:

$$\sigma = \frac{\left(\frac{PL}{8}\right)\frac{h}{2}}{\frac{bh^3}{12}}$$

$$\sigma = \frac{3PL}{4bh^2} \tag{2.7}$$

Therefore, the flexure strength of the specimen subjected to the FPBT can be determined using Equation 2.7. This equation is only valid when the load span is equal to half the length of the support span, which is the condition considered in this study. This equation is also the FPBT flexural stress equation outlined in the ASTM C1158-02 standard [103].

Ravimony et al. [79] performed FPBT on LG beams, shown in Figure 2.21, to study the load-deflection behaviour and fracture patterns. It was found that the LG exhibited linear

load-deflection behaviour until the initial fracture load was reached, followed by residual load-carrying capacity and safety fracture behaviours. The specimens used in the study measured 700 × 100 mm. The test involved a 200 mm loading span and a 600 mm support span. Rubber pads were placed at each contact point between the rollers and the specimen to ensure uniform load distribution. During the FPBT, the initial fracture occurred in the lower glass layer. Subsequently, the load is transferred to the upper glass layer through the polymer interlayer [96].

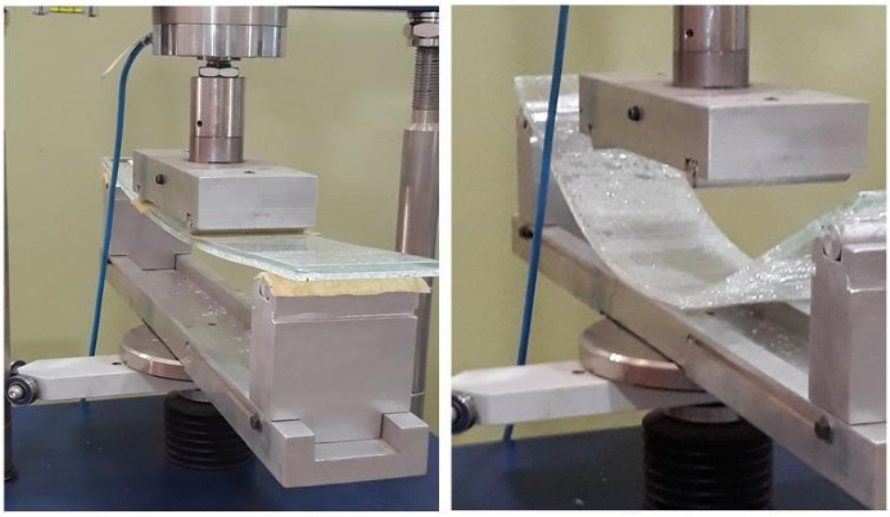

(a) During loading (b) After failure

Figure 2.21 Photograph of LG specimen under four-point bend test [79]

Figure 2.22 displays a typical glass fracture in FPBT. It was recorded that the fracture initiation occurred in two distinct locations: (a) at the edge, where a crack branched out from a point at the edge, and (b) at the centre, where a crack initiation occurred at the surface of the specimen.

a. fracture at the edge **b.** fracture at the face

Figure 2.22 Photographs of typical glass fracture in FPBT [7]

2.10.3 Ring-on-Ring (ROR)

In the ROR test, a specimen is placed in between two concentric rings of varying diameters [104, 105], as shown in Figure 2.23. The specimen is subjected to a gradually increasing load until it fractures. This test provides a consistent and reliable method to evaluate the fracture strength of glass without interference from edge micro-flaws [10, 104, 105].

The stress state in the loading ring of the ROR test and the stress state in the region between the point loads in the FPBT share similar characteristics. In both cases, the shear stress in these regions is zero due to the symmetry of the loading, and these sections are purely subjected to bending forces. Additionally, in both cases, the maximum compressive stress occurs at the top surface, where the material is compressed by the bending moment, while the maximum tensile stress occurs at the bottom surface, where the material is being pulled apart by the bending moment. These regions can be directly compared in terms of stress behaviour, which is important when analysing failure characteristics.

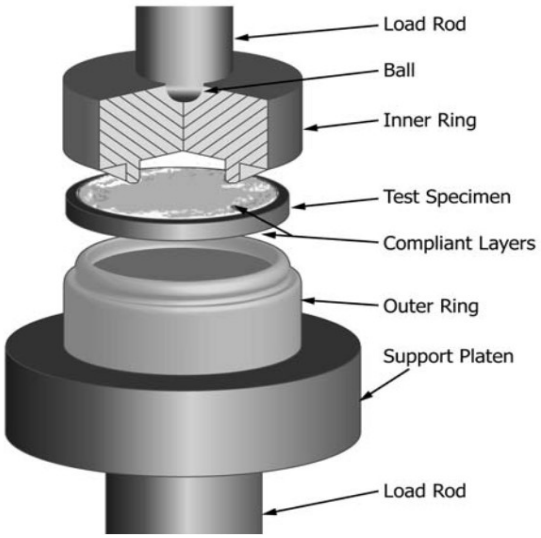

Figure 2.23 Diagram of the perspective view of the ROR test [106]

The ROR test is ideal for creating a nearly uniform equibiaxial stress condition within the centre of the specimen [7, 76, 107]. This is important for materials like glass, which are highly sensitive to micro-cracks. The ROR test can minimise the influence of specimen edge micro-flaws on the strength measurements [10, 104]. In the four-point flexural test, the edge fracture initiation of the specimen can influence the results, which often produce misleading or inconsistent data [104]. The ROR test places less emphasis on specimen edge quality, as the region of load application of the loading ring is far away from the edges of the specimen. Figure 2.24 shows the bending test configurations of circular plates.

The development of the governing equations for the stress state in a circular plate follows the formulation presented in [107] and is reproduced here for convenience and completeness

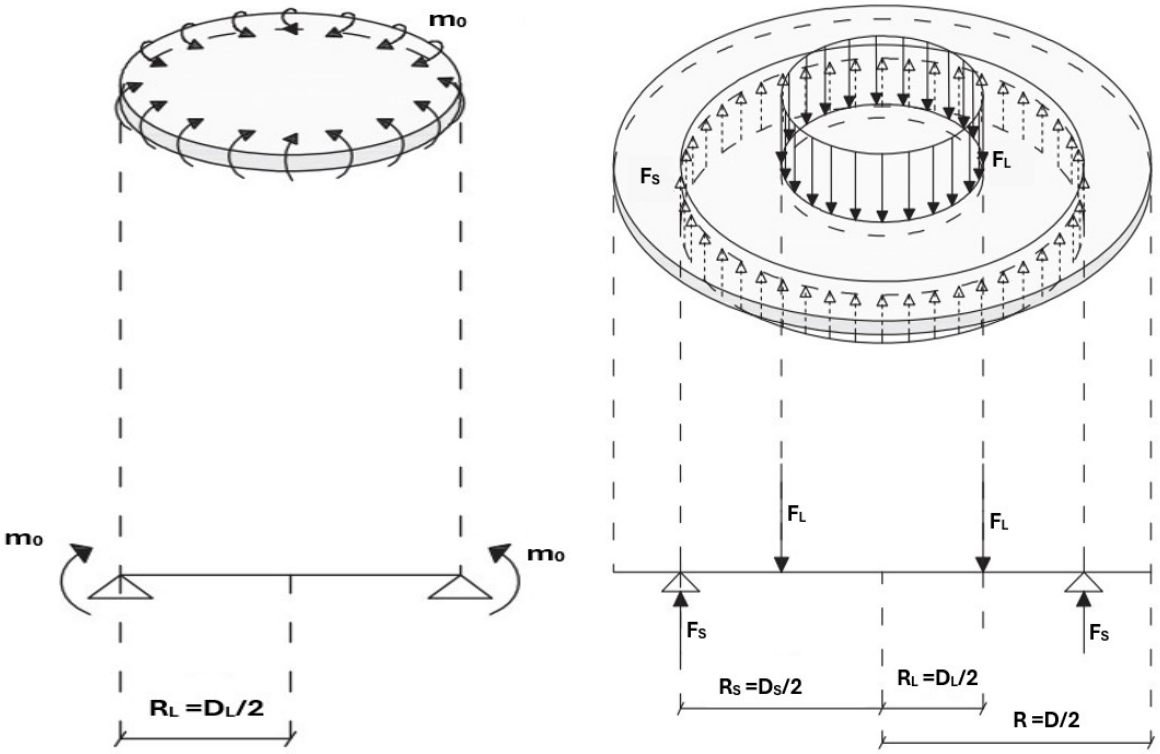

a. Circular plate subjected to bending moments along its edges

b. ROR test configuration

Figure 2.24 Bending test configurations of circular plate [107]

Considering a disk-shaped Kirchhoff–Love plate [108] with a uniform thickness (h). Let Young's modulus be E while ν is the Poisson's ratio. The bending stiffness D of the plate is defined as [107]:

$$D = \frac{Eh^3}{12(1-\nu^2)} \tag{2.8}$$

Using a polar coordinate system defined by coordinates (r, θ), with the origin at the centre of the plate, the vertical displacement is denoted as ξ. The loading and constraints are axisymmetric, leading to the vertical displacement ξ being expressed as $\xi(r)$, while shear stress in the circumferential direction equals zero. The slope of the displacement is denoted as $\varphi(r)$. The radial shear stress, denoted as t_r, can be derived from static equilibrium. Integrating the classical fourth-order differential equation in $\xi(r)$ for plate bending, the vertical displacement rate is defined as [107, 108]:

$$\varphi(r) = -\frac{d}{dr}\xi(r) \tag{2.9}$$

It leads to [108]:

$$\frac{d^2\varphi}{dr^2} + \frac{1}{r}\frac{d\varphi}{dr} - \frac{\varphi}{r^2} = -\frac{t_r}{D} \tag{2.10}$$

Radial moment m_r with circumferential moment m_θ can be expressed as follows [107, 108]:

$$\begin{aligned} m_r &= -\frac{Eh^3}{12(1-\nu^2)}\left(\frac{d\varphi}{dr} + \nu\frac{\varphi}{r}\right), \\ m_\theta &= -\frac{Eh^3}{12(1-\nu^2)}\left(\frac{\varphi}{r} + \nu\frac{d\varphi}{dr}\right) \end{aligned} \tag{2.11}$$

The bending-induced radial stress σ_r with circumferential stress σ_θ (the stresses are shown in Figure 2.25) can be expressed as follows [107]:

$$\begin{aligned} \sigma_r &= -\frac{E}{1-\nu^2}\left(-z\frac{d^2\xi}{dr^2} - \nu z\frac{\varphi}{r}\right) = -\frac{6}{h^2}m_r, \\ \sigma_\theta &= -\frac{E}{1-\nu^2}\left(-z\frac{\varphi}{r} - \nu z\frac{d^2\xi}{dr^2}\right) = -\frac{6}{h^2}m_\theta. \end{aligned} \tag{2.12}$$

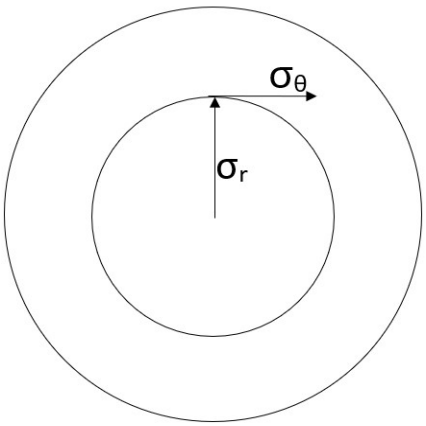

Figure 2.25 Sketch to show stresses and directions

For a circular plate with radius R_L, subjected to distributed moments m_0 at the edge as seen in Figure 2.24a, the radial shear stress $t_r = 0$ in Equation 2.10, and the boundary conditions are given as [107]:

$$\xi(R_L) = 0, \quad m_r(R_L) = m_0, \quad \varphi(0) = 0 \tag{2.13}$$

Considering the geometric condition as well as the natural boundary condition at $r = R_L$, along with the symmetry condition at $r = 0$, the function $\varphi(r)$ is found to be $\varphi(r) = \frac{1}{2}X_1 r$. Since $\frac{d}{dr}\varphi = \frac{\varphi}{r}$, the solution leads to $m_r = m_\theta = m_0$ and $\sigma_r = \sigma_\theta = \frac{6m_0}{h^2}$. Therefore,

the stress state remains constant with perfect equibiaxial throughout the specimen [107, 108].

In practice, applying bending moments that are distributed along the circular edge is challenging. This highlights the need to approximate the ideal loading condition using a ROR configuration [107]. When two rings are aligned to the centre of the specimen, placed in touch with the opposing surfaces of the specimen, and pressed against one another, the reaction forces are transmitted through the rings, assuming negligible friction, as shown in Figure 2.24b. Reaction forces transmitted through the loading ring, F_L, and support ring, F_S are:

$$F_L = \frac{P}{2\pi R_L}, \quad F_S = \frac{P}{2\pi R_S},$$

where R_L, R_S, and R are the radius of the loading ring, support ring, as well as specimen, respectively, and P is the load transmitted by the tensile tester.

By symmetry, the radial shear force t_r in Equation 2.10 becomes [107, 108]:

$$\begin{aligned} t_r(r) &= 0 \text{ for } 0 \leq r < R_L, \\ t_r(r) &= \frac{P}{2\pi r} \text{ for } R_L < r < R_S, \\ t_r(r) &= 0 \text{ for } R_S < r \leq R \end{aligned} \tag{2.14}$$

In the particular case where $t_r = \frac{P}{2\pi r}$, the solution to Equation 2.10 takes a specific form determined by boundary and matching conditions at R_L and R_S [107]:

$$\begin{aligned} \varphi(r) &= \frac{Pr}{4\pi D}\left[\log(r) - \frac{1}{2}\right] - \frac{X_1 r}{2} - \frac{X_2}{r} \\ \xi &= \frac{Pr^2}{8\pi D}\left[\log(r) - 1\right] - \frac{1}{4}X_1 r^2 - X_2 \log(r) + X_3, \end{aligned} \tag{2.15}$$

where X_1, X_2, and X_3 are defined by the limit and matching conditions.

The resulting stress state is uniform and equibiaxial within the area $0 \leq r < R_1$, thus can be expressed as [107]:

$$\sigma_r = \sigma_\theta = \frac{3P(1+\nu)}{2\pi h^2}\left[\ln\frac{R_S}{R_L} + \frac{(1-\nu)}{(1+\nu)}\frac{R_S^2 - R_L^2}{2R^2}\right]. \tag{2.16}$$

The Equation 2.16 is used to evaluate the equibiaxial strength of specimens subjected to the ROR test. This equation is adopted by both the EN 1288 [109] and ASTM 1499 standards [106].

To standardise and ensure the quality of the ROR test within the advanced ceramics community, a dedicated test methodology has been developed and approved by the American Society for Testing and Materials (ASTM). The standard methodology for the ROR test can be found in ASTM C1499-19 [106]. ASTM C1499-19 addresses critical factors such as the determination of the load ring diameter and support ring diameter ratio, specimen mid-point deflection, fracture prevention at the edge, as well as adaptability for both circular and square shape tests. However, over time, the ASTM C1499-19 standard has been compared with the European Standard EN 1288 [109]. While both standards were developed independently to ascertain the equibiaxial flexural strength of various material classes, the analysis of ASTM C1499-19 and EN 1288 shows significant comparisons. The two standards recommend the usage of similar formulas to calculate the equibiaxial strength of a circular shape (see Table 2.3). However, the ASTM standard expresses the formula in terms of diameters, whereas the European standard utilises radii. Both formulas may be adapted to determine the equibiaxial strength of shapes with rectangular or square dimensions. This is achieved through determining the diameter or radius that effectively represents the dimension of the rectangular or square shape, then incorporating this value into the formulas. The two standards offer the same specifications and guidance concerning essential aspects such as the loading machine, permissible deflection of the specimen, alignment of the specimen, load type, and the material composition of the rings. The standards also recommend the usage of thin material layers between the ring and specimen contact regions to mitigate friction and reduce stress concentrations. Despite these many similarities, it is important to acknowledge that there are certain aspects the two standards handle differently. The following sections provide the details of the differences between the two standards.

2.10.3.1 Specimen Size

EN 1288: The EN 1288 adopts a more prescriptive stance. It mandates a fixed diameter or side length of the plate, specifically either 66 mm or 100 mm. The selection between these two dimensions is influenced by the ring ratio used during the testing process [109].

ASTM C1499-19: Instead of prescribing a specific size for the test specimen, it provides an equation for finding the diameter of a circular shape plate, which depends on the thickness of the specimens. This approach ensures that the response of the plate to the load strictly adheres to the simple plate theory principles [106].

2.10.3.2 Load and Support Ring Sizes

EN 1288: The EN 1288 standard adopts a more prescriptive approach by specifying 0.2 as a constant ratio of load/support ring. The corresponding diameters of load and support ring are set to load ring diameter = 18 mm and support ring diameter = 90 mm for larger

test specimens, while for smaller test specimens, load ring diameter = 12 mm and support ring diameter = 60 mm [109].

ASTM C1499-19: This standard does not prescribe fixed ring diameters but provides an equation for calculating the load ring diameter as well as the diameters of the support rings. This equation is contingent on the diameter of the test specimen. The load ring diameter to the support ring diameter ratio is recommended to range from 0.2 to 0.5. For materials with a Young modulus $E \leq 100$ GPa as well as a failure strength $\sigma \geq 1000$ MPa, a ratio of 0.2 is specifically recommended [106].

2.10.3.3 Plate Overhang

The extension of material beyond the circumference of a support ring is known as plate overhang.

EN 1288: The precise quantity of overhang is stipulated in the European standard, a specification that accounts for the fixed dimensions of a support ring and test plate [109].

ASTM C1499-19: In ASTM standard, the overhang value of at least $\frac{D-Ds}{h} = 2$ is considered adequate. However, it indicates that when plates are cut from bigger plates or exhibit bad edge processing, a higher overhang value of no more than 12 may be necessary. Additionally, the standard acknowledges that when testing optical materials, an even larger overhang value may be required to ensure accurate results [106].

2.10.3.4 Plate Edges

The equibiaxial flexural test offers a distinct advantage by minimising stress exposure at the plate edges, consequently reducing the risk of edge initiation fracture [104]. At the edges, stress takes the form of circumferential ring stresses, which constitute only a few part of the stresses experienced at the centre of the test plate. However, it is essential to note that if large flaws exist on the edge, they can potentially trigger fractures [104]. ASTM C1499-19 includes a dedicated section on edge preparation for advanced ceramics. While EN 1288 does not delve into any issues related to the edge, aside from a brief mention in section 6.1.1 [109].

Several studies have used ASTM C1499-19 to assess the equibiaxial strength of float glass [2, 9, 10, 57, 104], despite this standard being primarily made for ceramics that are generally more resilient than glass. Interestingly, only one paper, authored by Gulati et al. [110], referenced the European standard. However, these authors did not adhere to the standard-defined ring ratio and test plate dimensions; instead, they used square plates with an edge length of 50 mm and a 0.5 ring ratio.

Table 2.3 presents a concise summary of the similarities and differences between EN 1288 and ASTM C1499-19.

Table 2.3 *Comparison of parameters for ASTM C1499-19 and EN 1288 [106, 109]*

Parameter	ASTM C1499-19	EN 1288
Strength calculation	$\sigma = \frac{3P}{2\pi h^2}\left[(1-\nu)\frac{D_S^2-D_L^2}{2D^2} + (1+\nu)\ln\frac{D_S}{D_L}\right]$	$\sigma = \frac{3P}{2\pi h^2}\left[(1-\nu)\frac{R_S^2-R_L^2}{2R^2} + (1+\nu)\ln\frac{R_S}{R_L}\right]$
Specimen type	A plate with a circular or square shape	A plate with a circular or square shape
Specimen size	Sizes are selected by using the relation $2 \leq \frac{D-D_S}{h} \leq 12$ to ensure that the simple plate theory is adhered to.	66 or 100 mm as diameter or side length
Load/support ring ratio	0.2 to 0.5 but material that has $\sigma \geq 1$ GPa and $E \leq 100$ GPa, 0.2 ratio can be used	Set at a constant value of 0.2 for both specimen size parameters.
Plates overhang	$\frac{D-D_S}{h} \geq 2$	Fixed
Plate edges	Guides on edge preparation and include schematics of both valid and invalid fracture patterns.	No details provided

Note: P = Failure load; ν = Poisson's ratio; h = Thickness; D = Specimen diameter or equivalent diameter for rectangular or square shapes; D_L = Load ring diameter; D_S = Support ring diameter; R = Specimen radius or equivalent radius for rectangular or square shapes; R_L = Load ring radius; R_S = Support ring radius.

Emmanuella and Castori [76] conducted an experiment using the ROR test to assess the equibiaxial strength of float glass. The specimens were subjected to stress via an inner ring positioned away from the edges. This arrangement created a uniform stress state in the region defined by the inner ring. The primary goal of the test was to prevent edge micro-flaws, which may have been introduced during the glass-cutting process, from influencing the equibiaxial strength measured by the ROR test. Figure 2.26 displays the ROR setup.

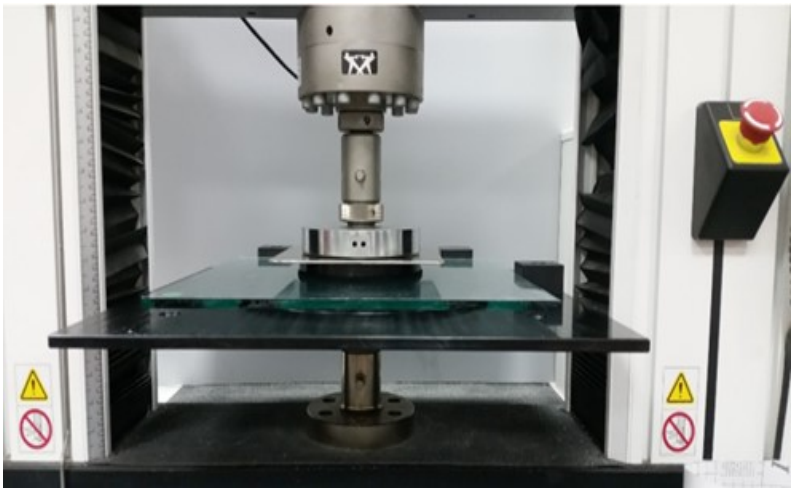

Figure 2.26 Photograph of ring-on-ring test on FG specimen [76]

Figure 2.27 displays the type of fracture patterns that are common in the ROR test. The test revealed a brittle fracture mechanism. Generally, fractures originate either within the loading span or just beyond it, where the highest principal stresses are present, and then rapidly spread outward. As the fracture propagates, the size of the fracture fragments progressively increases from the centre toward the edges.

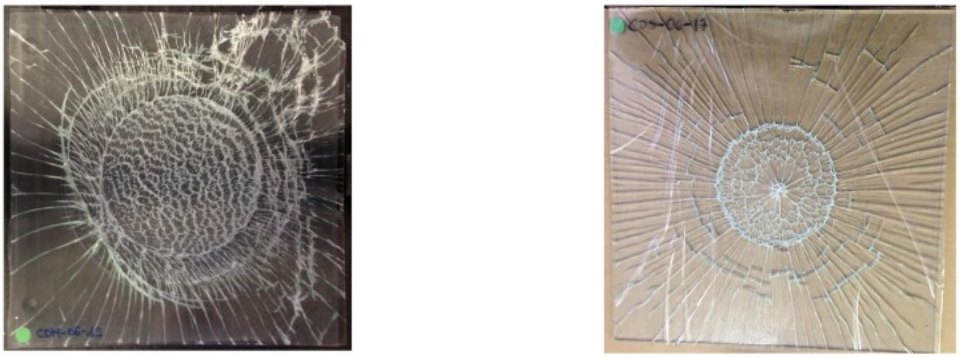

a. Failure initiation outside the loading ring region

b. Failure initiation within the loading region

Figure 2.27 Images of crack pattern from ring on ring test

There is a discrepancy between the strength generated through the FPBT and the ROR test. For instance, in the work conducted by De Pauw [105], it was noted that the glass fracture strength measured by the ROR test is three times higher than that of the FPBT. The reason he provided for this is related to the region of loading in each test. He noted that the ROR loading region is far from the specimen edge, where micro-flaws might have influenced the glass failure, while the edge micro-cracks in the FPBT are exposed to the load applied during testing.

2.11 Fracture Toughness of Glass

An isotropic linear elastic continuum model can be applied to glass with a surface crack. In continuum stress analysis, crack surface displacements are categorised into three distinct modes [4]. These modes, depicted in Figure 2.28, represent different ways a surface crack can progress to failure. The first mode, Mode I (opening mode), involves a load perpendicular to the flaw plane. Mode II (sliding mode) is characterised by shear stress, which acts parallel to the crack plane. The third mode, Mode III (tearing mode), involves out-of-plane shear forces [111]. When glass is subjected to uniform stress, the resulting failure can be classified as Mode I [4]. In this scenario, the crack grows as a result of tensile stresses at the crack opening.

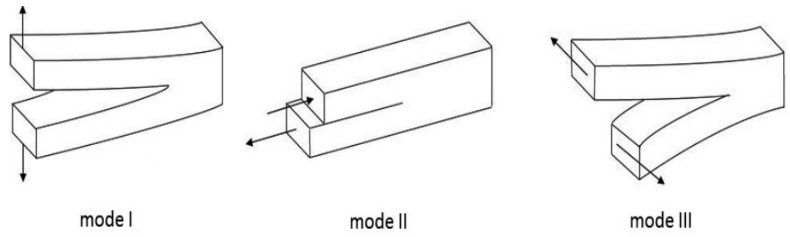

Figure 2.28 Images of micro-crack opening mechanisms [4]

Irwin developed a principle [111], that expresses stress intensity factor (SIF). This factor helps explain how flaws influence failure stress by representing the elastic stress intensity close to the crack's tip. For Mode I loading, Irwin defined the SIF as:

$$K_I = Y\sigma\sqrt{\pi a} \tag{2.17}$$

"a" is the flaw size, which is the distance between the surface of the material and the deepest point of the micro-flaw. "σ" is the stress distributed evenly over a plane parallel to the fracture plane, acting in a direction perpendicular to this plane [111]. "Y" is the geometry factor, which is a dimensionless constant that depends on the geometry of the micro-crack and the loading conditions (e.g., a value of 1.12 is applied for a typical surface micro-flaw [2, 111], 0.713 for a semi-elliptical shaped micro-flaw on a bending component [2,4], 0.637 pertains to an elliptical micro-flaw [2], and 0.722 for a quarter-circle micro-flaw on glass edges [112]).

Fracture is observed when the stress intensity factor surpasses a critical threshold, known as K_{IC}, this is as well referred to as fracture toughness [4]. The stress at which failure occurs can be expressed using three key parameters: the fracture toughness (K_{IC}), the depth of the crack (a), as well as a geometry factor (Y).

Fracture toughness is a term used to quantify a material's resistance to fracture. Lindqvist [4] reported that the fracture toughness value for soda-lime glass ranged between $0.72\,\mathrm{MPa}\sqrt{\mathrm{m}}$

and $0.82\,\mathrm{MPa}\sqrt{\mathrm{m}}$. Nevertheless, for this research, the value of $0.75\,\mathrm{MPa}\sqrt{\mathrm{m}}$ for soda-lime silica glass will be adopted, in line with Porter's report [112]. Haldimann [2] describes the concept of the SIF with its variation.

Although the stress state in the ROR test is biaxial, the general principles of crack propagation and failure in brittle materials still hold. Glass, being a brittle material, often fails through Mode I crack growth, where tensile stresses cause the cracks to propagate [4]. Cracks in brittle materials typically initiate and propagate in a manner consistent with Mode I failure [4, 113]. This suggests that fracture mechanics, which relies on models developed for uniaxial stress states, particularly Mode I failure for glass, can still provide meaningful information about the failure mechanisms of glass under biaxial stress conditions. Kinsella and Serrano used the Mode I model for glass flaw size subjected to a biaxial stress state [114].

Duan et al. [115] presented a mathematical model for calculating stress intensity factors (SIFs) for Mode I cracks subjected to biaxial loadings. This provides a theoretical solution for an angled crack within an infinite plate. This plate is subjected to uniform tensile stresses applied in two directions, as shown in Figure 2.29. The analytical solution of SIFs for Mode I cracks under biaxial loadings is presented as [115]:

$$\mathrm{K_I} = \sigma\sqrt{\pi a}\left(B\sin^2\alpha + \cos^2\alpha\right) \tag{2.18}$$

α is the angle at which a micro-flaw is inclined relative to the horizontal plane, and B is the biaxial loading factor. For a flat crack (where $\alpha = 0$) [116], Equation 2.18 becomes Equation 2.19.

$$\mathrm{K_I} = \sigma\sqrt{\pi a} \tag{2.19}$$

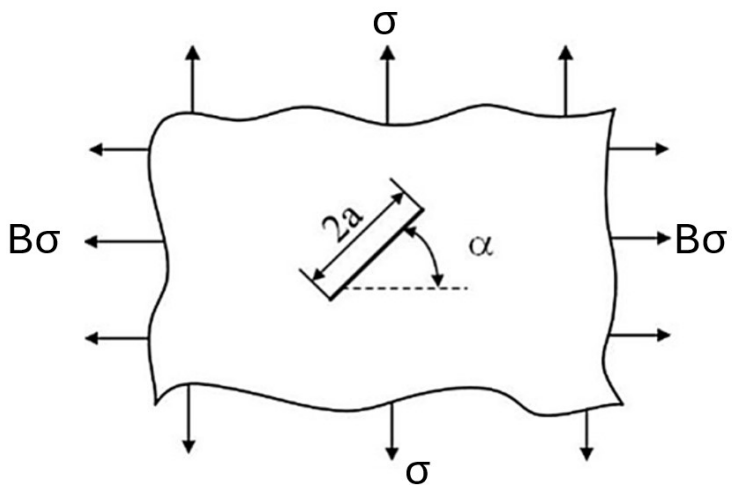

Figure 2.29 An infinite plate with an inclined flaw subjected to biaxial loading [115]

Also, Arunkumar and Nithin [116] used analytical equations from Eftis and Subramonian [117] to validate their finite element model. The model examined a plate with a centrally inclined crack under the tensile normal stress in biaxial loading (Figure 2.29). According to them, the stress intensity factor (SIF) in Mode I was analytically expressed as:

$$\mathrm{K_I} = \frac{\sigma\sqrt{(\pi a)}}{2}[(1+B) - (1-B)\cos(2\alpha)] \tag{2.20}$$

Similarly, from the analytical expression, Equation 2.20 becomes Equation 2.21 for a flat crack (where $\alpha = 0$) which is the case considered in this study.

$$\mathrm{K_I} = B\sigma\sqrt{\pi a} \tag{2.21}$$

Arunkumar and Nithin [116] specified that the B value ranges from 1 to 2. Considering a B value of 1, Equation 2.21 will be equivalent to Equation 2.19. Therefore, Equation 2.19 is adopted in this study, as it has also been used by Janssen et al. [118].

2.12 Weibull Distribution

Several statistical distributions, including normal, log-normal, and Weibull, are used to model the flexural strength of materials [111, 119, 120]. While normal and log-normal distributions are suitable for many applications, they are less effective in capturing the variability and likelihood of fracture in brittle materials [121]. The Weibull distribution is more commonly chosen for brittle materials like glass due to its ability to account for the presence of critical micro-cracks and the inherent variability in the material's strength [119, 120]. The strength is governed by flaw propagation, as described by the Griffith criterion [120]. Since glass typically contains numerous surface and edge micro-flaws that are randomly oriented, fracture occurs when the first micro-flaw reaches a critical size (according to the weakest link model) [120, 121].

The probability density function (PDF) of the two-parameter Weibull distribution can be given as [122, 123]:

$$f(\sigma) = \frac{\beta}{\eta^\beta}\sigma^{\beta-1}\exp\left(-\left(\frac{\sigma}{\eta}\right)^\beta\right) \tag{2.22}$$

Where:

the probability density function (PDF), represented as $f(\sigma)$, is the failure density function.
σ is the fracture strength.
η is the Weibull characteristic life or scale parameter. It indicates the flexural strength when 63% of specimens fail, which is commonly termed the B63.2 life [124].

β is the Weibull shape parameter, often called Weibull modulus. A β less than 1 indicates a pattern where fractures mainly occur early, while a β equal to 1 suggests a constant rate of fractures over time. When β exceeds 1, there is an increasing fracture rate as stress progresses, indicating a higher probability that fractures are more likely [120]. Kinsella and Persson [124] highlighted in their work that to observe a clear effect of β in a test, a substantial number of specimens is necessary.

The equation for the two-parameter Weibull cumulative distribution function (CDF) can be seen as [119–121, 123, 124]:

$$CDF = F(\sigma) = 1 - \exp\left(-\left(\frac{\sigma}{\eta}\right)^{\beta}\right) \tag{2.23}$$

The CDF is represented as $F(\sigma)$, which is also referred to as the probability of failure or the unreliability function. On the other hand, the reliability function, denoted as $R(\sigma)$, is also known as the probability of success or the survivor function. The reliability function for a two-parameter Weibull distribution can be defined as [119, 120, 123, 124]:

$$R(\sigma) = 1 - F(\sigma) = \exp\left(-\left(\frac{\sigma}{\eta}\right)^{\beta}\right), \quad \eta > 0, \beta > 0 \tag{2.24}$$

Figure 2.30 illustrates the relationship between $R(\sigma)$ and $F(\sigma)$ using a graphical representation of $f(\sigma)$. In Figure 2.30a, the area under the $f(\sigma)$ curve up to a point "a" is equal to the value of $F(\sigma)$ at the same point, as shown in Figure 2.30b. The total area under the fracture density function equals "a" unit.

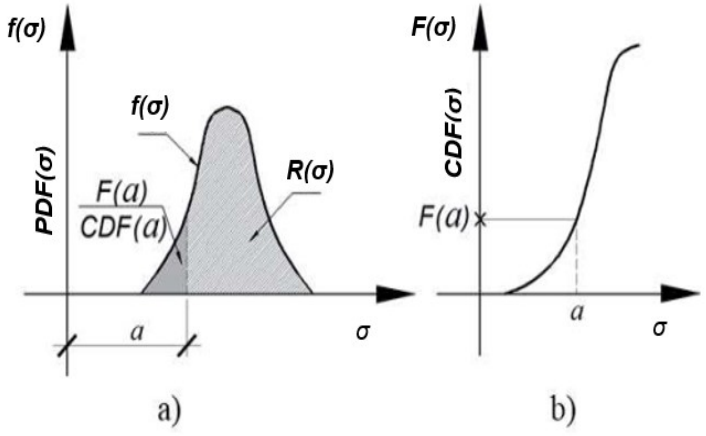

Figure 2.30 Relationship between $R(\sigma)$, $F(\sigma)$ (CDF), and $f(\sigma)$ (PDF) [121]

2.12.1 Estimation of Weibull Parameters

The linear regression method (LRM), which uses the least squares method (LSM) for estimation, is a common and simple approach for evaluating the parameters of the Weibull distribution [114, 120]. The $F(\sigma)$, representing the cumulative probability of failure up to a certain flexural strength level σ, can be transformed into a linear form resembling $y = m \cdot x + b$. This transformation is achieved by applying the natural logarithm to Equation 2.23 twice.

$$\ln\left(\ln\left(\frac{1}{1-F}\right)\right) = \beta \ln \sigma - \beta \ln \eta \tag{2.25}$$

The ordinate of the Weibull plot is given by $y = \ln\left(\ln\left(\frac{1}{1-F}\right)\right)$ where F denotes the unreliability or probability of failure. For the i-th flexural strength level, the associated probability of failure $F(\sigma_i)$ is typically calculated using the median rank method [120].

The Weibull modulus, denoted by β or m in a linear regression context, is the slope of the straight line on the Weibull plot. This slope β, also referred to as the regression coefficient, represents the tangent of the angle of inclination of the line with respect to the x-axis [120].

$x_i = \ln(\sigma_i)$, which represents the horizontal axis on the Weibull plot for the i-th fracture and is influenced by the stress parameter σ_i.

The y-intercept in the linear regression equation, represented by "b," is given as $b = -\beta \times \ln(\eta)$ where η is the scale parameter of the Weibull distribution. This y-intercept is the point where the regression line intersects the y-axis (at $x = 0$). The actual value of "b" depends on the specific values of β and η.

Chapter 3

Experimental Methodology

Two destructive tests, the four-point bend test (FPBT) and the ring-on-ring (ROR) test, are used to study the fracture strength of float glass (FG) and laminated glass (LG). Before each test was conducted, a glass surface identification was performed on each specimen. This section details the experimental design for the study, specimen preparation, and glass surface test. It also covers the set-up and procedures for the FPBT and the ROR test. All the experiments were performed at room temperature. Table 3.1 summarises the tests with the objectives.

Table 3.1 *Test summary and objectives*

Tests	Test objective
Glass surface identification:	To identify the tin-side of the FG and to confirm the continued identification of the tin-side after lamination.
FPBT:	To measure the flexural strength of both FG and LG using three different loading spans.
ROR:	To measure the equibiaxial strength of the FG and LG using three loading rings with varying diameters.

In both the FPBT and the ROR tests, the strength resulting from tensile stress is the primary focus. During the testing with a bending apparatus, the fracture initiation typically occurs on the tension side of the glass specimen. This highlights the fracture strength of the glass material. Also, for the fracture strength analysis, the study does not exclude any specimens based on the location of the fracture, although a larger number of specimens still fractured within the loading region. While some researchers do not document the exact site of the breakage [122,125], others disregard the data if the fracture occurs outside the specified loading region [2,76]. Reid [126], critiqued the practice, emphasising that fractures outside the loading region represent genuine physical events that cannot be eliminated in an experiment, highlighting the inherent variability in glass strength. This viewpoint is further supported by Natividad et al. [127]. The study on numerous large

panes subjected to bending tests revealed that none fractured at the peak principal tensile stress location. In reality, fractures may occur outside the designated loading region. Therefore, dismissing such data might not be the most robust approach.

3.1 Experimental Specimens Preparation

The two commercial soda-lime glass materials (float glass and laminated glass) obtained from Glasfit Industries in Cape Town are used in all the tests. The FG had a 6 mm nominal thickness (h), whereas the LG had a slightly greater thickness of 6.38 mm. The LG is composed of two FG sheets, each with a thickness of 3 mm, bonded together by a PVB interlayer thickness of 0.38 mm. Figures 3.1 and 3.2 illustrate the typical specimens for the FPBT and the ROR test, respectively.

Figure 3.1 FG specimen for FPBT

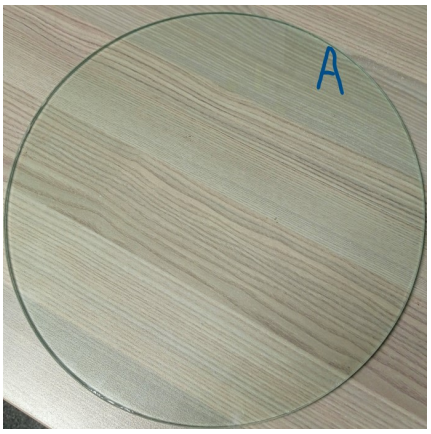

Figure 3.2 LG specimen for the ROR test

The diameter of the ROR specimen (D) was set in accordance with the ASTM C1499-19 standard, which specifies the relationship $2 \leq \frac{D-D_S}{h} \leq 12$, as presented in Table 2.3. The FPBT specimen dimensions were selected to ensure that the area over which flaws occur covered by the loading spans in both the FPBT and ROR tests is similar in magnitude. The area covered by the loading spans of the FPBT was calculated by multiplying the loading span ($L/2$) by the roller length (b), which corresponds to the specimen width. Similarly, the area covered by the loading spans in the ROR test was calculated using the formula $\frac{\pi}{4}(D_L)^4$, where D_S is the support ring diameter, h is the thickness of the specinem, L is the support span and D_L is the loading ring diameter.

For the FPBT, rectangular strips of FG and LG measuring 150 × 70 mm, 300 × 70 mm, and 550 × 70 mm were carefully cut from the respective glass sheets by the supplier through a careful process of scoring and bending. For the ROR bend test, circular plates of FG and LG with a diameter of 350 mm were extracted from the core of 400 mm square glass sheets, using similar scoring and bending techniques. All edges of the specimens were manually smoothed with a 120-grit silicon carbide grinding belt to reduce the sharpness of the glass edges, thereby enhancing safety during handling. Each glass specimen was individually wrapped in brown paper to minimise potential micro-flaws during transportation and preserve the glass surface conditions. The specimens remained in the "as received" state, without coatings or treatments applied prior to testing. The detailed dimensions and quantities of the glass specimens used for the FPBT and ROR test are listed in Table 3.2 and Table 3.3, respectively.

Table 3.2 *Details of specimens used for FPBT*

Specimen description	Specimen dimensions (mm)			Number of
	Width (b)	Length (l)	Thickness (h)	specimens
FG_S	70	150	6.00	25
FG_M	70	300	6.00	24
FG_L	70	550	6.00	24
LG_S	70	150	6.38	25
LG_M	70	300	6.38	24
LG_L	70	550	6.38	25

Note: FG_S, FG_M, and FG_L refer to float glass subjected to small, medium, and large loading spans, respectively. Similarly, LG_S, LG_M, and LG_L represent laminated glass under small, medium, and large loading spans, respectively.

Table 3.3 *Details of specimens used for ROR test*

Specimen description	Specimen dimensions (mm)		Number of
	Diameter (D)	Thickness (h)	specimens
FG_S	350	6.00	22
FG_M	350	6.00	23
FG_L	350	6.00	23
LG_S	350	6.38	25
LG_M	350	6.38	25
LG_L	350	6.38	25

Prior to testing, all specimens were visually inspected for physical defects, and none were found. The specimens were then cleaned with acetone using a non-abrasive cloth to remove any contaminants. Clear contact adhesive film (a 0.05 mm thick adhesive plastic material) was affixed to the compression surface of each FG specimen to accurately identify the fracture initiation point and capture fracture fragments, as specified in Section 9.3 of the ASTM C1499-19 standard [106]. The film was wide enough to fully cover the compression surface of the test specimen, with any excess trimmed to prevent interference or handling issues. In contrast, the LG specimens did not require contact film due to the presence of an interlayer.

3.2 Glass Surface Identification

The side of the glass that comes into contact with the molten tin is commonly referred to as the tin-side and is weaker than the opposite side of the glass, known as the air-side. Therefore, it is necessary to differentiate the glass surfaces by identifying either the tin-side or the air-side of the glass so that all the specimens can be tested in the same way to prevent any biased experiments. The glass surface identification is also used to confirm that the tin coating on the glass remains identifiable after lamination.

Two methods were explored to identify the tin side of the glass: the water-drop method and the use of ultraviolet (UV) light through a tin-side detector device. The two techniques fall under the category of non-destructive tests, as they allow for the assessment of material properties without causing any damage. Glass surface identification of all the glass materials listed in Table 3.2 and Table 3.3 were carried out, with the identified air-side labelled as 'A', using a marker as shown in Figure 3.1 and Figure 3.2. All the specimens

tested in the study were positioned with the air-side facing downward, which is the tensile side during loading.

3.2.1 Water Drop Method

The water drop method involves placing a water droplet on different sides of the glass to identify the air-side, which exhibits greater hydrophilic (water-attracting) properties, causing the water to spread and cover a larger region. Before the water droplet, the glass surface was cleaned with acetone. A water droplet was then carefully placed on each side to observe the characteristics and behaviour of the surfaces.

The water drop technique conducted on the glass did not yield enough visual evidence to effectively distinguish between the surfaces of the glass, which suggests that this particular method may not be suitable for the accurate identification of the air-side of the glass, at least based on the procedure used in the study. As a result, an alternative method or additional test is necessary to accurately identify and distinguish the sides of the glass.

3.2.2 Ultraviolet Light Method

The ultraviolet light method involves the use of short-wave ultraviolet (UV) light through a tin-side detector device, which induces visible fluorescence on the tin-side of the glass. A UV light device (Make: Bohle; Model: B05164612) was used, with a wavelength of 254 nm and a power rating of 6 volts. Figure 3.3 shown the tin-side detector device.

Figure 3.3 Picture of a tin-side detector UVG 4 (Bohle)

The glass surface identification through tin-side detector device was conducted in a darkened room to minimise external light interference, with the ultraviolet-emitting side of the tin-side detector placed on each glass surface, allowing the UV light to shine directly through the glass. A significant difference was observed between the two surfaces of the glass during the process. A noticeable reflection of the UV light was observed on one side, causing the UV light to appear brightly on the glass surface, as shown in Figure 3.4a, which signifies the tin-side. The presence of a glow on the surface confirms the identification of the tin-side. On the air-side, the light was absorbed and did not reflect off on the glass surface, shown in Figure 3.4b.

a. tin-side showing reflected light

b. air-side showing transmitted light, no reflection

Figure 3.4 Photographs of glass side identification

3.3 Experimental Design

The experimental rigs for both the FPBT and the ROR test were specifically designed and manufactured following the ASTM C158-02 [103] standard for the FPBT and the ASTM C1499-19 [106] standard for the ROR test. These rigs are all made of mild steel to minimise deformation during the loading. The FPBT rig was designed and manufactured in such a way that different loading spans can be formed by adjusting the position of the roller holder. Three different loading rings were designed and manufactured for ROR testing to create three distinct loading spans on the glass specimen. Figures 3.5 and 3.6 illustrate the assembly drawings for the experimental setups of the FPBT and ROR test, respectively. Detailed engineering drawings for both the FPBT and ROR test can be found in Appendix A. Figures 3.7 and 3.8 provide visual representations of the fabricated bar and rings, respectively.

The fabricated bar and rings are equipped with the following features:

- Roller length for FPBT (shown in Figure 3.7): 70 mm (equal to the width of the specimen)
- Roller diameter for FPBT: 10 mm
- Support ring diameter (D_S) for ROR (shown in Figure 3.8a): 300 mm
- Loading ring diameters (D_L) for ROR (shown in Figure 3.8b): 150 mm (large loading ring), 105 mm (medium loading ring), and 75 mm (small loading ring)

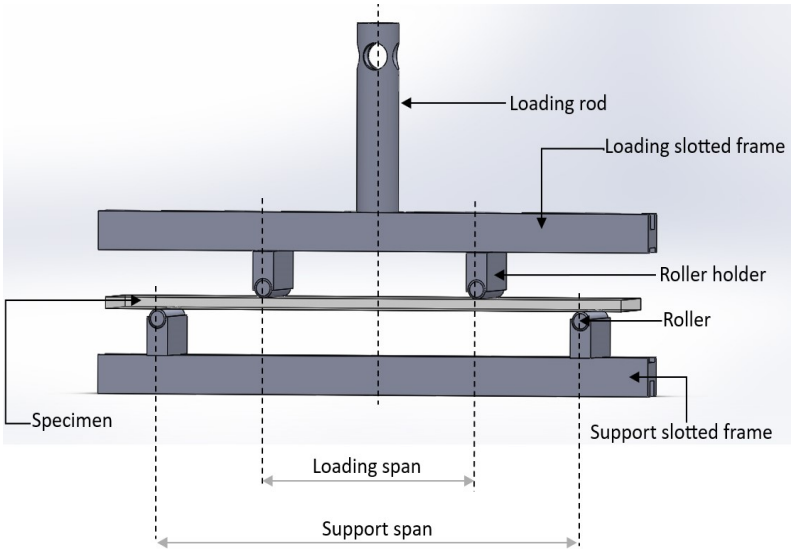

Figure 3.5 FPBT assembly drawing

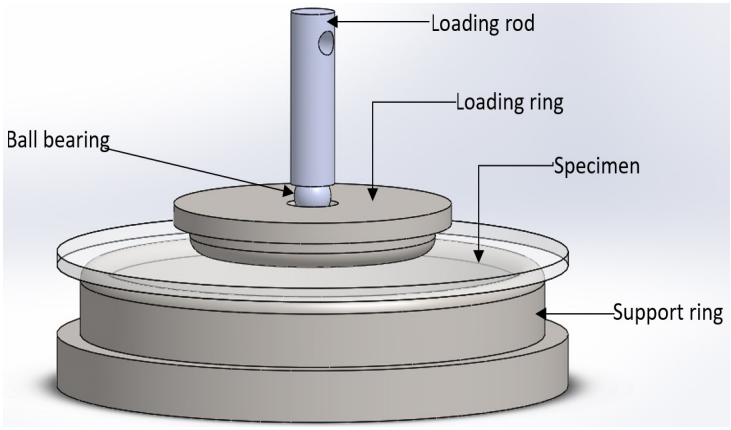

Figure 3.6 ROR assembly drawing

Figure 3.7 FPBT manufactured slotted bar

a. support ring **b.** loading rings

Figure 3.8 ROR manufactured rings

Due to the masses of the testing loading rings depicted in Figure 3.8b, there was a preload on all the ROR specimens tested. The preload was calculated based on the mass of each loading ring listed in Table 3.4. The preloads were as follows: a preload of 13 N for all specimens tested with the small loading ring, 22 N for specimens tested with the medium loading ring, and 36 N for specimens tested with the large loading ring.

Table 3.4 *Masses of the test rings*

Test Rings	Mass (kg)
ROR small loading ring	1.3
ROR medium loading ring	2.2
ROR large loading ring	3.6

The ASTM C158-02 standard required a loading rate of 1.1 MPa/min [103]. Given that Young's modulus is defined by Equation 3.1, it can be rearranged in terms of strain rate, as shown in Equation 3.2, where $\dot{\varepsilon}$ represents the strain rate and $\dot{\sigma}$ represents the loading rate:

$$E = \frac{\sigma}{\varepsilon} \tag{3.1}$$

$$\dot{\varepsilon} = \frac{\dot{\sigma}}{E} \tag{3.2}$$

To determine the strain rate range, two different values of Young's modulus, E, were used. The minimum value, E_{min}, was 50,000 MPa, while the maximum value, E_{max}, was 90,000 MPa. Substituting these values into Equation 3.2 resulted in strain rates ranging from 2.2×10^{-5} ($\dot{\varepsilon}_{\text{min}}$) to 1.2×10^{-5} ($\dot{\varepsilon}_{\text{max}}$). However, since the Zwick machine only

accepts cross-head velocity as an input, the strain rate had to be converted into cross-head velocity.

To achieve this, the ASTM standard "Standard Test Method for Flexural Properties of Polymer Matrix Composite Materials" [128] was used. According to the standard, strain (ε) for a four-point bend test can be calculated using Equation 3.3, where the strain depends on the specimen thickness h, mid-span deflection D_f, and the support span L:

$$\varepsilon = \frac{6hD_f}{L^2} \tag{3.3}$$

Considering the strain ε as a function of time $\varepsilon(t)$, then D_f must also be regarded as a function of time. This leads to the modified equation, Equation 3.4, which accounts for time-varying deflection:

$$\varepsilon(t) = \frac{6hD_f(t)}{L^2} \tag{3.4}$$

Upon deriving Equation 3.4, the deflection as a function of time translates into displacement rate (v). Then, the equation for strain rate becomes:

$$\dot{\varepsilon} = \frac{6hv}{L^2} \tag{3.5}$$

$$v = \frac{\dot{\epsilon}L^2}{6h} \tag{3.6}$$

Equation 3.6 is similar to the displacement rate equation provided in ASTM C1499-19 [106] for the ROR test. The equation is given as:

$$\dot{\delta}f = \left(\frac{D_S^2}{6Eh}\right)\dot{\sigma} \tag{3.7}$$

where: $\dot{\delta}f$ = the displacement rate of crosshead (mm/min), D_S = support ring diameter (mm), E = Young's modulus, (MPa), h = test specimen thickness (mm), $\dot{\sigma}$ = maximum normal stress rate for the test specimen (MPa/min) in the loading ring, with a recommended range between 30 and 35 MPa/min.

With the measurements used in this study, Equations 3.6 and 3.7 specify a displacement rate range from 0.005 mm/min to 1.75 mm/min. Although the Zwick machine can operate at a rate as low as 0.01 mm/min, this rate is not ideal, as the machine would struggle with data accuracy due to resolution limitations. Also, using a higher displacement rate could introduce dynamic effects that might affect the results. For these reasons, a cross-head displacement rate of 0.5 mm/min was selected, providing a balance between maintaining

data accuracy and allowing for a more thorough examination of the specimen's behaviour during the test.

3.4 Experimental Test Procedure

The FPBT and the ROR bend test were conducted using a Zwick/Roell BZC-MM14840.ZW03 Universal Testing Machine which has a maximum compression force of 200 kN and can operate at rates from 200 mm/min down to 0.01 mm/min. Force was measured using a load cell of the Zwick machine with a resolution of 0.01 N, while displacement was recorded via crosshead displacement with a resolution of 0.001 mm. The compliance of the test rig was accounted for by software adjustments. There was a consistent experimental set-up throughout all the specimens tested.

3.4.1 Apparatus Set-up and Procedures for the FPBT

The FPBT was conducted using a symmetrical four-point configuration as specified by the ASTM C158-02 standard [103]. The support rollers were set using a measuring tape to provide support spans of 126 mm, 247 mm, and 505 mm. Similarly, the loading rollers were adjusted with vernier callipers to achieve load spans of 63 mm, 123.5 mm, and 252.5 mm, as listed in Table 3.5.

Table 3.5 *Configuration values for the FPBT*

Configuration	Load span $L/2$ (mm)	Support span L (mm)	Roller/Specimen width b (mm)	Area covered by load (10^3 mm^2)	Cross-head speed (mm/min)
Small	63	126	70	4.4	0.5
Medium	123.5	247	70	8.7	0.5
Large	252.5	505	70	17.7	0.5

A silicone gasket sheet, 0.13 mm thick, serving as the compliant layer recommended by ASTM C1499-19 [106], was placed between the specimen and the roller pin to minimise friction. To ensure accurate testing outcomes, FPBT glass specimens were meticulously positioned on the respective, adjusted support spans. The loading span was set so that the distance from each support point to the nearest load point was equal and half of the load span, as depicted in Figure 3.9 - the sectional view of the fundamental fixture of the FPBT set-up. A spirit-level tool was also used to confirm that the specimen was parallel to the rollers. This alignment ensured an even distribution of the applied load, creating a uniform bending moment in the central region between the two load points. The load was applied via the mild FPBT slotted rigs, shown in Figure 3.7, with the loading rod positioned at midspan, as shown in Figure 3.5. The specimen was visually aligned with

the support and load rollers. After the setup, a plastic sheet was used to cover the testing rig to protect against flying glass fragments for safety. The setup of the FPBT is depicted in Figure 3.10.

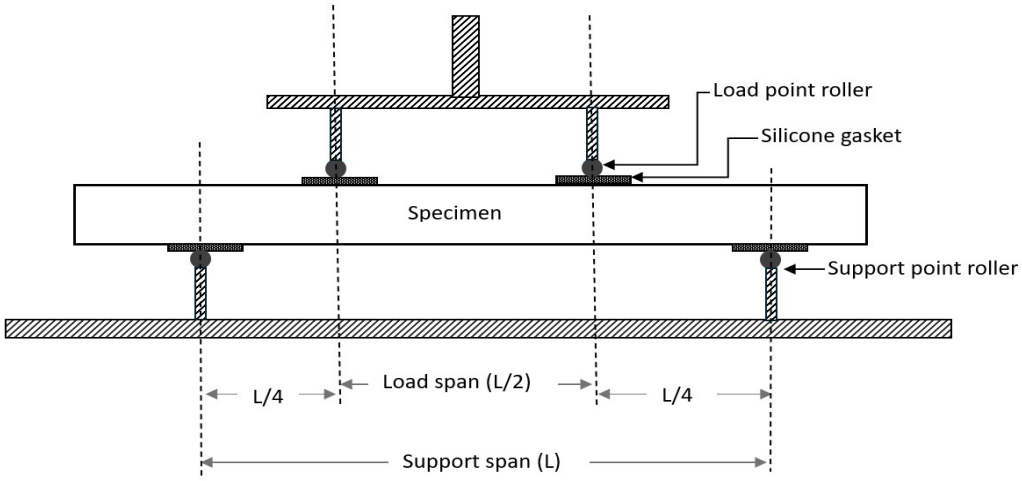

Figure 3.9 Sectional view of the fundamental fixture of FPBT set up.

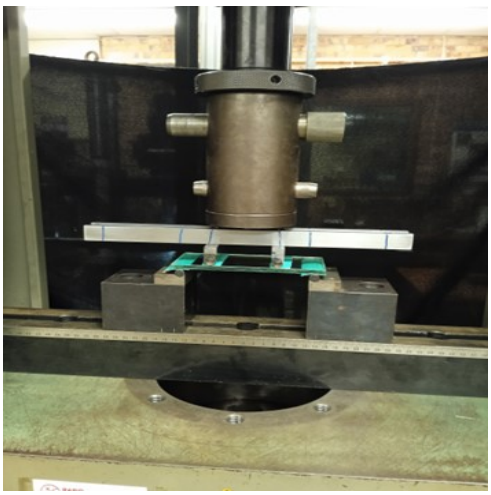

Figure 3.10 Photograph of a FPBT experimental set-up

The test commenced when the set-up was complete, providing output data regarding force (N) and displacement (mm). Upon fracture, the failure loads sustained by the specimens, along with the width, thickness, and support span of the specimen, were used to analytically calculate the fracture strengths, representing the maximum stresses that the glass materials could withstand before breaking under tension.

3.4.2 Apparatus Set-up and Procedures for the ROR Test

In the ROR testing, three different loading-to-support ring ratios were used. These ratios were in agreement with the range specified in the ASTM C1499-19 standard. The ROR test configuration is listed in Table 3.6.

Table 3.6 *Configuration values for the ROR test*

Configuration	Ring diameter (mm)		Loading-to-support	Area covered by	Cross-head
	Loading (D_L)	Support (D_S)	ring ratio (D_L/D_S)	loading ring (10^3 mm^2)	speed (mm/min)
ROR small	75	300	0.25	4.4	0.5
ROR medium	105	300	0.35	8.7	0.5
ROR large	150	300	0.50	17.7	0.5

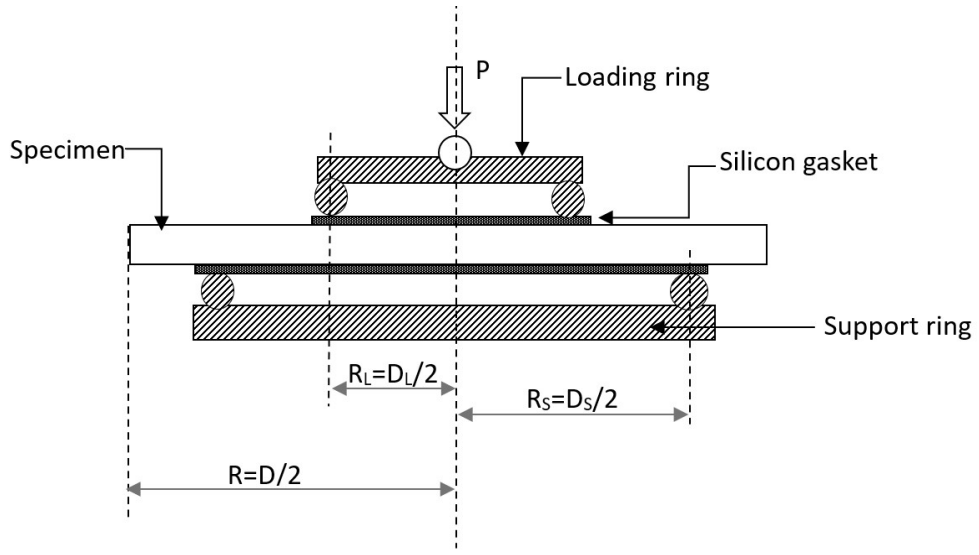

Figure 3.11 Sectional view of the fundamental fixture of ROR set up.

The ROR test set-up was assembled with the circular specimen placed between the loading ring and the support ring, which were aligned concentrically. Figure 3.11 shows the sectional view of the fundamental fixture of ROR set-up. To ensure accurate testing, the glass specimen was meticulously positioned to achieve parallel alignment when necessary, thereby ensuring that the applied forces on the circular area were perpendicular. Similar to the FPBT, a gasket sheet with a thickness of 0.13 mm, which represents the compliant layer, was placed between the specimen and the rings to reduce frictional stresses. Following guidelines from ASTM C1499-19 standard [106] a hole with a diameter of approximately $D_S/2$ was created in the middle of the compliant layer (Silicon gasket) that touches the support ring. The opening allowed exposure to the test environment. A ball bearing was

placed in the cylindrical hole at the centre of the loading ring. The loading rod of the Zwick Universal Testing Machine then applied load to the loading ring through the ball bearing, ensuring uniform loading around the line of contact. The ROR experimental setup is shown in Figure 3.12.

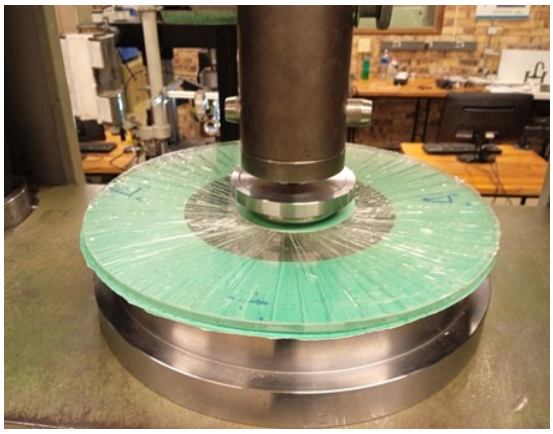

Figure 3.12 Photograph of ROR experiment set-up

The failure loads attained at the point of fracture of the specimens, as recorded by the testing machine, were used to calculate the equibiaxial strength of the specimens. A Poisson's ratio (ν) of 0.23 was used as a fundamental parameter in the fracture strength calculation, as recommended in the ASTM C1499-19 standard. Statistical analysis can further enhance the understanding of the test results, which will provide insights into the variability and reliability of the glass material.

3.5 Simulation Approach

Finite element analysis (FEA) software, specifically ANSYS version 2023R1 was used to simulate the bending test set-up for the FPBT and the ROR test. The simulation was conducted on a computer with 11th Gen Intel Core I7-1185G7 processor at 3.00 GHz and 16 GB of RAM, running a 64-bit operating system. These simulations aimed to replicate the experiment. All inputs for the simulation were standardised using the International System of Units (SI units), which ensures consistency and ease of comparison with experimental data. The glass material was assumed to be linear elastic isotropic, with a Young's modulus E of 70,000 MPa and a Poisson's ratio ν of 0.23 [129]. Similarly, the interlayer material was modelled as a viscoelastic material, with properties of Polyvinyl butyral (PVB) - Young's modulus of 220 MPa and a Poisson's ratio of 0.495 [129]. The steel for the support and loading had a Young's modulus of 210,000 MPa and a Poisson's ratio of 0.3 [105]. FG was modelled as a single-layer geometry, while LG was modelled as a composite structure consisting of glass panes and an interlayer with a bonded contact. The gasket material was omitted from the model.

A quarter-symmetry model with mirror boundaries was used in the FEA of the four-point bending simulation to save the computation time. Solid elements were used through-thickness to capture changes in normal stress. The symmetry planes were along the XY and YZ planes and the model geometry was the same as the experimental set-up shown in Figure 3.9. Frictionless contact was applied between the loading roller and the glass, as well as between the support roller and the glass. For the boundary conditions, displacement support was used, with no movement allowed in or out of the symmetry plane. A load equivalent to a quarter of the average experimental fracture force of the FPBT was applied at the nodes along the line of the load application roller. The output of interest for the FPBT simulation is the stress in the y-direction. Figure 3.13 shows the quarter-symmetry model created for the FPBT simulation, where A and B are the symmetry planes.

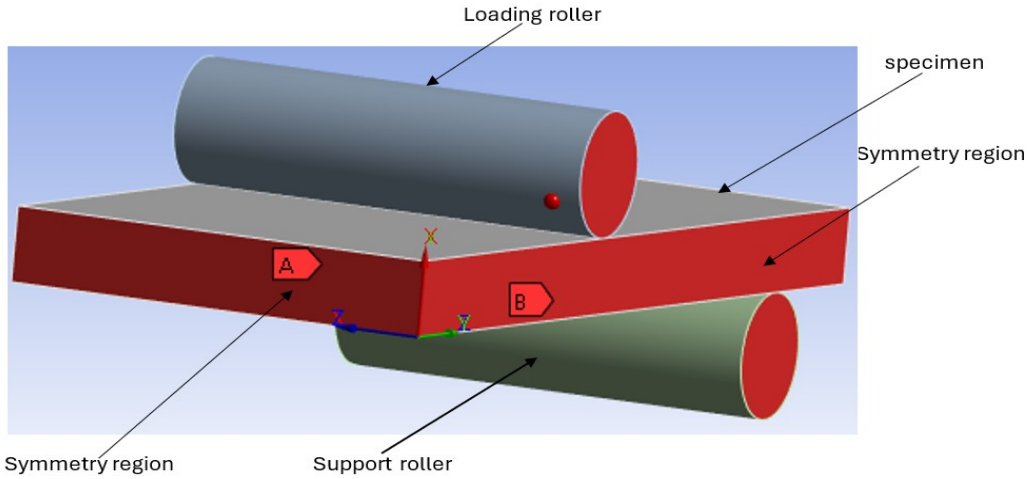

Figure 3.13 FPBT quarter symmetry

In the finite element model for the ROR simulation, a two-dimensional axisymmetric model was constructed to reduce the computation time, taking advantage of the axial symmetry of the loading ring, specimen and support ring. The axisymmetric model for the ROR simulation is displayed in Figure 3.14. The geometry model was the same as the experimental one shown in Figure 3.11. Frictionless contact was also used between the loading ring and glass as well as between the glass and supporting ring. As for the boundary conditions, displacement support was applied, with the horizontal translation and in-plane rotation set to zero. A load corresponding to the average fracture force measured in all the ROR experiments was applied to the loading ring. The output of interest here is the normal stress component in the X orientation.

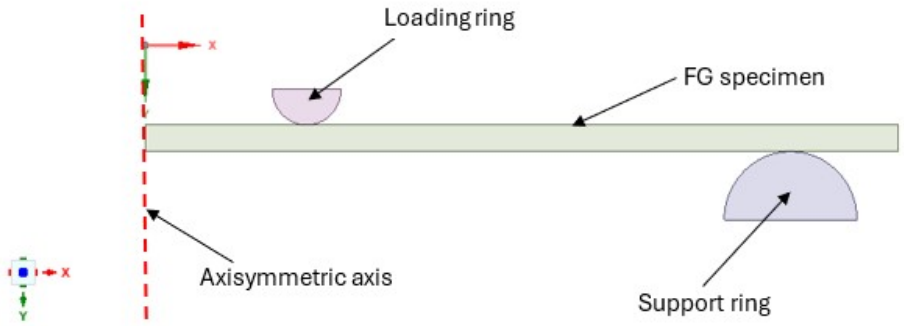

Figure 3.14 ROR axisymmetric bending test

The mesh of the glass specimen was refined until result convergence was achieved. The mesh size of the glass specimen was progressively reduced from 5 mm to 3 mm, then to 2 mm, and finally to 1 mm. Convergence of the results became evident starting at a mesh size of 2 mm. Figure 3.15 displays the typical mesh for the FPBT and the ROR simulation. The convergence plots can be seen in Appendix B.1 and B.2 for the FPBT and the ROR test, respectively.

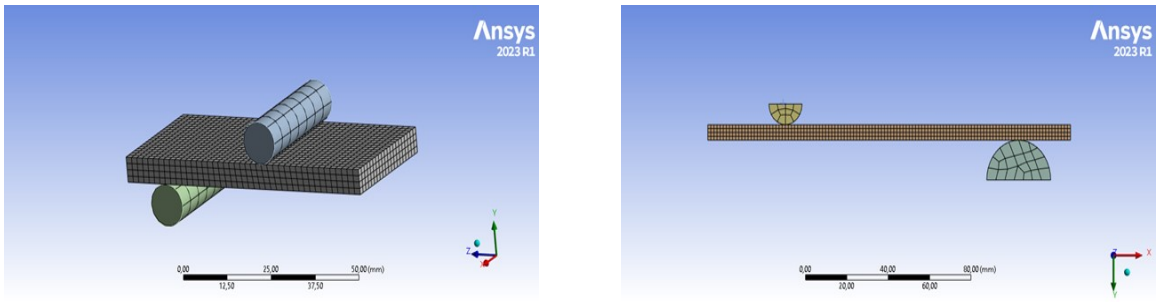

a. Quarter symmetry mesh **b.** Axisymmetric mesh

Figure 3.15 Mesh for the finite element analysis

3.6 Weibull Parameters Evaluation Process

The procedure for determining the shape parameter (β) and the scale parameter (η) of the Weibull distribution, as outlined in Equation 2.25, using experimental fracture strength data for glass specimens, is as follows:

- Measure and record the radius/width of each specimen, denoted as R or b.
- Measure and record the thickness of each specimen, h.
- Record the loading ring diameter, R_L.
- Record the support ring radius, R_S, or the outer span, L.
- Record the force at which each specimen fractures, P.

- Use the recorded fracture load and specimen dimensions to calculate the fracture strength σ_i for each specimen.
- Enter the calculated fracture strength values into an Excel sheet.
- Sort the fracture strength values in ascending order, from smallest to largest.
- Number the sorted data set from 1 to N, where N is the total number of specimens tested.
- Use Benard's approximation to calculate the median rank/ fracture probability $F(\sigma_i)$ for each specimen [121]:

$$F(\sigma_i) = \frac{i - 0.3}{N + 0.4} \tag{3.8}$$

  where i is the rank (position) of the specimen in the sorted data set. The median estimate is advantageous over the mean in skewed distributions, which are common in life data since they tend to be asymmetrical. Equation 3.8 is used primarily when $N \leq 30$; for $N > 30$, the adjustment is typically: $F(\sigma_i) = \frac{i}{N} \times 100$ [121]
- Calculate $\ln(\sigma_i)$ for each specimen.
- Calculate $\ln\left(\ln\left(\frac{1}{1-F(\sigma_i)}\right)\right)$.
- Plot $\ln(\sigma_i)$ against $\ln\left(\ln\left(\frac{1}{1-F(\sigma_i)}\right)\right)$ to generate a Weibull plot.
- Perform a least-squares fit of the plotted data.
- The slope of the least-squares fit is the Weibull modulus/shape parameter (β).
- Calculate the characteristic strength/scale parameter (η) from the y-intercept, using the relation $y = -\beta \times \ln(\eta)$.

Equations 2.25 and 3.8 were used to determine the Weibull parameters of glass at fracture in the study.

According to ASTM 1499-19 [106], the mean fracture strength $\bar{\sigma}$ and the standard deviation (SD), which quantifies the variation in fracture strength values, σ_i, can be obtained through Equations 3.9 and 3.10.

$$\text{Mean} = \bar{\sigma} = \frac{\sum_{i=1}^{n} \sigma_i}{N} \tag{3.9}$$

$$\text{Standard deviation (SD)} = \sqrt{\frac{\sum_{i=1}^{n} (\sigma_i - \bar{\sigma})^2}{N - 1}} \tag{3.10}$$

Chapter 4

Experimental Results

This chapter presents the results of the four-point bend test (FPBT) and the ring-on-ring test (ROR) conducted on float glass (FG) and laminated glass (LG). The chapter is organised into three main sections: force-displacement curves, fracture patterns of glass, and finite element analysis (FEA) output. The loading spans for both the FPBT and the ROR test cover equivalent areas. The details of the loading spans and the test configurations for the FPBT and the ROR test are provided in Table 3.5 and Table 3.6, respectively. The specifications and dimensions of the specimens tested, including the number of specimens, are listed in Table 3.2 for the FPBT and Table 3.3 for the ROR test.

4.1 Force-displacement Curves

This section presents the typical force-displacement curves of glass specimens subjected to the FPBT and ROR test. The graphs are randomly selected as representative examples; the complete set of data is available in Appendices D.1 and D.2 for the FPBT and the ROR test, respectively. All forces are measured with the tensile tester load cell, and the displacement in all cases is the cross-head displacement. All specimens were tested with the air-side facing downward. The section is subdivided into four subsections based on the types of glass and the test performed. Each subsection presents the results for the three different loading spans to which each glass type is tested

4.1.1 Float Glass subjected to FPBT

Figure 4.1 shows the typical force-displacement curves for 150 mm, 300 mm, and 550 mm long FG specimens subjected to small, medium, and large loading spans in the FPBT, respectively. Linear elastic behaviour up to the point of glass fracture is observed for all cases, as expected. At the point of fracture, the force rapidly dropped to zero. There is no indication of plastic deformation, as the curve showed no rounding before failure, indicating purely elastic behaviour. This is typical of the failure curve of a brittle material. The failure force was measured at the point of fracture. For the 150 mm long FG specimens tested under the small loading span (25 in total), the fracture force capacities range from 1009 N to 1530 N, with displacements between 0.38 mm and 0.65 mm. For the 300 mm

long FG specimens (24 in total), representing the medium loading span, the fracture loads vary from 497 N to 659 N, with displacements from 1.02 mm to 1.22 mm. Meanwhile, the fracture loads for the 550 mm long FG specimens (also 24 in total), corresponding to the large loading span, range from 181 N to 258 N, with displacements between 2.78 mm and 4.23 mm.

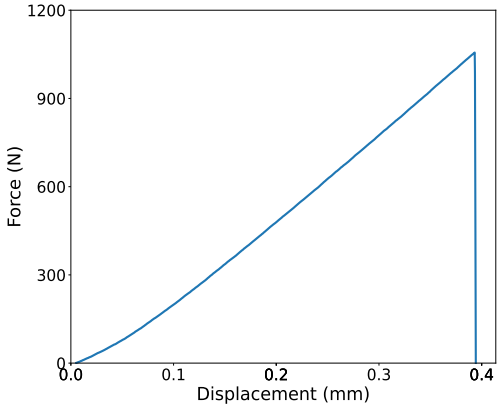

a. 150 mm long FG

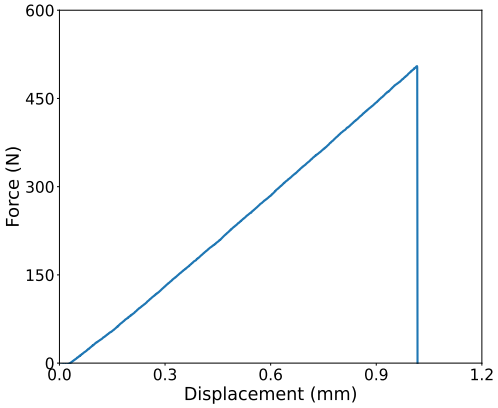

b. 300 mm long FG

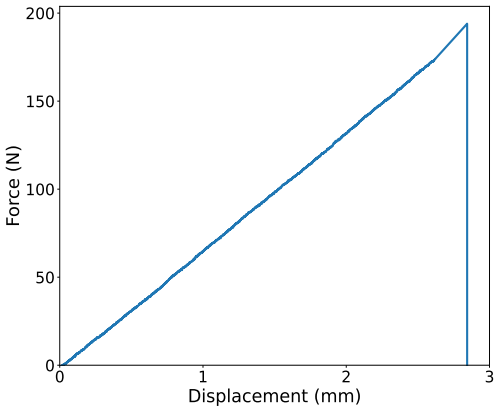

c. 550 mm long FG

Figure 4.1 Typical force-displacement curve of FG subjected to the FPBT

4.1.2 Laminated Glass subjected to FPBT

Unlike the single peak observed in the FG curve, the force-displacement curve for the LG exhibited two peaks, as shown in Figure 4.2. After the initial fracture, represented by the first peak in the graph, the load dropped; however, the load did not fall to zero. Following this first load drop, the specimen in the testing apparatus underwent another increase in load, which continued until another fracture occurred, resulting in a second peak. However, this second peak did not reach the height of the first peak.

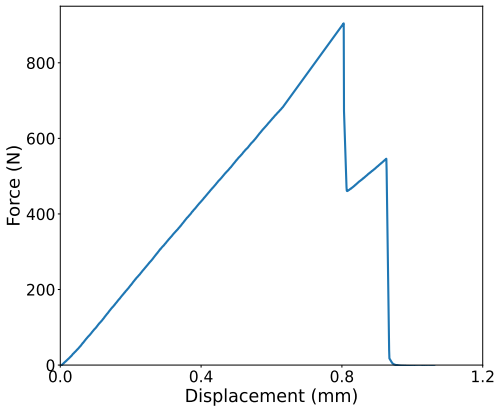

a. 150 mm long LG

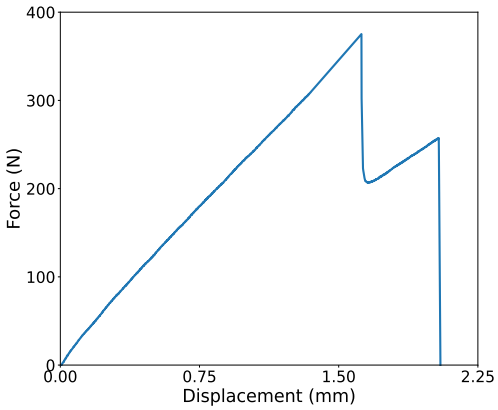

b. 300 mm long LG

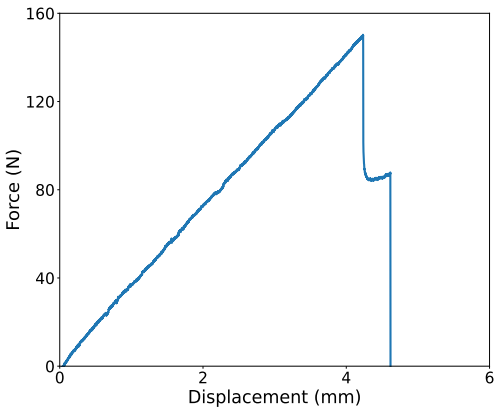

c. 550 mm long LG

Figure 4.2 Typical force-displacement curve of LG subjected to the FPBT

The two peaks observed in the LG force-displacement curve can be attributed to the two layers of glass panes in the LG specimen. Typically, the lower layer fractured first due to unconstrained tension, while the upper layer was constrained by the interlayer film, resulting in sequential fracturing of the layers. After the first fracture, the thickness of the LG carrying the load was reduced to nearly half of what it was originally, with only about half of the LG thickness contributing to the load-bearing capacity for the second fracture (considering the breakage behaviour of LG as shown in Figure 2.17). Consequently, both the distance from the neutral axis (y) and the moment of inertia of the cross-section (I) decreased.

The load at the first peak is the primary focus, as the specimens were considered to have lost their structural integrity at the point of the first fracture. At this point, the load capacities for the 150 mm long laminated glass specimens (25 in total) vary between 721 N and 982 N, with displacements ranging from 0.69 mm to 0.93 mm. For the 300 mm long LG specimens (24 in total), test results indicate load fluctuations from 300 N to 484 N, with displacements between 1.37 mm and 2.75 mm. Meanwhile, the load capacities for the

550 mm long LG specimens (25 in total) range from 122 N to 193 N, with displacements between 3.51 mm and 5.63 mm. The forces at the first fracture are higher than those at the second fracture. For instance, in Figure 4.2, the fracture force of the second fracture for the 150 mm long LG (Figure 4.2a) is approximately 61% of that of the first fracture, requiring an additional displacement of about 0.15 mm after the first fracture. For the 300 mm long LG specimens (Figure 4.2b), the force at the second fracture is around 70% of the first fracture force, with a displacement of approximately 0.5 mm following the first fracture. In the case of the 550 mm long LG specimens (Figure 4.2c), the second fracture force is about 60% of the first fracture force, with a displacement of less than 0.5 mm after the first fracture.

4.1.3 Float Glass subjected to ROR Test

Figure 4.3 displays the typical force-displacement graphs of FG specimens subjected to small, medium and large loading rings of the ROR test.

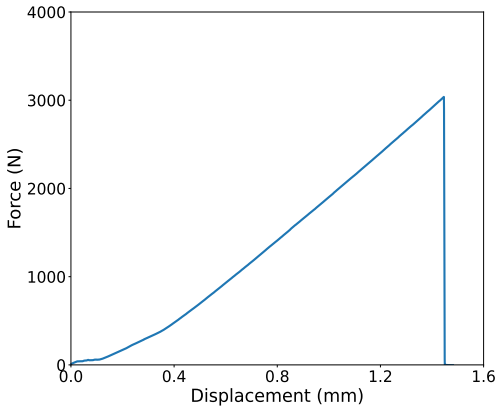

a. 75 mm diameter loading ring

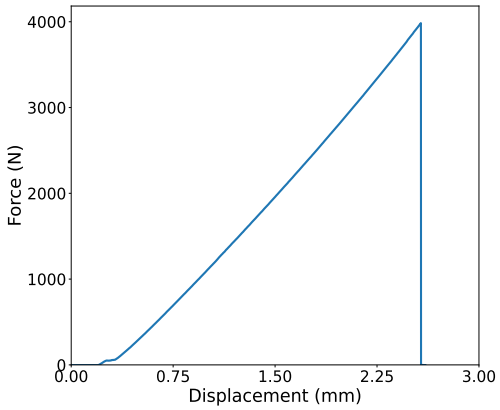

b. 105 mm diameter loading ring

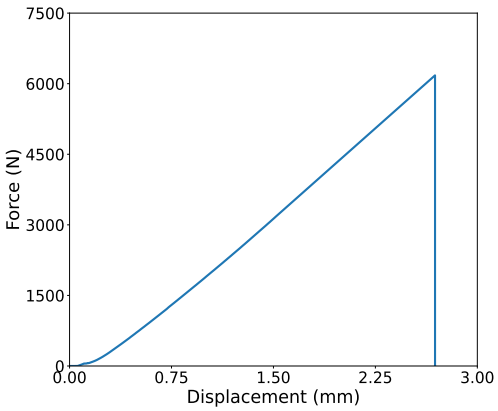

c. 150 mm diameter loading ring

Figure 4.3 Typical force-displacement curve of FG subjected to the ROR testing

The fracture loads of 22 FG specimens tested under the small (75 mm diameter) loading ring in the ROR test range from 2446 N to 4301 N, with displacements vary between 1.46 mm and 3.43 mm. Similarly, 23 FG specimens tested with the medium (105 mm diameter) loading ring display fracture loads ranging from 2510 N to 5849 N, with displacements between 1.57 mm and 3.49 mm. Additionally, for 23 FG specimens subjected to the large (150 mm diameter) loading ring, the fracture loads range from 3001 N to 6848 N, accompanied by displacements from 1.15 mm to 3.25 mm. From the force-displacement graphs of the FG specimens subjected to the ROR test (Figure 4.3), it is observed that the curve behaves similarly to that of the FG specimens subjected to the FPBT (Figure 4.1).

4.1.4 Laminated Glass subjected ROR Test

Figure 4.4 displays the force-displacement curves for LG specimens subjected to three different loading rings of the ROR test. The behaviour resembles the one observed for LG under the FPBT (Section 4.1.2).

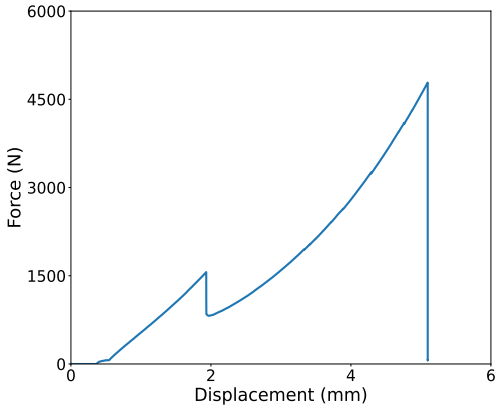

a. 75 mm diameter loading ring

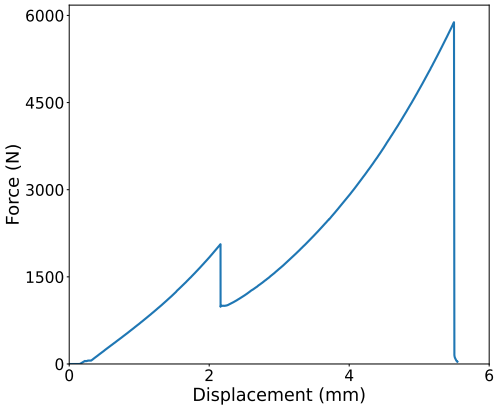

b. 105 mm diameter loading ring

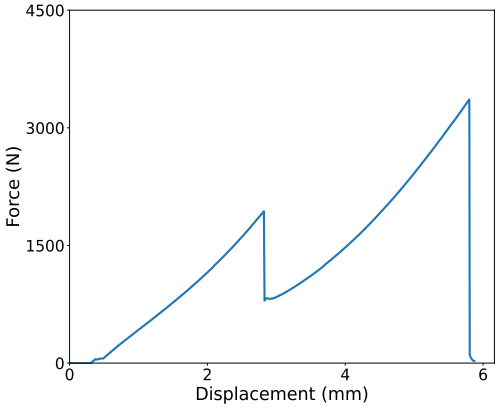

c. 150 mm diameter loading ring

Figure 4.4 Typical force-displacement behaviour of LG under the ROR testing

From the force-displacement curves of the LG specimens subjected to three various loading rings of the ROR test, the second peak of the curve is higher than the first peak in all three loading rings. In the ROR test, the mechanism changes from bending before the first peak to a punching shear-type failure, where there is interference between the fractured top and bottom layers as the loading ring travels downwards. On the ROR force-displacement graphs, after the first peak, the displacement becomes non-linear, with no stiffness reduction, as there is with the FPBT, where the reduction in stress-effective thickness exhibits a lower force-displacement slope. This characteristic differentiates the behaviour of LG specimens subjected to the ROR test from those under the FPBT. The linear slopes seen in all graphs are due to bending deformation. However, the first peak is the primary focus for calculating the equibiaxial strength. At the initial fracture, the 25 LG specimens subjected to the small loading ring of the ROR test exhibit load capacities ranging from 1062 N to 1764 N with displacements from 1.80 mm to 3.78 mm. For the 25 LG specimens tested under the medium loading ring, the observed fracture loads vary between 1093 N and 2223 N with displacements between 1.93 mm and 3.82 mm. Meanwhile, the fracture loads of the 25 LG specimens tested with the large loading ring fall within the range of 919 N to 2890 N with displacements between 2.23 mm and 3.78 mm.

4.2 Fracture Pattern Observations

The fracture of each glass specimen was investigated to identify the point of initiation and fracture pattern. A brittle fracture mechanism was consistently observed across all specimens. The fracture initiated from the bottom surface within the zero shear, maximum bending moment region, where the maximum tensile stress occurred. This is expected since the top surface was under compression while the bottom surface was under tension, as shown in Figure 2.9. Given that glass has high compressive strength but relatively low tensile strength [2, 10], it is unable to withstand significant tensile loads. It was also observed that multiple cracks can be seen in a single specimen. This is anticipated, as the bending moment remained constant across the entire central region between the loading spans and rings.

4.2.1 FPBT Fracture Pattern

The fracture initiation points for FG and LG specimens subjected to the FPBT were similar, identified as either face fracture initiation (Figure 4.5a) or edge fracture initiation (Figure 4.5b) within the loading span where the maximum bending moment occurred. Notably, edge fracture initiations were observed in the highest number of specimens tested; approximately 80% of the specimens subjected to the FPBT exhibited edge fracture initiation. This is expected, as the edges of glass specimens are more susceptible to micro-flaws introduced during the cutting process. The micro-flaws created stress

concentrations along the edge regions within the loading span, leading to higher localised stress compared to the interior surface regions. Therefore, the probability of fracture initiating at an edge is high.

a. fracture initiation on the face **b.** fracture initiation on the edge

Figure 4.5 Images of fractured glass specimens subjected to FPBT

4.2.2 ROR Fracture Pattern

Figure 4.6 shows the typical ROR test fracture patterns observed in FG and LG specimens subjected to different sizes of loading rings. Ring-shaped cracks were formed within the region occupied by the loading ring. Once a fracture initiated on the bottom surface within the loading ring or at its tip, it propagated outward in a radial direction, covering the entire surface of the glass specimen. The size of the fracture fragments progressively increased from the centre towards the edges. This pattern was also observed by Wu et al. [9] and Emmanuella and Castori [76].

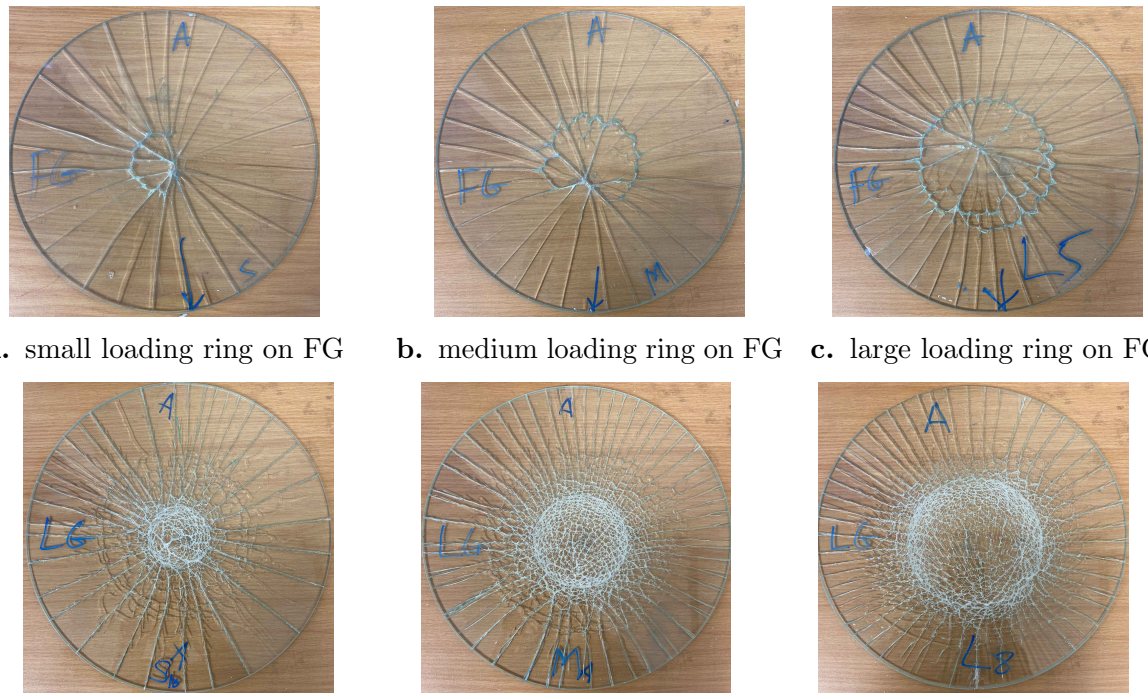

a. small loading ring on FG **b.** medium loading ring on FG **c.** large loading ring on FG

d. small loading ring on LG **e.** medium loading ring on LG **f.** large loading ring on LG

Figure 4.6 Photographs of the ROR fracture patterns for FG and LG

Figures 4.6a, 4.6b, and 4.6c show that FG specimens subjected to the ROR test fractured into relatively large fragments with ring-shaped cracks. while LG specimens produced small fragment with dense spider-web-like patterns within the region occupied by the loading ring, as shown in Figures 4.6d, 4.6e, and 4.6f. This difference is likely due to the energy absorbed by the interlayer in the laminated glass.

4.3 Finite Element Analysis (FEA) Result

The typical FEA stress and displacement plots for the FPBT and the ROR simulations are shown in Figures 4.7 and 4.8. In both figures, the maximum stresses and deformations are located in the central region of the geometry, which represents the behaviour of the experimental test. Table 4.1 gives the numerical simulation output of the glass specimens.

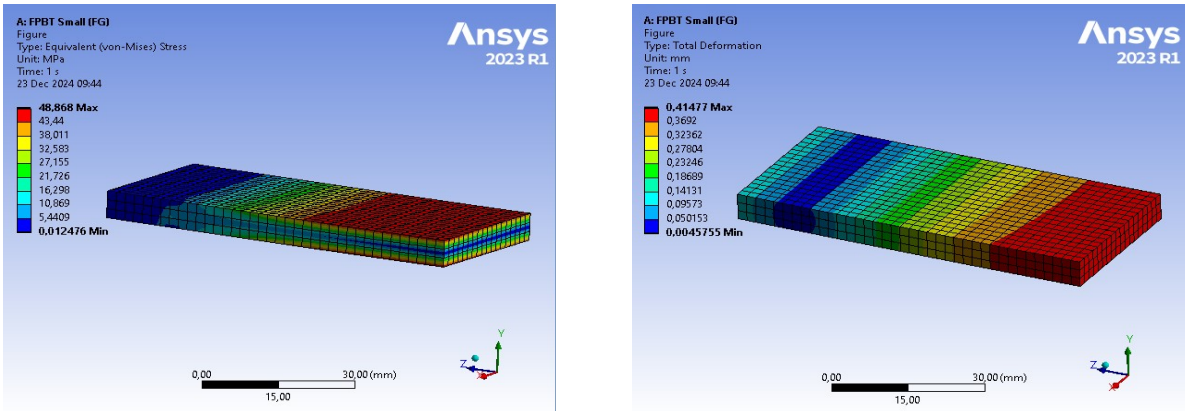

a. FPBT stress output **b.** FPBT deformation output

Figure 4.7 Typical FPBT simulation output

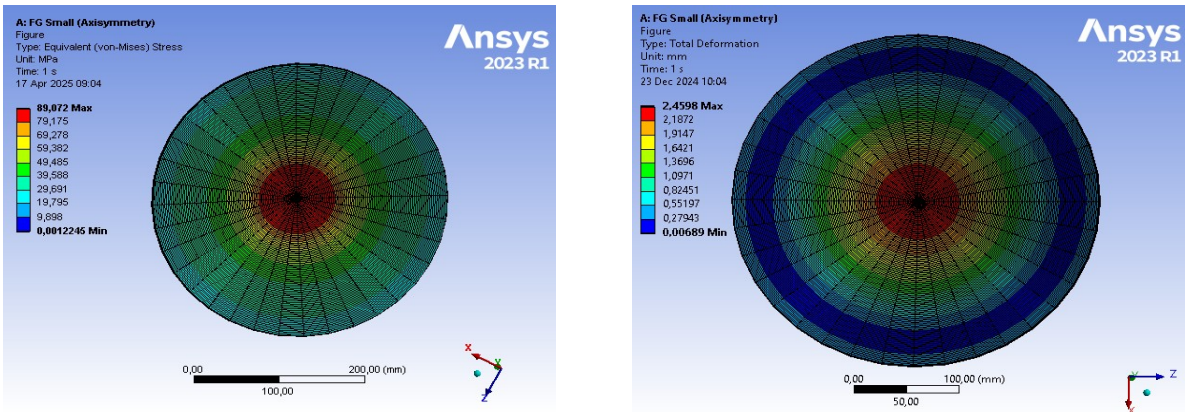

a. ROR stress output **b.** ROR deformation output

Figure 4.8 Typical ROR simulation output

Table 4.1 *Results of the FPBT and the ROR Simulations*

Test	Loading span	Float Glass		Laminated Glass	
		Maximum Stress (MPa)	Maximum Displacement (mm)	Maximum Stress (MPa)	Maximum Displacement (mm)
Four-point Bend	Small	48.9	0.4	49.2	2.7
	Medium	43.1	3.5	45.2	2.3
	Large	34.8	4.2	38.0	3.6
Ring on Ring	Small	89.07	2.5	36.6	1.0
	Medium	84.9	2.6	31.4	1.0
	Large	70.5	2.5	26.2	1.0

Chapter 5

Discussion

This chapter discusses the data obtained from the experiments, emphasising the similarities and differences between the four-point bend test (FPBT) and ring-on-ring (ROR) test regarding the focus of the study, which is the influence of loading span on the fracture strength of float glass (FG) and laminated glass (LG). It then relates the outcomes to the literature. The chapter is divided into six sections: fracture strength of glass, comparison of the FPBT and the ROR test, stress and moment relation, critical flaw sizes for glass, Weibull analysis of glass strength, and finite element analysis of glass.

5.1 Fracture Strength of Glass

This section is divided into four parts: the fracture strength of FG and LG specimens, respectively, subjected to the FPBT and the ROR test, respectively.

5.1.1 Fracture Strength of FG subjected to FPBT

Figure 5.1 presents the fracture strength values of the three different lengths (150 mm, 300 mm, and 550 mm) of FG subjected to the FPBT. The fracture strength values were calculated using the FPBT flexural stress equation, presented in Equation 2.7. The parameters used to calculate the fracture strengths for the specimens subjected to the FPBT include the fracture force from the force-displacement curves presented in Section 4.1, along with the support span, width, and thickness of the specimen, as listed in Table 3.5. The minimum, maximum, and average fracture strengths, along with the corresponding lower and upper 95% confidence intervals (CI), are listed in Table 5.1. The 95% confidence interval was calculated using the t-critical value $t_{\alpha/2,N-1}$, as shown in Equation C.1, since the sample size was small and the population standard deviation was unknown. The recorded failure loads and calculated strengths for all the specimens subjected to the FPBT can be found in Table D.1 and Table D.2.

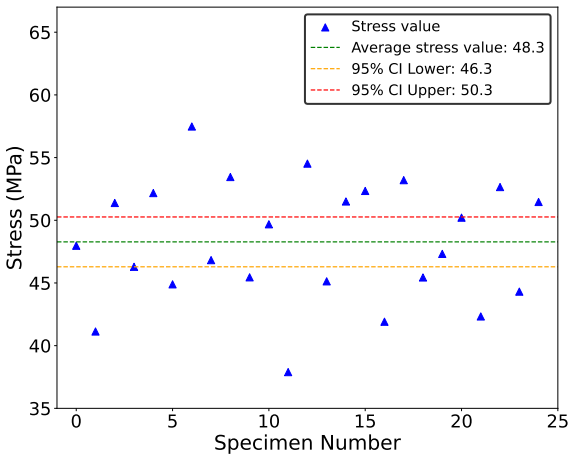

a. fracture strength of 150 mm long FG

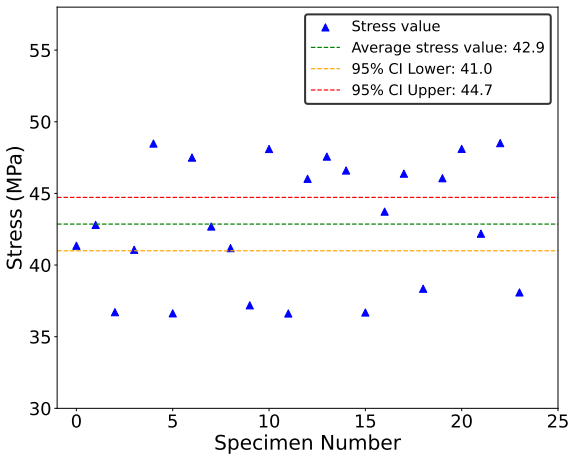

b. fracture strength of 300 mm long FG

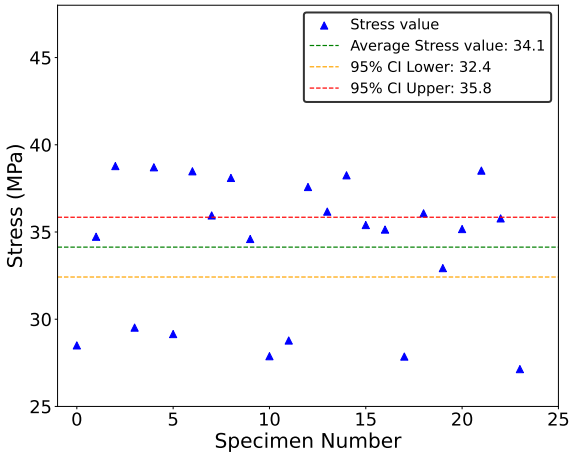

c. fracture strength of 550 mm long FG

Figure 5.1 Graphs of fracture strength of FG subjected to the FPBT

Table 5.1 *Table showing calculated fracture strength for four-point bend test*

	Float Glass			Laminated Glass		
	Small	Medium	Large	Small	Medium	Large
σ_{fmin}(MPa)	37.9	36.6	27.1	41.3	33.6	28.00
σ_{fmax}(MPa)	57.5	48.5	38.8	56.2	54.3	44.3
σ_{fmean}(MPa)	**48.3**	**42.9**	**34.1**	**49.0**	**45.3**	**38.1**
95% CI Lower(MPa)	46.3	41.0	32.4	47.4	43.3	36.1
95% CI Upper(MPa)	50.3	44.7	35.8	50.5	47.3	40.1

Note: σ_{fmin} = Minimum fracture strength, σ_{fmax} = Maximum fracture strength, σ_{fmean} = Average fracture strength, 95% CI = Confidence Interval.

A negative correlation was observed between fracture strength and specimen size: as the specimen size increased, the fracture strength decreased. For instance, the average fracture strength of the 150 mm long FG specimens (small loading span) is approximately 12.6% higher than that of the 300 mm long FG specimens (medium loading span). The 550 mm long FG specimens (large loading span) show a mean fracture strength that is 20.5% lower than that of the 300 mm long FG specimens. According to Osnes et al. [7, 80], the reduction in fracture strength as the specimen size increased can be attributed to the higher number of micro-flaws that may be present in large glass specimens, which can trigger early failure and result in reduced fracture strength. This highlights the inherent sensitivity of glass strength to micro-flaws. Additionally, the graphs reveal considerable variation in fracture strength across different specimen sizes. The variation is expected in brittle materials like glass due to the non-uniform nature of glass properties, which is influenced by various surface and edge micro-flaws (cracks).

5.1.2 Fracture Strength of LG subjected to FPBT

The forces measured at the initial failure point of the force-displacement graphs of the LG subjected to FPBT (Figure 4.2) were used to calculate the highest stress that the specimens can withstand. The first peak load was used because, at the point of initial fracture, the specimens were considered to have lost their structural integrity. Also, due to the composite nature of LG, with a large difference in stiffness between the outer glass layers and the polymer interlayer, the fracture strength of LG is more accurately represented using the stress-effective thickness (h_{eff}) instead of the normal thickness (h) in Equation 2.7. The modification led to a revised formula for calculating the fracture strength of LG under the FPBT, as shown in Equation E.7. This adjustment also accounted for the reduced neutral axis (y) and the moment of inertia (I) of the cross-section for the LG specimen after the initial fracture, as discussed in Section 4.1.2. Further explanations and complete details of the modified equation used for the fracture strength calculation of the laminated glass are provided in the Appendix E.

Figure 5.2 presents the collection of fracture strength values for all LG specimens subjected to the FPBT. The corresponding minimum, maximum, and average fracture strengths for the small, medium, and large loading spans of LG, along with the respective lower and upper 95% confidence intervals, are listed in Table 5.1. The average values indicate a decrease in fracture strength as the specimen size increased, which supports the idea that larger glass specimens would normally have more micro-flaws. For the LG specimens in Table 5.1, the average fracture strength of the 150 mm long LG specimens surpasses that of the 300 mm long LG specimens by about 8.2%, while the 550 mm LG specimens show a mean fracture strength that is 15.9% lower than that of the 300 mm LG specimens. Additionally, there is noticeable variation in fracture strength values across different specimen sizes, as depicted in each figure.

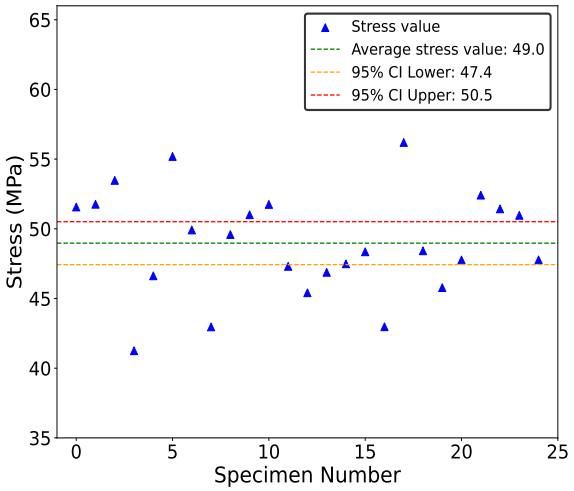

a. fracture strength of 150 mm long LG

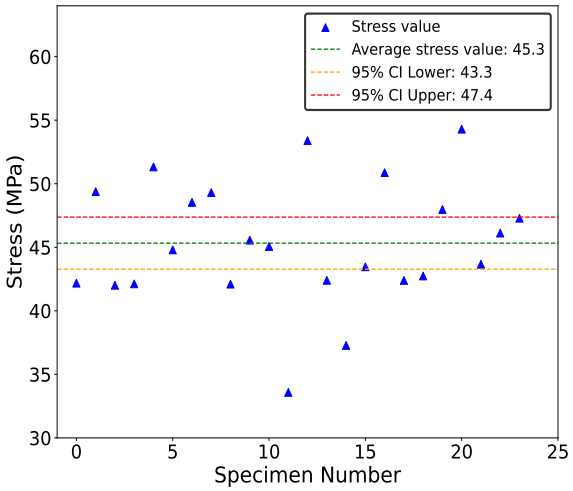

b. fracture strength of 300 mm long LG

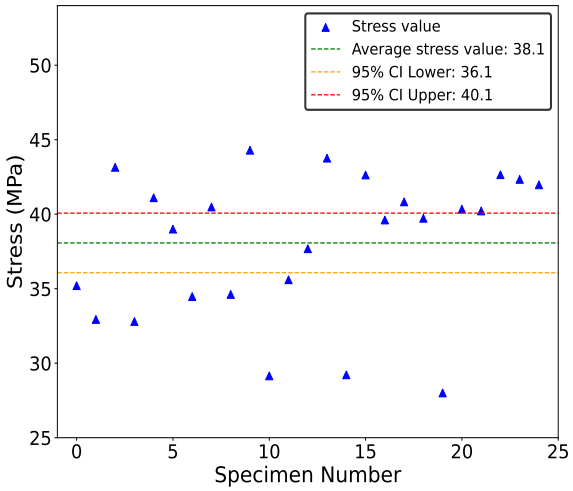

c. fracture strength of 550 mm long LG

Figure 5.2 Graphs of fracture strength of LG specimens subjected to the FPBT, as determined from the modified equation at first failure

5.1.3 Fracture Strength of FG subjected to ROR Test

Figure 5.3 presents the calculated fracture strengths for all FG specimens tested using the small (75 mm diameter), medium (105 mm diameter), and large (150 mm diameter) loading rings in the ROR test, as determined by Equation 2.16. The fracture strengths were calculated using the fracture force obtained from the force-displacement curves, along with the diameters of the loading and support rings, the diameter and thickness of the specimens (as shown in Table 3.6), and a Poisson's ratio of 0.23. The minimum, maximum, and average fracture strengths, along with the 95% confidence intervals for the FG specimens tested with small, medium, and large loading rings, are provided in Table 5.2. The fracture loads and strengths calculated for all the specimens subjected to the ROR test are presented in Table D.3 and Table D.4. Similar to the glass specimens

subjected to the FPBT, there is a negative correlation between fracture strength and the size of the loading ring: as the size of the loading ring increased, the fracture strength decreased. From Table 5.2, the average fracture strength of FG specimens subjected to the 75 mm diameter loading ring (small loading ring) exceeds that of FG specimens under the 105 mm diameter loading ring (medium loading ring) by approximately 5.7%. The FG specimens under the 150 mm diameter loading ring (large loading ring) show an average fracture strength that is 17.04% lower than that of the FG specimens under the medium loading ring. Also, the graphs show some scatter in the fracture strength values.

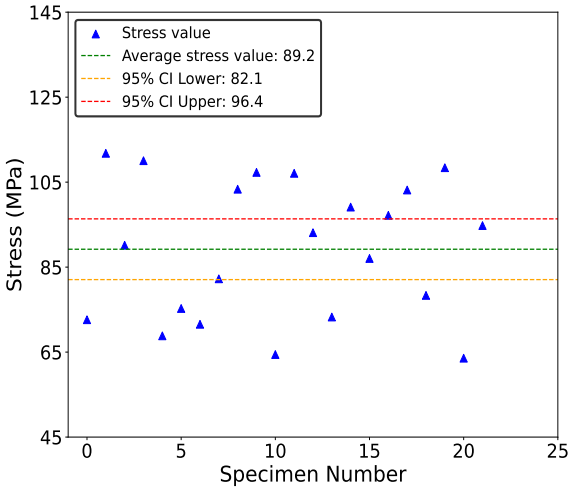

a. 75 mm diameter loading ring

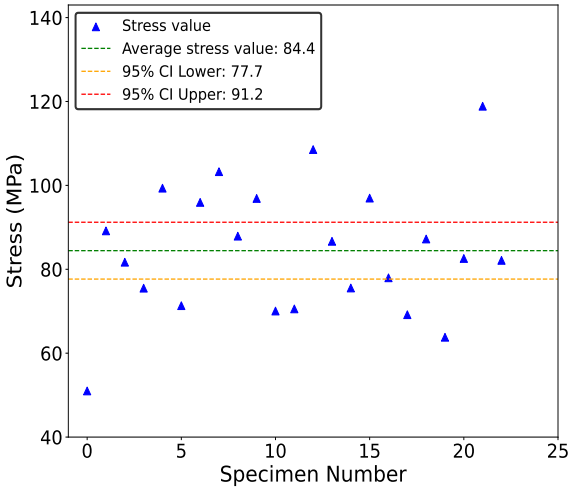

b. 105 mm diameter loading ring

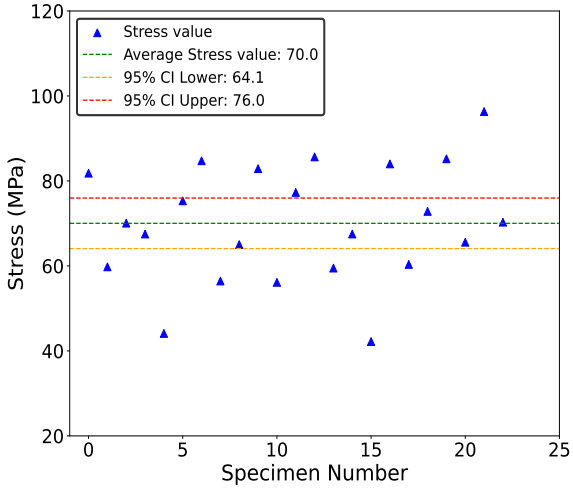

c. 150 mm diameter loading ring

Figure 5.3 Graphs of fracture strength of FG specimens subjected to the ROR testing

Table 5.2 *Table showing calculated fracture strength for ring-on-ring test*

	Float Glass			Laminated Glass		
	Small	Medium	Large	Small	Medium	Large
$\sigma_{f_{\min}}$(MPa)	63.6	51.0	42.2	27.7	21.3	12.4
$\sigma_{f_{\max}}$(MPa)	111.8	118.9	96.3	45.1	42.6	38.3
$\sigma_{f_{\text{mean}}}$(MPa)	**89.2**	**84.4**	**70.0**	**36.0**	**30.7**	**25.9**
95% CI Lower (MPa)	82.1	77.7	61.1	34.1	28.8	23.7
95% CI Upper (MPa)	96.4	91.2	76.0	39.3	33.7	29.1

5.1.4 Fracture Strength of LG subjected to ROR Test

Similar to the fracture strength of LG subjected to FPBT (Section 5.1.2), the stress-effective thickness (h_{eff}) of the LG expressed as Equation E.5 is used to replace the specimen thickness (h) in Equation 2.16 to give Equation E.8, which is used for the calculation of the fracture strength of the LG subjected to ROR test. The details of this can be seen in Appendix E.

Figures 5.4a, 5.4b, and 5.4c display the fracture strength of LG specimens subjected to small, medium, and large loading rings in the ROR test, respectively. Table 5.2 lists the minimum, maximum and average fracture strength along with the 95% confidence interval. Similar to the other glass specimens tested, the fracture strength decreased as the size of the loading ring increased. For LG specimens in Table 5.2, the average fracture strength of those under the small loading ring is approximately 17.3% higher than that of LG specimens under the medium loading ring, while LG specimens under the large loading ring show a mean fracture strength that is 15.6% lower than the average fracture strength of LG specimens under the medium loading ring. A noticeable variation in fracture strength is also observed.

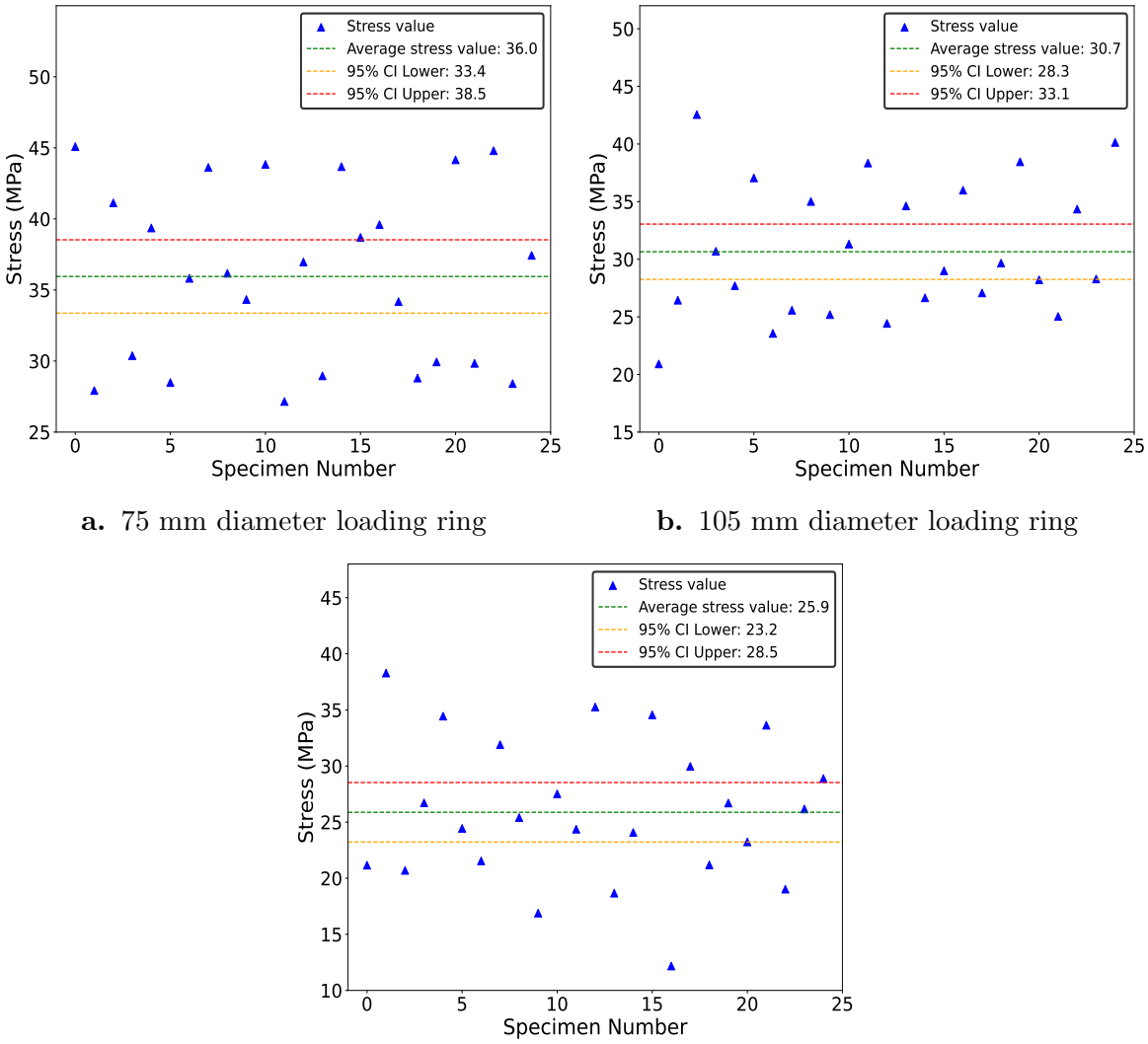

a. 75 mm diameter loading ring

b. 105 mm diameter loading ring

c. 150 mm diameter loading ring

Figure 5.4 Graphs of fracture strength of each LG specimen under the ROR testing, as determined from the modified equation at first failure

5.2 Comparison of the FPBT and the ROR Test

The FPBT and the ROR test are similar because both methods generate uniform maximum bending stresses in the central region of the glass specimen. Additionally, in both tests, maximum compressive stress occurs at the top surface, where the material is being compressed by the bending moment, while maximum tensile stress occurs at the bottom surface, where the material is stretched by the bending moment. Therefore, this allows for a direct comparison of stress behaviour in these regions, which is crucial for analysing failure characteristics. However, the magnitude of fracture strength and the variation obtained from each method differ because of the geometry and boundary conditions.

Figure 5.5 shows an overview of the fracture strength for the FPBT and the ROR test. The fracture strength for the FG specimens in the ROR test is higher than that of the FG specimens in the FPBT. This strongly supports the notion that the use of the ROR test can minimise edge effects, as edge flaws reduce fracture strength in the FPBT, as reported by De Pauw in [105]. The variation in fracture strength is lower in the FPBT.

In the loading span, micro-flaws at the specimen edges, which are created during the cutting process, are subjected to the highest stress. This leads to consistently early fractures, resulting in lower fracture strength values and reduced variation in the results. Thus, the fracture strength obtained from the FPBT is influenced by the condition of the specimen edges. In contrast, the specimen in the ROR test experiences the highest tensile stress beneath the loading ring on the opposite surface of the glass. The region is located away from the specimen edges, where various micro-cracks may have been introduced during the cutting process. The presence or absence of surface flaws in the loading region affects the measured fracture strength, resulting in increased variation in the results. The impact of the cutting process in creating more micro-flaws along the edges of glass specimens was highlighted by Lindqvist [4].

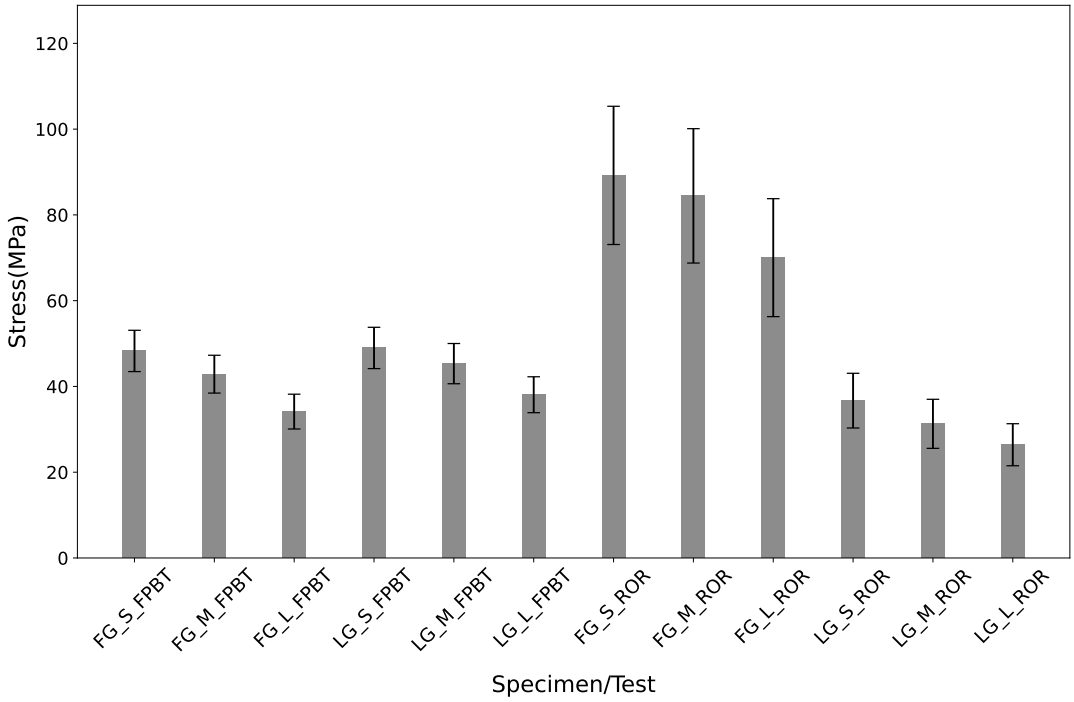

Figure 5.5 Overview of the FPBT and the ROR test: fracture strength.

Note: FG_S, FG_M, and FG_L refer to float glass specimens subjected to small, medium, and large loading spans, respectively. Similarly, LG_S, LG_M, and LG_L represent laminated glass specimens under small, medium, and large loading spans, respectively.

The fracture strength of the LG in the ROR test is slightly lower than that of the LG in the FPBT. This could be explained by cracks of any orientation resulting in failure in

ROR tests since the stress is equibiaxial. In FPBT, the normal stress is uniaxial, and only cracks perpendicular to this stress are likely to cause failure [2]. In addition, in the ROR test, surface flaws under tension initiate failure, and since the surface area under tension doubles for LG, as seen in Figure 5.6b and 5.6d, it results in a much lower strength. The similar stress observed in LG samples compared to FG samples in the FPBT is due to the edge area under tension remaining comparable in both cases, as shown in Figure 5.6a and 5.6c.

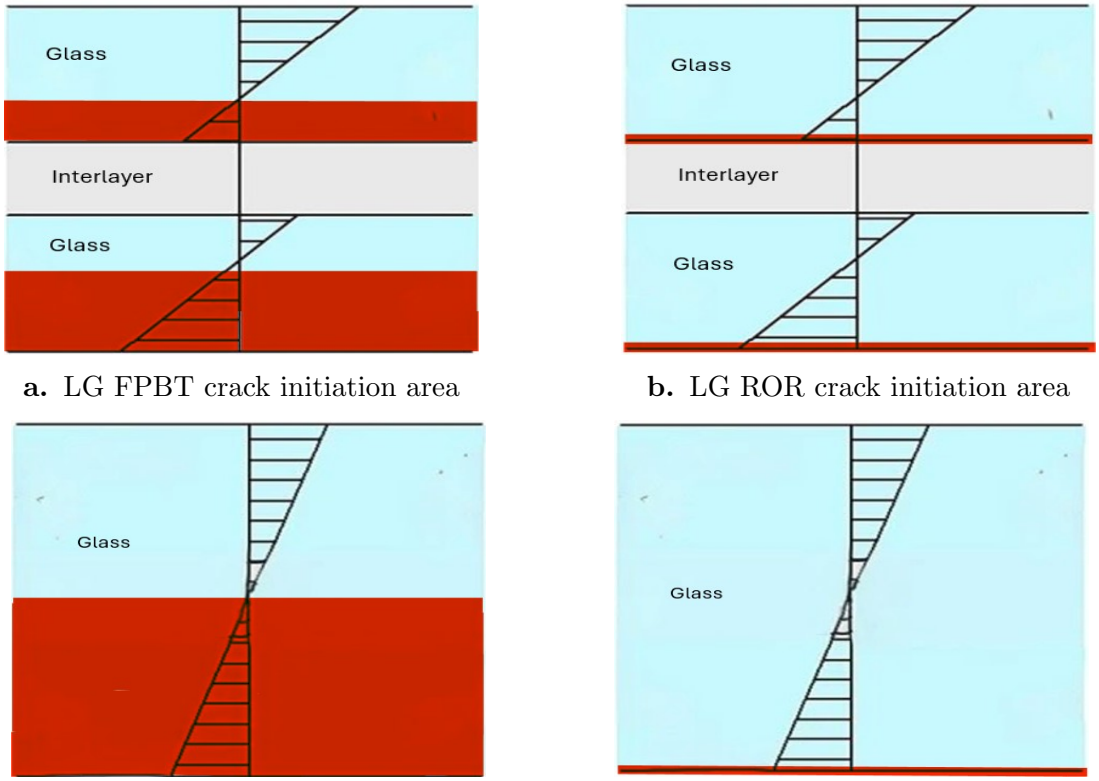

a. LG FPBT crack initiation area

b. LG ROR crack initiation area

c. FG FPBT crack initiation area

d. FG ROR crack initiation area

Figure 5.6 Crack initiation area for Specimen subjected to the FPBT and the ROR test.

During the FPBT and the ROR test of FG specimens, a fracture with a loud noise was heard. This can be attributed to the rapid crack propagation in the glass material, causing the fracture to be observed almost instantaneously across its entire cross-section. The brittle nature of the glass prevented plastic deformation at the crack tip and the redistribution of load, resulting in sudden and catastrophic failure. The transparent adhesive material affixed to the compressive side of the FG specimens effectively captured the glass fragments upon fracture, preventing them from becoming projectiles. In contrast, during the FPBT and the ROR test of LG, only a small crack noise was heard. The sound can be attributed to the presence of an interlayer within the LG, which distributes stress and slows down crack propagation across the glass layers, thereby reducing the loud

noise compared to FG. Additionally, the interlayer holds together broken glass fragments, preventing potential injuries.

5.3 Stress and Moment Relation

As can be seen from Equations 2.7 and Equation 2.12, there is a linear relationship between the moment and the stress. This linear relationship is influenced by the square of the thickness of the plate, h, which appears in the denominator of the governing equations. For FPBT in Figure 5.7a, the LG curve has a steeper gradient compared to the FG. This is because the effective thickness of the LG is 4.86 mm, which is lower than the 6 mm thickness of the FG. Since stress is inversely proportional to h^2.

Even though the laminated glass is physically thicker, it behaves as if it is thinner, and for a given bending moment, the stress is slightly higher for LG relative to FG in the FPBT. The situation is different for the ROR test. The effective thickness of LG is 6.18 mm which approximately similar to the thickness of FG. The slopes of the curves are then similar for LG and FG as can be observed in Figure 5.7b.

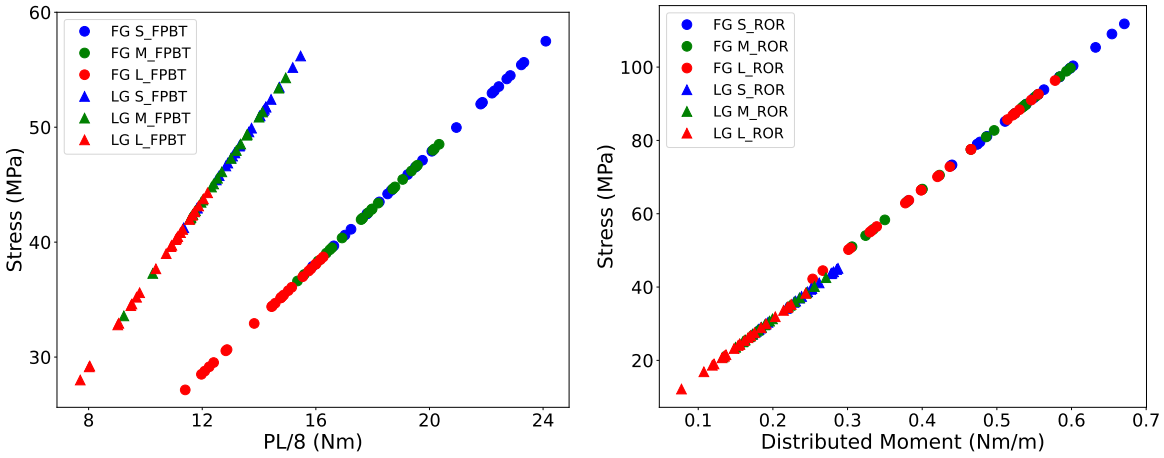

a. Glass specimens subjected to the FPBT **b.** Glass specimens subjected to the ROR

Figure 5.7 Graphs of stress vs moment

Note: The stress–moment curves do not pass through the origin $(0, 0)$, which suggests that there may be a small amount of stress present even before the main loading phase begins. This could be due to pre-existing residual stresses in the glass, imperfect contact between the loading fixtures and the specimen, or a small preload applied to ensure proper seating. These factors can introduce an initial stress offset that shifts the entire curve upward.

5.4 Critical Flaw Size

The fracture toughness equations, as discussed in Section 2.11 and represented by Equation 2.17 for uniaxial loading and Equation 2.19 for biaxial loading, were used to calculate the critical flaw size for each tested specimen. For the FPBT, a geometry factor of 0.713, reported by Porter [112], was adopted and a fracture toughness value (K_{IC}) of 0.75 MPa $\sqrt{m}$ for soda-lime glass was used [2].

Figure 5.8 shows a direct relationship between flaw size and loading span: as the loading span increased, the flaw size increased in both the FPBT and ROR tests. The observation echoes the work of Osnes et al. [7, 80], where it was noted that increased loading spans or specimen sizes correspond to a higher probability of encountering micro-flaws.

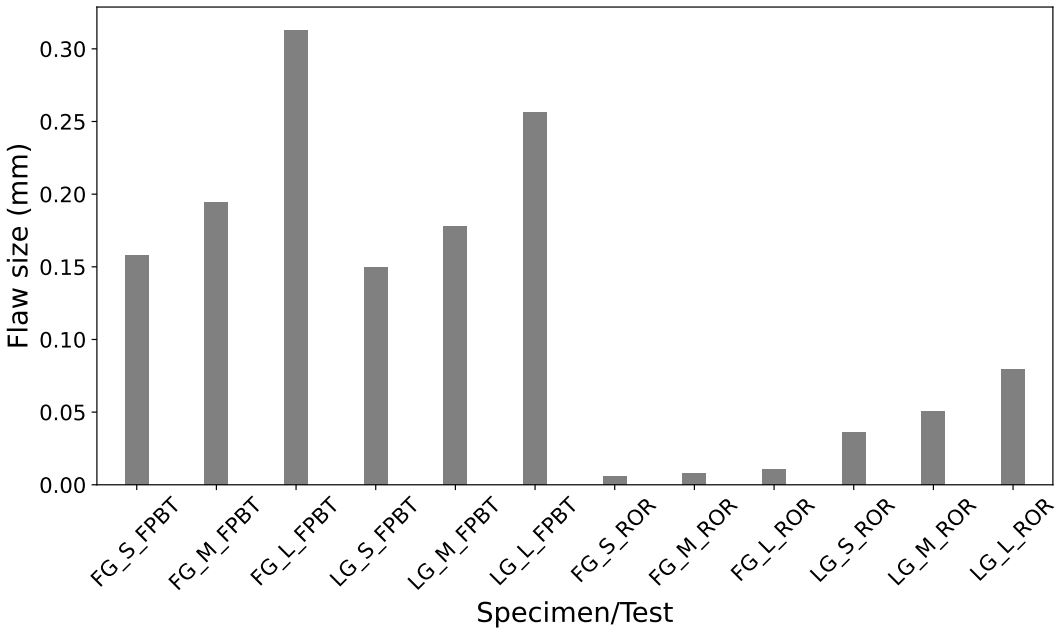

Figure 5.8 Critical micro-flaw size

It is observed that FPBT specimens exhibit larger flaw sizes across all loading spans compared to the equivalent ROR spans. The difference is likely due to the higher likelihood of locating micro-flaws, particularly at the edges, in the FPBT specimens.

5.5 Weibull Analysis of Glass Strength

The relationship between fracture strength and fracture probability for FG and LG specimens subjected to the FPBT and the ROR test is analysed with the Weibull distribution and plotted in Figure 5.9. Each graph contains three linear regression lines of glass specimens tested. The abscissa represents the natural logarithm of fracture strength, $ln(\sigma)$, while the ordinate represents the natural logarithm of fracture probability

function, $\ln(\ln\left(\frac{1}{1-F}\right))$, where F represents the fracture probability (See Section 3.6 for details about the graph plotting).

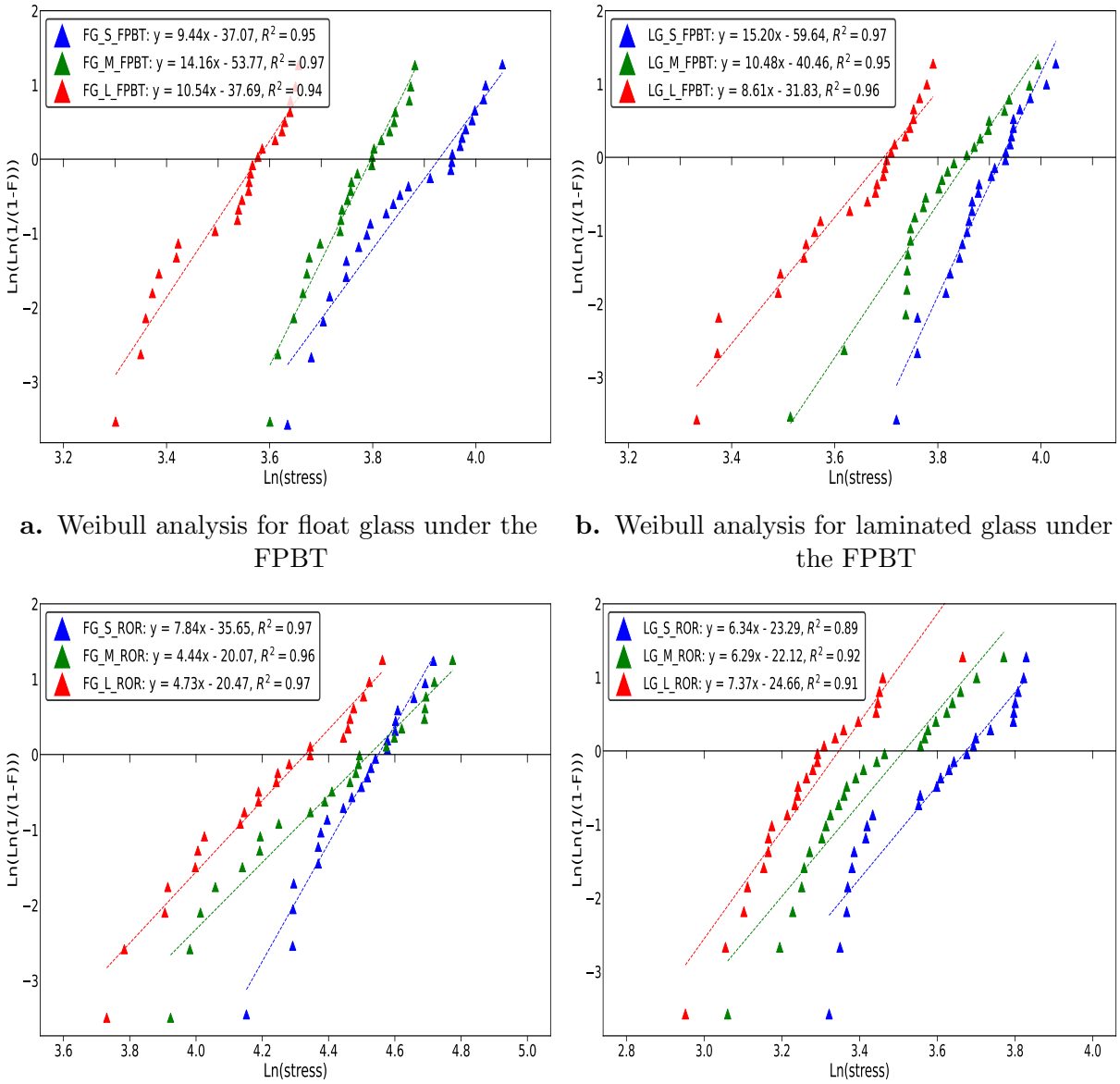

a. Weibull analysis for float glass under the FPBT

b. Weibull analysis for laminated glass under the FPBT

c. Weibull analysis for float glass under ROR testing

d. Weibull analysis for laminated glass under ROR testing

Figure 5.9 Graphs of Weibull distribution analysis

All the graphs in Figure 5.9 display high coefficients of determination, R^2, (as it is relatively closer to 1). The high R^2 values suggest a strong linear correlation between the natural logarithms of the fracture probability function and the fracture strengths of the specimens. The consistency of high R^2 values across all specimens, tested under the three different loading spans in both the FPBT and ROR tests, supports the suitability of the Weibull distribution model for describing the fracture strength of glass materials under stress. Also,

in all the graphs in Figure 5.9, the slopes of the regression lines for FG and LG specimens subjected to various loading spans of the FPBT and ROR tests, which represent the shape parameter of the Weibull distribution (β), vary. The different slopes indicate that the rate of glass fracture varies across the different loading spans. However, the absence of a specific trend in the slopes could be due to the limited number of specimens tested, as Kinsella and Persson [124] highlighted that small sample sizes can lead to significant scattering in the estimation of Weibull distribution parameters, potentially resulting in misleading interpretations or statistical artefacts.

5.6 FEA of Glass

Table 5.3 compares the average simulation stresses of FG and LG under the three various loading conditions of four-point loading and ring-on-ring loading with the average fracture strength values of the glass specimens obtained from the calculated (listed in Table 5.1 and Table 5.2). The comparison reveals no significant difference between the two, thereby validating the fracture strength of glass specimens obtained based on the calculated approach, especially the values obtained for LG specimens using the effective thickness analytical approach.

Table 5.3 *Comparison of FEA and calculated fracture strength for FPBT and ROR*

Test	Loading span	Float Glass		Laminated Glass	
		FEA (MPa)	Calculated (MPa)	FEA (MPa)	Calculated (MPa)
Four-point Bend	Small	48.9	48.3	49.2	49.0
	Medium	43.1	42.9	45.2	45.3
	Large	34.8	34.1	38.0	38.1
Ring on Ring	Small	89.07	89.2	36.6	36.0
	Medium	84.9	84.4	31.4	30.7
	Large	70.5	70.0	26.2	25.9

Chapter 6

Conclusions

The investigation of the fracture strength of float glass (FG) and laminated glass (LG) using the four-point bend test (FPBT) and ring-on-ring (ROR) test reveals the complex nature of glass strength. The bending experimental tests conducted provide insights into the fracture strength of FG and LG specimens in relation to the various loading spans. Based on the experiments conducted and the results, the following conclusions can be made:

- During the glass surface identification test, the use of the ultraviolet light method through the tin-side detector device proved to be highly effective in precisely identifying the tin-side of the FG and LG.
- From the study, all the glass specimens tested exhibit elastic behaviour with no plastic deformation and fail through the brittle fracture. The energy absorption during crack propagation is significantly limited, especially when compared to materials like metals. This highlights the inherent fragility of glass, which emphasises the significance of considering its brittle nature in various applications and design considerations.
- The FPBT fracture pattern analysis for both FG and LG revealed consistent fracture patterns within loading spans, with edge fracture initiation accounting for about 80% of the specimens. In contrast, during the ROR test, no fractures were found to initiate at the specimen edge of the ROR specimens; all fractures were contained within the loading ring region.
- In all the LG specimens tested, the fragments adhered to the interlayer, preventing the broken glass from becoming projectiles. Similarly, the adhesive material affixed to the compression surface of all the FG specimens served to keep the fragments from becoming projectiles.
- In both the FPBT and ROR test, it is observed that the fracture strength values obtained with the smaller loading spans consistently surpassed those obtained with larger loading spans across all tested glass specimens. The trend indicates that the size of the loading span has a substantial influence on the fracture strength of both FG and LG specimens subjected to the FPBT and ROR test.

- Despite the controlled experimental conditions, the fracture strength values presented in the study exhibit considerable variability, which is usually due to the probability of varying numbers of micro-flaws across different loading spans.
- The experimental data from all glass specimens subjected to various loading spans of the FPBT and the ROR tests demonstrated excellent compliance with the Weibull distribution model. The high values of coefficients of determination, R^2, indicate that the Weibull distribution is suitable for describing the fracture strength of glass.
- The fracture toughness equation was employed to evaluate the critical flaw size values in the glass specimens. The results indicate a positive relationship between flaw size and loading span. Specifically, the small loading span exhibits the smallest magnitude of flaw size values for all glass specimens in both the FPBT and ROR test.
- The comparison of fracture strength obtained from finite element analysis with those obtained from the analytical approach showed no significant difference, validating the experimental and analytical methods employed in the study.

In summary, the study provides important insights into the fracture strength of float glass and laminated glass subjected to various loading conditions. The knowledge is crucial for FG and LG applications in the construction and automotive industries, among others, where safety and durability are of utmost importance.

Chapter 7

Recommendations

From the experiments conducted in the study, the following suggestions are recommended for future studies:

1. In all the glass specimens tested, the glass was positioned with the air-side face downward. Future research could consider testing the glass specimens with the tin-side facing downward.
2. The study only considered float and laminated glass. Future studies should investigate other types of glass, such as heat-treated glass.
3. All the experiments were performed at room temperature. Future research could determine the strength of glass at both reduced and elevated temperatures.
4. The study mainly considered quasi-static experiments with a relatively low loading rate. Future experiments could explore the impacts of dynamic loading rate.
5. No specific trends were observed in the magnitude of the Weibull parameter values for float and laminated glass in both the FPBT and ROR tests, likely due to the limited number of specimens tested. Future studies should consider a larger number of specimens to provide a more definitive trend of the Weibull parameter values.

References

[1] M. Haldimann, A. Luible, and M. Overend, *Structural use of glass*. International Association for Bridge and Structural Engineering, 2008, vol. 10.

[2] M. Haldimann, "Fracture strength of structural glass elements: analytical and numerical modelling, testing and design," Ph.D. thesis, EPFL, 2006.

[3] G. Pisano, "The statistical characterization of glass strength: from the micro-to the macro-mechanical response," Ph.D. thesis, Università di Parma. Dipartimento di Ingegneria e Architettura, 2018.

[4] M. Lindqvist, "Structural glass strength prediction based on edge flaw characterization," Ph.D. thesis, Ecole Polytechnique Fédérale de Lausanne, 2013.

[5] C. Fors, "Mechanical properties of interlayers in laminated glass-experimental and numerical evaluation," Master thesis, Lund University, Sweden., 2014.

[6] I. Nurhuda, *Ultimate behaviour of annealed glass panels subject to out-of-plane static and transient action*. University of Melbourne, Department of Infrastructure Engineering, 2011.

[7] K. Osnes, T. Børvik, and S.Hopperstad, "Testing and modelling of annealed float glass under quasi-static and dynamic loading," *Engineering Fracture Mechanics*, vol. 201, pp. 107–129, 2018.

[8] J. Belis, C. Louter, J. H. Nielsen, and J. Schneider, "Architectural glass," in *Springer handbook of glass*. Springer, 2019, pp. 1781–1819.

[9] W. Xiufeng, L. Longfei, Z. Ding, and J. Peng, "Weibull model for bending failure prediction of polyurea laminated glass under coaxial double-ring test," *Engineering Fracture Mechanics*, p. 109, 2024.

[10] S. Van Dam, "Experimental analysis of the post-fracture response of laminated glass under impact and blast loading," Ph.D. thesis, Ghent University, 2017.

[11] S. Basu and D. Sarkar, "Glass processing and properties," in *Ceramic Processing*. CRC Press, 2019, pp. 247–281.

[12] C. Delincé, "Post-breakage behaviour of laminated glass in structural applications," in *Conference on Architectural and Structural Applications of Glass*. IOS Press, 2008, pp. 459–467.

[13] Thomas, "Laminated glass versus tempered glass," Accessed: 2 March 2023. [Online]. Available: https://ukcarglass.co.uk/blog/laminated-car-glass-versus-tem

pered-car-glass

[14] A. Vedrtnam and S. Pawar, "Laminated glass: Classification, characterization, and future perspectives," *J. Mater. Educ*, vol. 42, pp. 51–61, 2020.

[15] J. Chung, "World's longest glass bridge opens in china's three gorges scenic area," accessed: 15 August 2023. [Online]. Available: https://www.techeblog.com/worlds-longest-glass-bridge-china/

[16] A. Hussain, "Osha safety glasses requirements you should know," Accessed: 2, August 2022. [Online]. Available: https://www.hseblog.com/osha-safety-glasses-requirements/

[17] D. Callewaert, "Stiffness of glass/ionomer laminates in structural applications," Ph.D. thesis, Ghent University, 2011.

[18] R. T. Nichols and R. M. Sowers, "Laminated materials, glass," *Kirk-Othmer Encyclopedia of Chemical Technology*, 2000.

[19] P. Foraboschi, "Analytical model for laminated-glass plate," *Composites Part B: Engineering*, vol. 43, no. 5, pp. 2094–2106, 2012.

[20] R. A. Behr, A. Belarbi, and A. T. Brown, "Seismic performance of architectural glass in a storefront wall system," *Earthquake Spectra*, vol. 11, no. 3, pp. 367–391, 1995.

[21] M. Martín, X. Centelles, A. Solé, C. Barreneche, A. I. Fernández, and L. F. Cabeza, "Polymeric interlayer materials for laminated glass: A review," *Construction and Building Materials*, vol. 230, p. 116897, 2020.

[22] H. Sanders and S. Electrochromics, "Fading protection and sageglass® products," 2014.

[23] M. Müller, S. Reich, C. Pfütze, and I. Stelzer, "Investigation of color protection of laminated glass by uv-blocking interlayers for conservation application," *Glass Structures & Engineering*, pp. 1–26, 2024.

[24] M. Teotia and R. Soni, "Applications of finite element modelling in failure analysis of laminated glass composites: A review," *Engineering Failure Analysis*, vol. 94, pp. 412–437, 2018.

[25] R. Behr, J. E. Minor, and H. Norville, "Structural behavior of architectural laminated glass," *Journal of Structural Engineering*, vol. 119, no. 1, pp. 202–222, 1993.

[26] Z. Wang, D. Ma, T. Suo, Y. Li, and A. Manes, "Investigation into different numerical methods in predicting the response of aluminosilicate glass under quasi-static and impact loading conditions," *International Journal of Mechanical Sciences*, vol. 196, p. 106286, 2021.

[27] K. Osnes, O. S. Hopperstad, and T. Børvik, "Rate dependent fracture of monolithic and laminated glass: Experiments and simulations," *Engineering Structures*, vol. 212, p. 110516, 2020.

[28] S. Akter and M. Khani, "Characterisation of laminated glass for structural applications," 2013.

[29] I. M. Kalogeras and H. E. Hagg Lobland, "The nature of the glassy state: structure and glass transitions," *Journal of Materials Education*, vol. 34, no. 3, p. 69, 2012.

[30] A. Popov, "Atomic structure and structural modification of glass," in *Semiconductors and Semimetals*. Elsevier, 2004, vol. 78, pp. 51–95.

[31] C. Louter, M. Akilo, B. Miri, T. Neeskens, R. R. Silveira, Ö. Topcu, I. van der Weijde, C. Zha, M. Bilow, M. Turrin *et al.*, "Adaptive and composite thin glass concepts for architectural applications," *Heron*, vol. 63, no. 1/2, pp. 199–218, 2018.

[32] M. Biron, "Detailed accounts of thermoset resins for moulding and composite matrices," *Thermosets and Composites*, pp. 183–327, 2004.

[33] A. K. Varshneya, "Chemical strengthening of glass: lessons learned and yet to be learned," *International Journal of Applied Glass Science*, vol. 1, no. 2, pp. 131–142, 2010.

[34] M. Fröling, "Strength design methods for laminated glass," Ph.D. thesis, epartment of Construction Sciences, at Lund Universit, 2011.

[35] C. Gautam, A. K. Yadav, and A. K. Singh, "A review on infrared spectroscopy of borate glasses with effects of different additives," *International Scholarly Research Notices*, vol. 2012, no. 1, p. 428497, 2012.

[36] S. Rasmussen, *How glass changed the world: The history and chemistry of glass from antiquity to the 13th century*. Springer Science and Business Media, 2012.

[37] J. Henderson, *Ancient glass: an interdisciplinary exploration*. Cambridge University Press, 2016.

[38] S. G. Evans, "The odyssey of obsidian: A re-evaluation of chipped stone in the late bronze age aegean," Ph.D. thesis, University of Victoria, 2023.

[39] S. Dillis, "Antimony as a raw material for making metal and vitreous materials from the bronze age to the roman period," Ph.D. thesis, Dissertation for Doctoral Degree. Leuven: KU Leuven, 2020.

[40] B. Lambert and B. Santiago, "The history and structure of stantienite," *Bulletin for the History of Chemistry*, 2015.

[41] S. C. Rasmussen, "A brief history of early silica glass: Impact on science and society," *Substantia*, pp. 125–138, 2019.

[42] H. Bach and D. Krause, *Analysis of the composition and structure of glass and glass ceramics*. Springer Science & Business Media, 2013.

[43] EN 572-1:2012, "Glass in building - basic soda-lime silicate glass products - part 1: Definitions and general physical and mechanical properties," European Standard, Tech. Rep., 2012.

[44] L. Cormier, "Glasses: aluminosilicates," *Encyclopedia of materials: Technical Ceramics and glasses*, pp. 496–518, 2021.

[45] M. Qureshi and K. Varshney, *Inorganic ion exchangers in chemical analysis*. CRC press Florida, 1991, vol. 21.

[46] B. Elvers, *Ullmann's Encyclopedia of Industrial Chemistry*. Verlag Chemie Hoboken, NJ, 1991, vol. 17.

[47] S. Gobain, "Glass manufacturing process," Accessed: 2, August 2022. [Online]. Available: https://in.saint-gobain-glass.com/knowledge-center/glass-manufacturing-process

[48] M. Bustillo Revuelta, *Glass*. Cham: Springer International Publishing, 2021, pp. 375–400. [Online]. Available: https://doi.org/10.1007/978-3-030-65207-4_13

[49] J. Souviron and A. Z. Khan, "The materiality of transparency: An environmental analysis of the architectural flat glass industry since 1945 in europe, france and belgium," *Resources, Conservation and Recycling*, vol. 174, p. 105779, 2021.

[50] K. Pilkington, "Pilkington float process." Accessed: 2, August 2022. [Online]. Available: https://www.pilkington.com/en/global/knowledge-base/glass-technology/sir-alastair-pilkington

[51] F. Pölzl, "Mechanical behavior of cold-bent insulating glass units," Ph.D. thesis, Graz University of Technology, 2017.

[52] H. R. Sujon, "Float glass production process," accessed: 15 July 2023. [Online]. Available: https://www.slideshare.net/slideshow/glass-industry-visit-osmaniya-glass-sheet-factory-ltdbangladesh/105719452

[53] A. van de Lavoir, "Check for the tin side of window glass (float glass) with a drop of water," accessed: 15 July 2023. [Online]. Available: https://peliglass.eu/2013/11/05/check-for-the-tin-side-of-window-glass-float-glass-with-a-drop-of-water/

[54] Garibaldi Glass, "Air side vs. tin side of glass: What's the difference?" accessed: 15 July 2023. [Online]. Available: https://www.garibaldiglass.com/air-side-tin-side/

[55] A. S. Güzel, M. Sarıgüzel, M. C. Özdemir Yanık, E. Günay, M. Usta, and Y. Öztürk, "Enhancing mechanical endurance of chemical-tempered thin soda-lime silicate float glass by ion exchange," *Journal of the Australian Ceramic Society*, vol. 56, no. 1, pp. 185–201, 2020.

[56] M. H. Krohn, *Effect of tin on the relationship between composition, structure, and properties of soda-lime-silicate glasses*. The Pennsylvania State University, 2004.

[57] M. Krohn and J. Hellmann, "Test methodology for strength testing of soda-lime-silica float glass before and after enameling," *Journal of testing and evaluation*, vol. 30, no. 6, pp. 470–477, 2002.

[58] M. Teotia and R. Soni, "Improvement in impact properties of laminated glass panels through surface treatment and silane coupling agent," *J Indian Chem Soc*, vol. 93, no. 6, pp. 639–648, 2016.

[59] R. B. Ali, M. M. Islam, and M. Billah, "Sophisticated developments and advanced applications of glass structure: summary of recent research," *World Scientific News*, vol. 124, no. 1, pp. 1–85, 2019.

[60] M. Teotia and K. Soni, "Polymer interlayers for glass lamination—a review," *Int. J. Sci. Res.(IJSR)*, vol. 3, pp. 1264–1270, 2014.

[61] R. Ledbetter, R. Walker, and P. Keiller, "Structural use of glass," *Journal of architectural engineering*, vol. 12, no. 3, pp. 137–149, 2006.

[62] C. Bedon, X. Zhang, F. Santos, D. Honfi, M. Kozłowski, M. Arrigoni, L. Figuli, and D. Lange, "Performance of structural glass facades under extreme loads–design methods, existing research, current issues and trends," *Construction and Building Materials*, vol. 163, pp. 921–937, 2018.

[63] H. Carré and L. Daudeville, "Load-bearing capacity of tempered structural glass," *Journal of Engineering Mechanics*, vol. 125, no. 8, pp. 914–921, 1999.

[64] H. Zhu and S. Khanna, "Dynamic response of a novel laminated glass panel using a transparent glass fiber-reinforced composite interlayer under blast loading," *International Journal of Impact Engineering*, vol. 89, pp. 14–24, 2016.

[65] ASTM C1036–06, "Standard specification for flat glass," American Society For Testing And Materials, Tech. Rep., 2006.

[66] EN 572-2:2012, "Glass in building - basic soda lime silicate glass products - part 2: Float glass," European Standard, Tech. Rep., 2012.

[67] R. Bejkollari, "Evaluation of the effects of residual surface compression on the strength of structural glass bolted connections," Ph.D. thesis, Texas A&M University, 2018.

[68] EN 1863-1, "Glass in building. heat-strengthened soda lime silicate glass. definition and description. brussels: European committee for standardization (CEN)," European Standard, Tech. Rep., 2012.

[69] ASTM C1048-18, "Standard specification for heat-strengthened and fully tempered flat glass," American Society For Testing And Materials, Tech. Rep., 2018.

[70] S. Bornemann, S. Henning, K. Naumenko, M. Pander, N. Thavayogarajah, and M. Würkner, "Strength analysis of laminated glass/eva interfaces: Microstructure, peel force and energy of adhesion," *Composite Structures*, vol. 297, p. 115940, 2022.

[71] A. J. Pye, *The structural performance of glass-adhesive T-beams*. University of Bath (United Kingdom), 1998.

[72] EN 12150-1: 2015, "Glass in building—thermally toughened soda lime silicate safety glass," 2000.

[73] X. Jiang, X. Lin, C. Li, M. Pang, L. Liu, Y. Yu, Z. Wang, Y. Luo, A. Lu, and Z. Bai, "Effect of potassium and silver ion-exchange on the strengthening effect and properties of aluminosilicate glass," *Ceramics International*, vol. 49, no. 19, pp. 31 351–31 363, 2023.

[74] G. Quinn, "A history of the fractography of glasses and ceramics," *Fractography of Glasses and Ceramics VI: Ceramic Transactions*, vol. 230, pp. 1–55, 2012.

[75] H. S. Norville and J. E. Minor, "Strength of weathered window glass," *American Ceramic Society Bulletin*, vol. 64, no. 11, pp. 1467–1470, 1985.

[76] G. Castori and E. Speranzini, "Fracture strength prediction of float glass: The coaxial double ring test method," *Construction and Building Materials*, vol. 225, pp. 1064–1076, 2019.

[77] D. Civil, "Tension vs compression," Accessed: 2 March 2023. [Online]. Available: ht tps://dailycivil.com/tension-vs-compression-what-is-tension-what-is-compression/

[78] I. Stelzer, "High performance laminated glass," in *Challenging Glass Conference Proceedings*, vol. 2, 2010, pp. 465–474.

[79] R. Ravimony, A. Joseph, and L. Mangal, "Investigations on the flexural performance of laminated glass," in *IOP Conference Series: Earth and Environmental Science*, vol. 491, no. 1. IOP Publishing, 2020, p. 012023.

[80] K. Osnes, O. S. Hopperstad, and T. Børvik, "Quasi-static and dynamic testing of annealed float glass," in *Proceedings*, vol. 2, no. 8. MDPI, 2018, p. 495.

[81] F. Sharafeddin, A. Alavi, and Z. Talei, "Flexural strength of glass and polyethylene fiber combined with three different composites," *Journal of Dentistry*, vol. 14, no. 1, p. 13, 2013.

[82] R. H. Snedeker, K. T. Garty, and F. J. Skiermont, "Glass-polycarbonate resin laminates," May 30 1972, uS Patent 3,666,614.

[83] C. Schimmelpenningh and J.Hoagland, "Safety glass structure resistant to extreme wind and impact," Dec. 29 1998, uS Patent 5,853,828.

[84] S. Bennison, M. Qin, and P. Davies, "High-performance laminated glass for

structurally efficient glazing," *Innovative light-weight structures and sustainable facades, Hong Kong*, pp. 1–12, 2008.

[85] S. A. Batzer, "Rollover collisions injuries related to automotive side glass," *Professional Safety*, vol. 52, no. 04, 2007.

[86] G. Castori and E. Speranzini, "Structural analysis of failure behavior of laminated glass," *Composites Part B: Engineering*, vol. 125, pp. 89–99, 2017.

[87] X. Zhang and M. Haibao, "Impact response of laminated glass with varying interlayer materials," *International Journal of Impact Engineering*, vol. 139, pp. 103–505, 2020.

[88] C. Louter, J. Belis, F. Bos, D. Callewaert, and F. Veer, "Experimental investigation of the temperature effect on the structural response of sg-laminated reinforced glass beams," *Engineering Structures*, vol. 32, no. 6, pp. 1590–1599, 2010.

[89] H. Schober and J. Schneider, "Developments in structural glass and glass structures," *Structural engineering international*, vol. 14, no. 2, pp. 84–87, 2004.

[90] M. Vandebroek, M. Lindqvist, J. Belis, and C. Louter, "Edge strength of cut and polished glass beams," in *12th International Conference on Architectural and Automotive Glass (Glass Performance Days 2011)*. Glass Performance Days, 2011, pp. 476–479.

[91] L. Biolzi and M. Orlando, "Static and dynamic response of progressively damaged ionoplast laminated glass beams," *Composite Structures*, vol. 157, pp. 337–347, 2016.

[92] G. Sedlacek, K. Blank, and J. Güsgen, "Glass in structural engineering," *Structural Engineer*, vol. 73, pp. 17–17, 1995.

[93] L. Galuppi, G. Manara, and C. Gianni, "Practical expressions for the design of laminated glass," *Composites Part B: Engineering*, vol. 45, no. 1, pp. 1677–1688, 2013.

[94] J. Hooper, "On the bending of architectural laminated glass," *International Journal of Mechanical Sciences*, vol. 15, no. 4, pp. 309–323, 1973.

[95] M. Timmel, S. Kolling, P. Osterrieder, and P. Du Bois, "A finite element model for impact simulation with laminated glass," *International Journal of Impact Engineering*, vol. 34, no. 8, pp. 1465–1478, 2007.

[96] R. Behr and J. Minor, "Laminated glass units under uniform lateral pressure," *Journal of Structural Engineering*, vol. 111, no. 5, pp. 1037–1050, 1985.

[97] P. Foraboschi, "Behavior and failure strength of laminated glass beams," *Journal of Engineering Mechanics*, vol. 133, no. 12, pp. 1290–1301, 2019.

[98] S. C. Angelides, J. P. Talbot, and M. Overend, "The effects of high strain-rate and in-plane restraint on quasi-statically loaded laminated glass: a theoretical study with

applications to blast enhancement," *Glass Structures & Engineering*, vol. 4, no. 3, pp. 403–420, 2019.

[99] G. Laura and G. Royer-Carfagni, "The post-breakage response of laminated heat-treated glass under in plane and out of plane loading," *Composites Part B: Engineering*, vol. 147, pp. 227–239, 2018.

[100] S. Feirabend and W. Sobek, "Reinforced laminated glass," in *Challenging Glass: Conference on Architectural and Structural Applications of Glass, Faculty of Architecture, Delft University of Technology*, 2008, pp. 469–478.

[101] M. Arora, "Indentation deformation/fracture of normal and anomalous glasses," *Journal of Non-Crystalline Solids*, vol. 31, no. 3, pp. 415–428, 1979.

[102] H. Y. Shin, C. Lawrence, K. R. Kota, P. Thamburaja, A. Srinivasa, T. E. Lacy Jr, and J. Reddy, "Experimental, theoretical and numerical studies on plain concrete fracture in the low-strain rate regime—a state-of-the-art review," *Mechanics of Advanced Materials and Structures*, vol. 29, no. 28, pp. 7115–7159, 2022.

[103] ASTM C158-02, "Standard test methods for strength of glass by flexure (determination of modulus of rupture)," in *American society for Testing Materials*, 2017.

[104] J. J. Swab, P. J. Patel, X. Tran, L. Gilde, E. Luoto, M. H. Gaviola, A. Gott, B. Paulson, and S. Kilczewski, "Equibiaxial flexure strength of glass: influence of glass plate size and equibiaxial ring ratio," *International Journal of Applied Glass Science*, vol. 5, no. 4, pp. 384–392, 2014.

[105] S. De Pauw, "Experimental and numerical study of impact on window glass fitted with safety window film," Ph.D. thesis, Ghent University, 2010.

[106] ASTM C1499-19, "Standard test method for monotonic equibiaxial flexural strength of advanced ceramics at ambient temperature," American Society For Testing And Materials, Tech. Rep., 2019.

[107] C. Pisano and R. Gianni, "Towards a new standardized configuration for the coaxial double test for float glass," *Engineering Structures*, vol. 119, pp. 149–163, 2016.

[108] S. Timoshenko and S. Woinowsky-Krieger, *Theory of plates and shells*. Second Ed. McGraw-Hill New York, NY, USA, 1959.

[109] EN 1288-2, "Glass in building - determination of the bending strength of glass - part 2: Coaxial double ring test on flat specimens with large test surface areas," European Standard, Tech. Rep., 2016.

[110] S. Gulati, R. Akcakaya, and J. Varner, "Fracture behavior of tin vs. air side of float glass," *Ceramic Transactions(USA)*, vol. 122, pp. 317–325, 2000.

[111] G. Irwin, "Analysis of stresses and strains near the end of a crack traversing a plate,"

Elsevier, 1957.

[112] M. Porter, "Aspects of structural design with glass," Ph.D. thesis, University of Oxford, 2001.

[113] Y. J. Chao and S. Liu, "On the failure of cracks under mixed-mode loads," *International journal of fracture*, vol. 87, pp. 201–223, 1997.

[114] D. Kinsella and E. Serrano, "Failure modelling of glass plates in biaxial loading: using flaw-size based weakest-link systems," *Glass Structures & Engineering*, vol. 6, pp. 397–424, 2021.

[115] Y. Li, H. Liu, Y. Shu *et al.*, "Fatigue crack behaviors under asynchronous biaxial loading," *International Journal of Fatigue*, vol. 126, pp. 248–257, 2019.

[116] S. Arunkumar and V. Nithin, "Estimation of stress intensity factor of multiple inclined centre cracks under biaxial loading," *Journal of Failure Analysis and Prevention*, vol. 20, no. 6, pp. 2040–2058, 2020.

[117] J. Eftis and N. Subramonian, "The inclined crack under biaxial load," *Engineering Fracture Mechanics*, vol. 10, no. 1, pp. 43–67, 1978.

[118] M. Janssen, J. Zuidema, and R. Wanhill, *Fracture Mechanics: An Engineering Primer*. TU Delft Open, 2024.

[119] W. Weibull, "A statistical theory of strength of materials," *Proc. Royal Academy Engrg Science*, vol. 15, 1939.

[120] K. C. Datsiou and M. Overend, "Weibull parameter estimation and goodness-of-fit for glass strength data," *Structural Safety*, vol. 73, pp. 29–41, 2018.

[121] B. Demchyna and T. Osadchuk, "Flexural strength of glass using weibull statistic analysis," *Journal of Achievements in Materials and Manufacturing Engineering*, vol. 87, no. 2, pp. 49–61, 2018.

[122] P. Bouška, T. Bittner, M. Eliášová, M. Špaček, M. Vokáč, and T. Mandlík, "Flexural strength of float glass," *Applied Mechanics and Materials*, vol. 732, pp. 341–344, 2015.

[123] EN 61649, "Weibull analysis (IEC 61649:2008), european committee for electrotechnical standardization (CENELEC)," European Standard, Tech. Rep., 2008.

[124] D. Kinsella and K. Persson, "On the applicability of the weibull distribution to model annealed glass strength and future research needs," in *Challenging Glass Conference Proceedings*, vol. 5, 2016, pp. 593–608.

[125] D. Kinsella, "Annealed glass failure modelling: A weakest-link approach with statistical analysis," Ph.D. thesis, Lund University, 2021.

[126] G. Reid, "Effects of spatial variability of glass strength in ring-on-ring tests," *Civil Engineering and Environmental Systems*, vol. 24, no. 2, pp. 139–148, 2007.

[127] K. Natividad, S. Morse, and S. Norville, "Fracture origins and maximum principal stresses in rectangular glass lites," *Journal of Architectural Engineering*, vol. 22, no. 2, p. 04015014, 2016.

[128] ASTM D7264/D7264M, "Standard test method for flexural properties of polymer matrix composite materials," American Society For Testing And Materials, Tech. Rep., 2021.

[129] A. Vedrtnam and S. Pawar, "Experimental and simulation studies on flexural strength of laminated glass using ring-on-ring and three-point bending test," *Proceedings of the school of Mechanical Engineers, Part C: Journal of Mechanical Engineering Science*, vol. 232, no. 21, pp. 3930–3941, 2017.

[130] I. Calderone, P. Davies, S. J. Bennison, H. Xiaokun, and L. Gang, "Effective laminate thickness for the design of laminated glass," in *Glass Processing Days*. Tampere Finland, 2009.

List of Abbreviations

Al_2O_3 Aluminium oxide.

ASTM American Society for Testing and Materials.

B_2O_3 Boric oxide.

Bao Barium oxide.

BISRU Blast Impact and Survivability Research Unit.

BMD Bending Moment Diagram.

CaO Calcium oxide.

CDF Cumulative Distribution Function.

CME Centre for Materials Engineering.

EN European Standard.

EVA Ethylene-Vinyl Acetate.

FEA Finite Element Analysis.

FG Float Glass.

FG_L Float Glass Subjected to Large Loading Span.

FG_M Float Glass Subjected to Medium Loading Span.

FG_S Float Glass Subjected to Small loading span.

FPBT Four-Point Bend Test.

HSG Heat-Strengthened Glass.

K+ Potassium ions.

K_{IC} Fracture Toughness.

LG Laminated Glass.

LG_L Laminated Glass Subjected to Large Loading Span.

LG_M Laminated Glass Subjected to Medium Loading Span.

LG_S Laminated Glass Subjected to Small loading span.

MgO Magnesium oxide.

MPa Megapascal.

Na_2O Sodium oxide.

OSHA Occupational Safety and Health Administration.

PDF Probability Density Function.

PVB PolyVinyl Butyral.

ROR Ring-on-Ring.

SD Standard Deviation.

SFD Shear Force Diagram.

SGP SentryGlas Plus.

SIF Stress Intensity Factor.

SIFs Stress Intensity Factors.

SiO_2 Silicon dioxide also known as silica.

TPBT Three- Point Bend Test.

UV Ulta Violet.

Appendices

Appendix A

Engineering Drawings

The mechanical drawings of the experimental rigs are presented as follows:

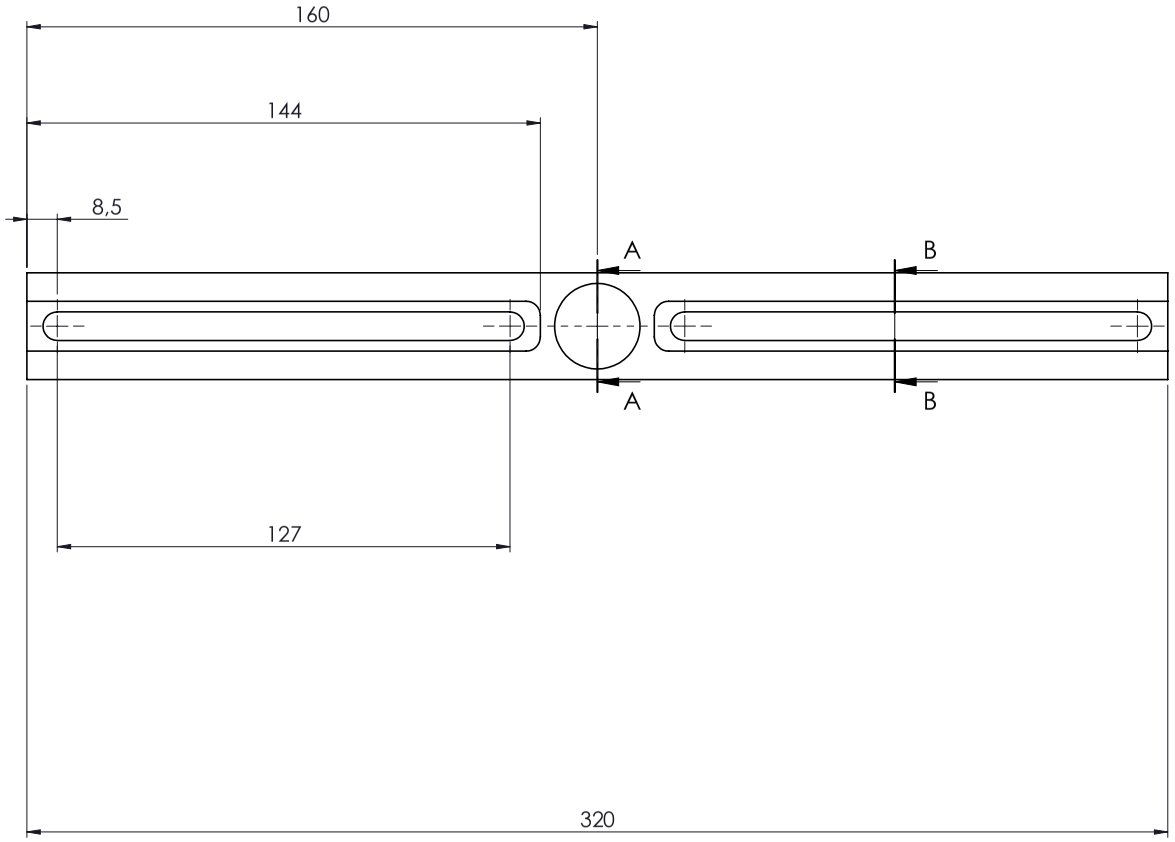

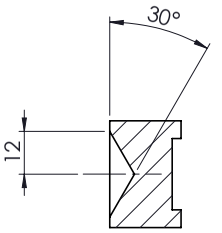

SECTION A-A

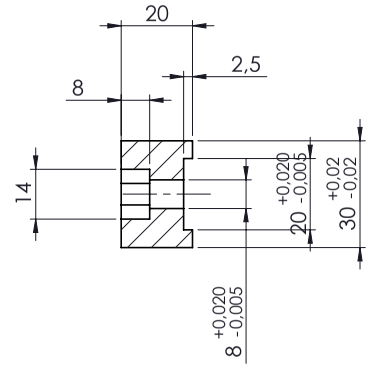

SECTION B-B

All fillet radii 4mm

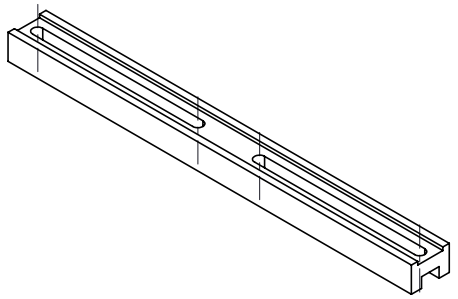

Scale: 1:1.5 on A3	University of Cape Town Department of Mechanical Engineering			
Drawn By: Adebowale	All un-toleranced dimensions to adhere to ISO 2768-m	Title: Slotted Frame		
Checked :	Assembly drawing	Drawing Number :	Rev. : A	Sheet : 1 of 1

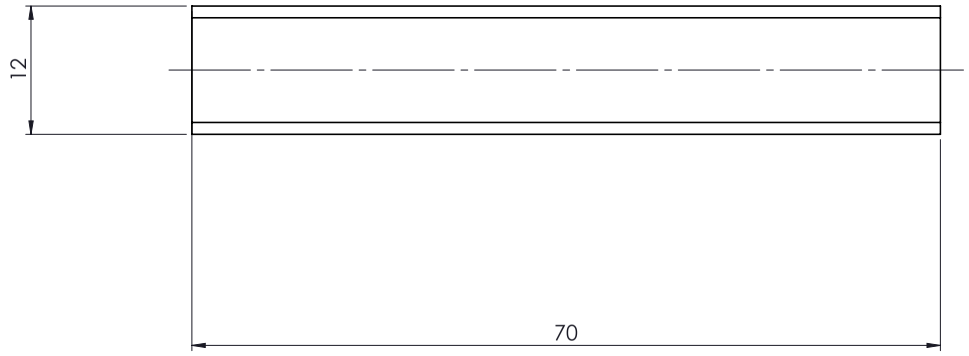

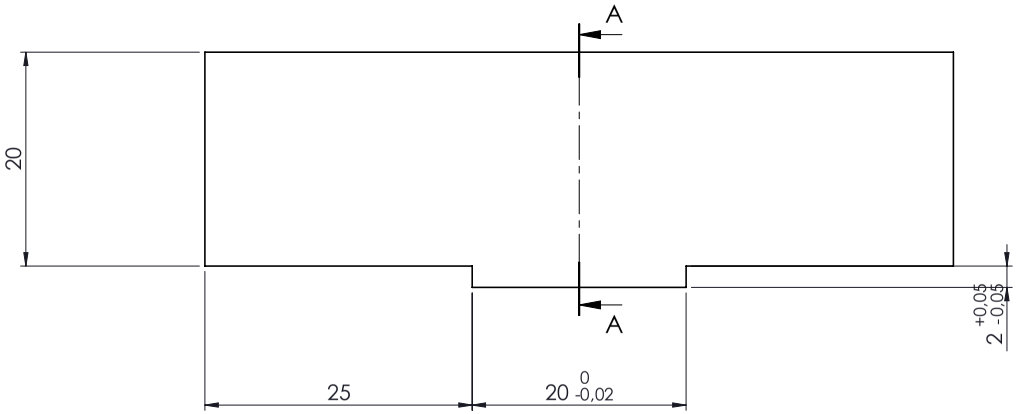

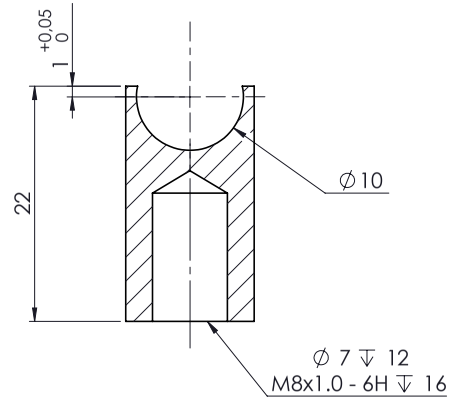

SECTION A-A

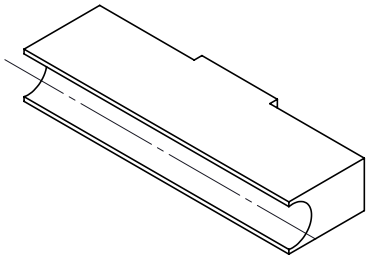

Scale: 2:1 on A3	University of Cape Town Department of Mechanical Engineering			
Drawn By: Adebowale	All un-toleranced dimensions to adhere to ISO 2768-m	Title: Roller holder		
Checked :	Assembly drawing	Drawing Number :	Rev. : A	Sheet : 1 of 1

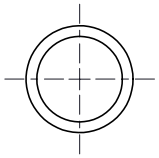

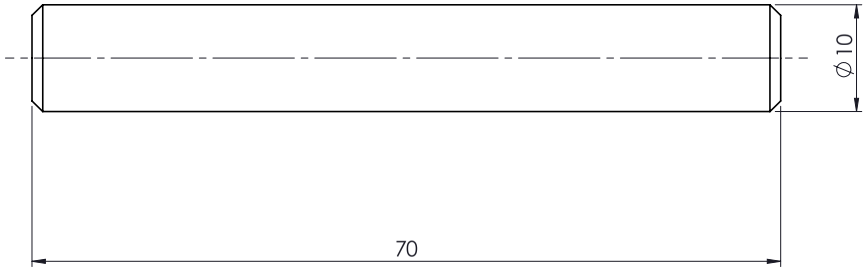

Scale: 2:1 on A3	University of Cape Town Department of Mechanical Engineering			
Drawn By: Adebowale	All un-toleranced dimensions to adhere to ISO 2768-m	Title: Roller pin		
Checked :	Assembly drawing	Drawing Number :	Rev. : A	Sheet : 1 of 1

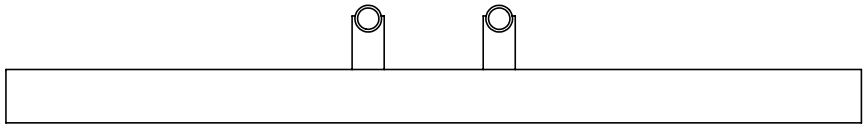

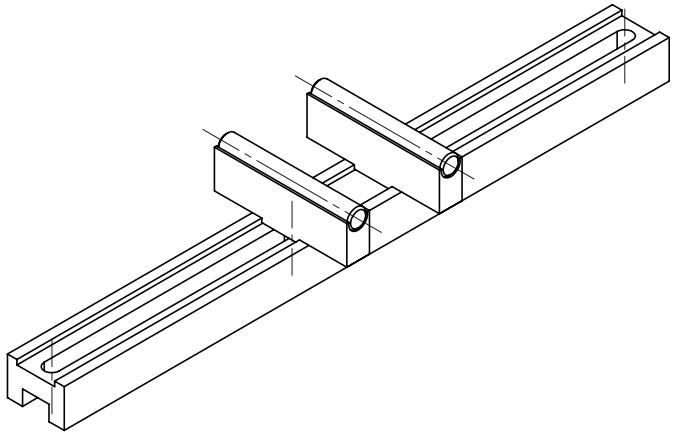

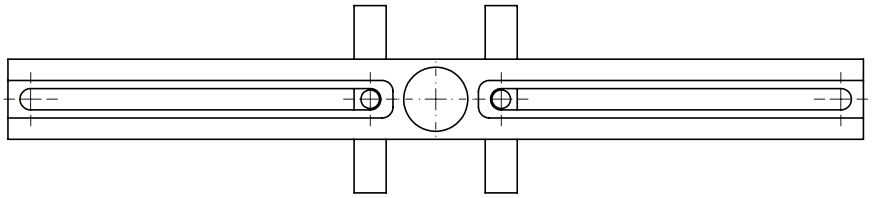

Part Quantity

Roller pin	x2
Roller holder	x2
Slotted Frame	x1

Scale: 1:2 on A3	University of Cape Town Department of Mechanical Engineering			
Drawn By: Adebowale Adeniran	All un-toleranced dimensions to adhere to ISO 2768-m	Title: FPBT load rig		
Checked :	Assembly drawing	Drawing Number :	Rev. : A	Sheet : 1 of 1

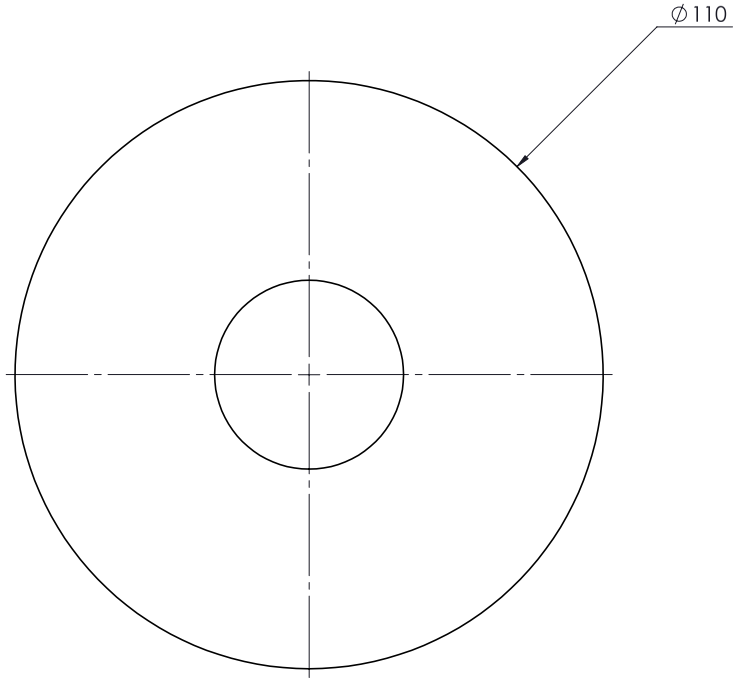

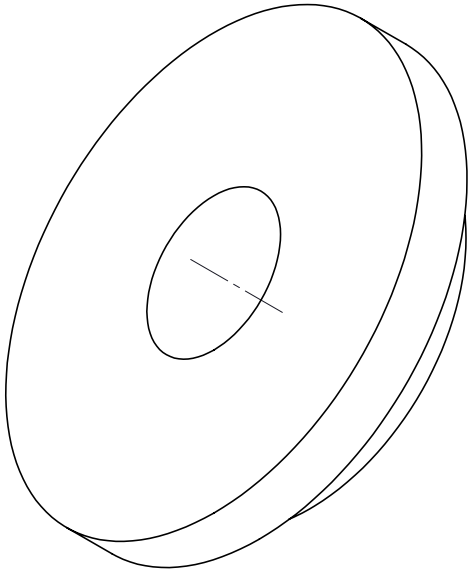

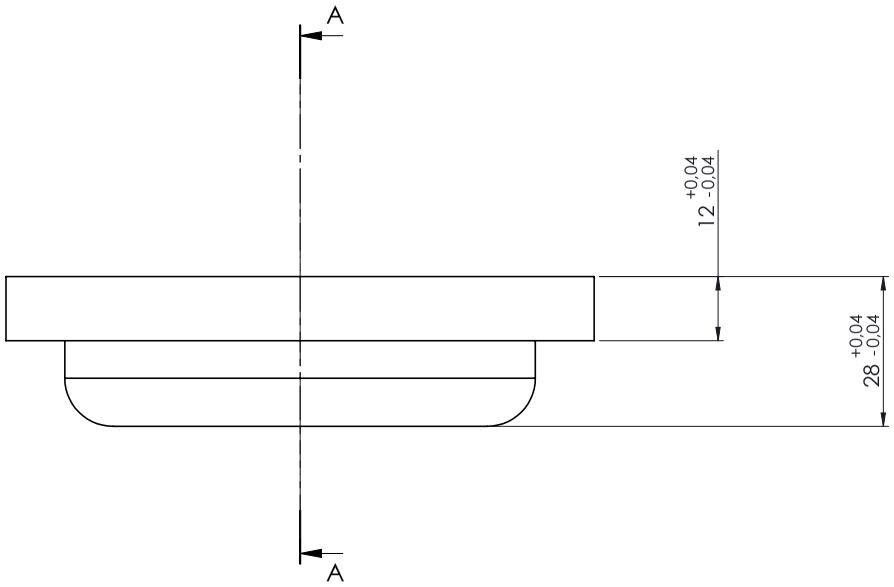

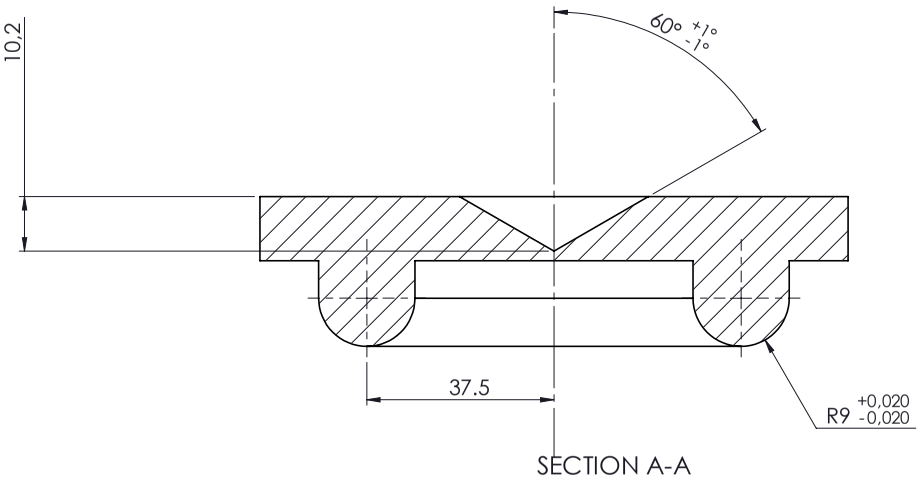

SECTION A-A

Scale: 1:1 on A3	University of Cape Town Department of Mechanical Engineering			
Drawn By: Adebowale Adeniran	All un-toleranced dimensions to adhere to ISO 2768-m	Title: load ring 1		
Checked :	Assembly drawing	Drawing Number : 1of 4	Rev. : A	Sheet : 1 of 1

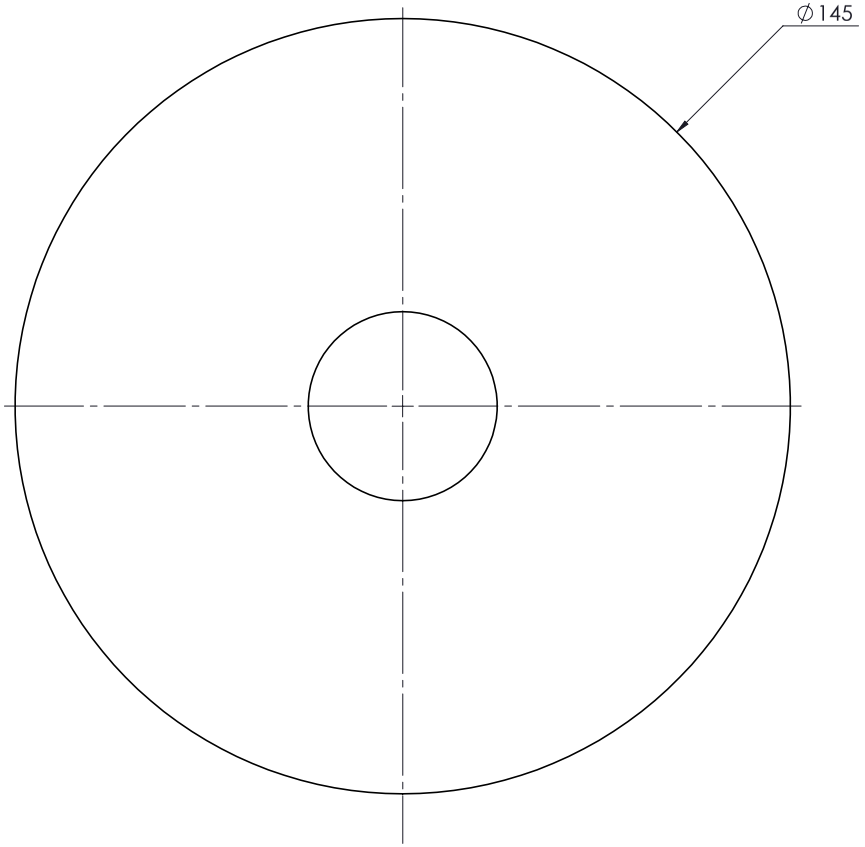

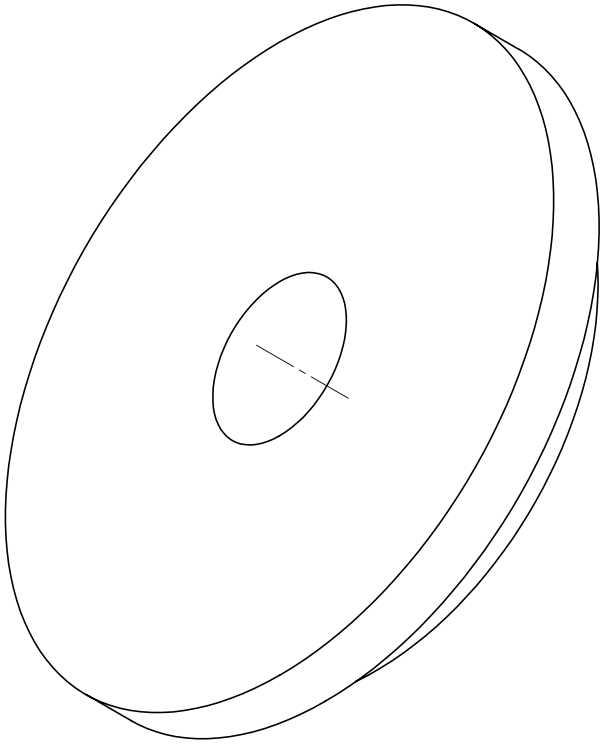

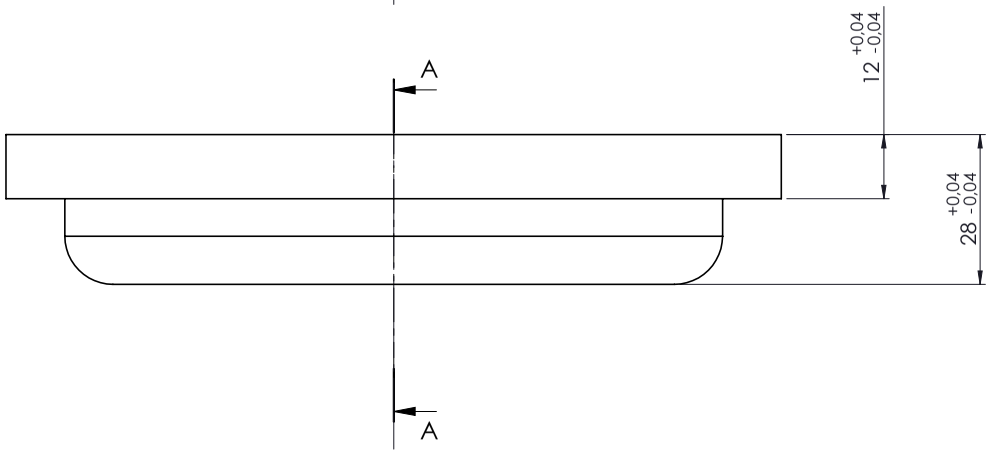

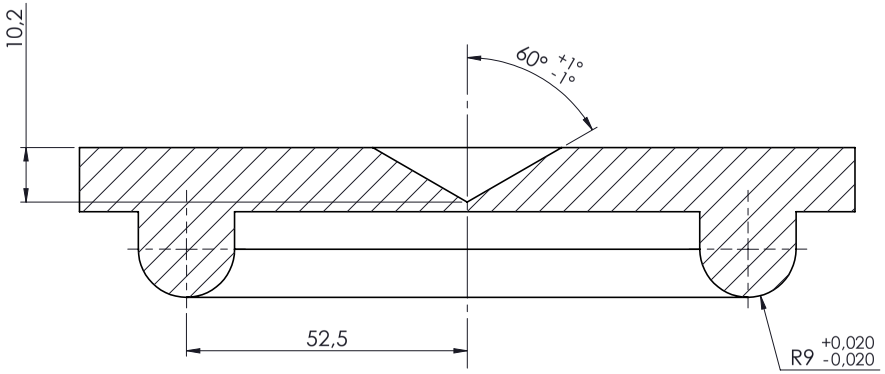

SECTION A-A

Scale: 1:1 on A3	University of Cape Town Department of Mechanical Engineering			
Drawn By: Adebowale Adeniran	All un-toleranced dimensions to adhere to ISO 2768-m	Title: load ring 2		
Checked :	Assembly drawing	Drawing Number : 2 of 4	Rev. : A	Sheet : 1 of 1

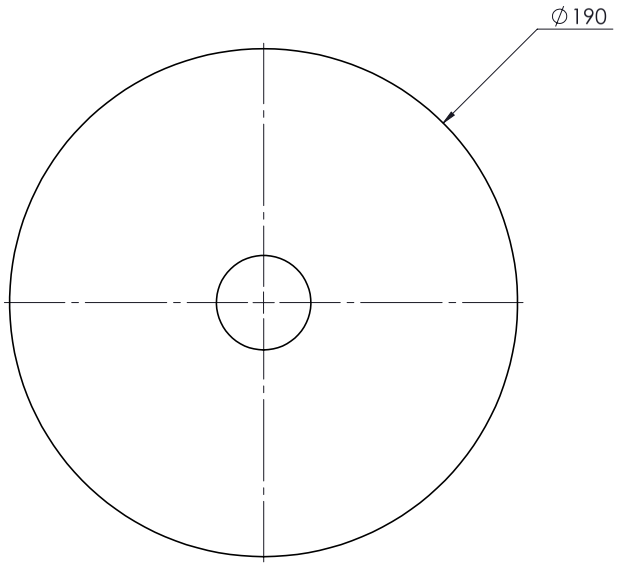

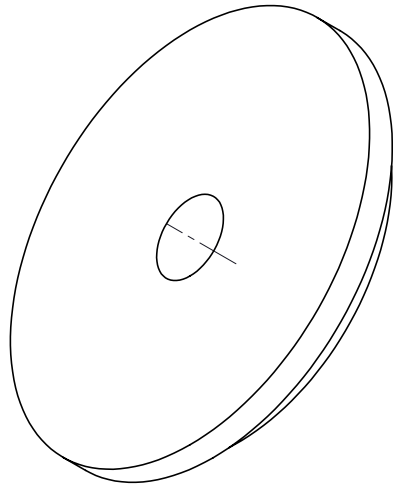

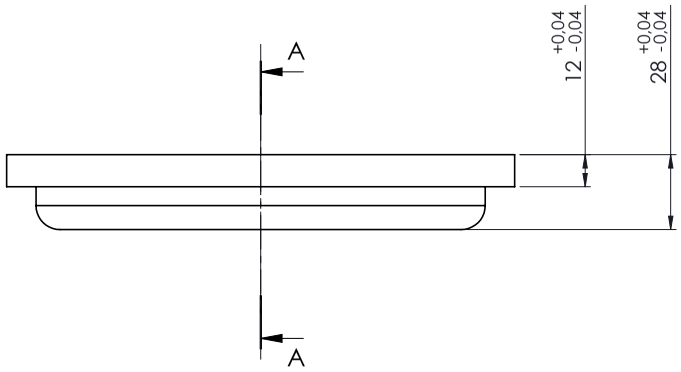

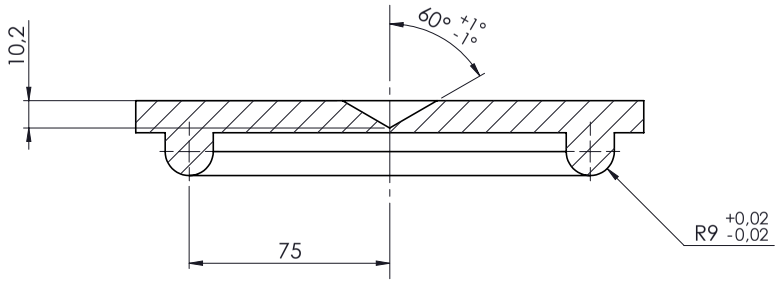

SECTION A-A

Scale: 1:2 on A3	University of Cape Town Department of Mechanical Engineering			
Drawn By: Adebowale Adeniran	All un-toleranced dimensions to adhere to ISO 2768-m	Title: Load ring 3		
Checked :	Assembly drawing	Drawing Number : 3 of 4	Rev. : A	Sheet : 1 of 1

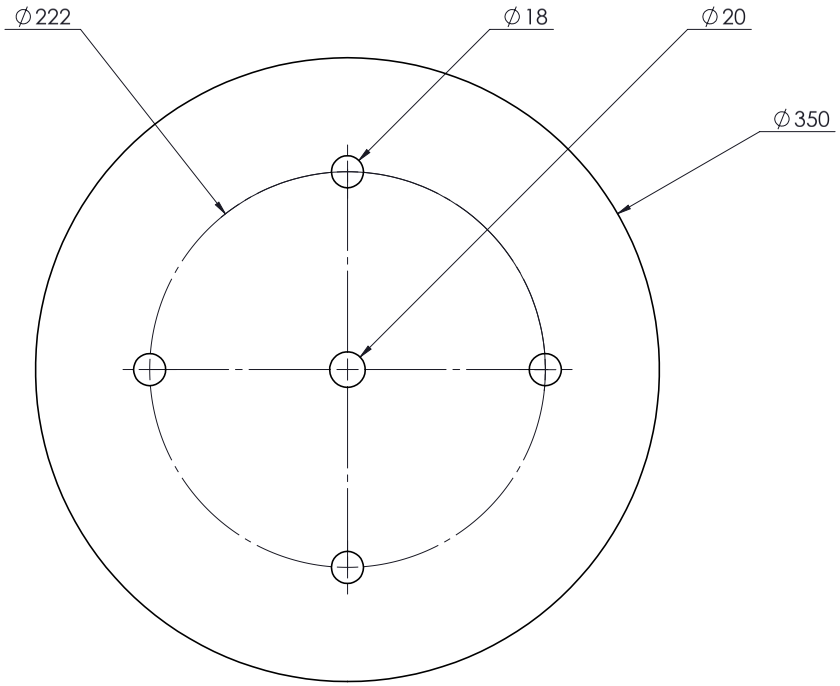

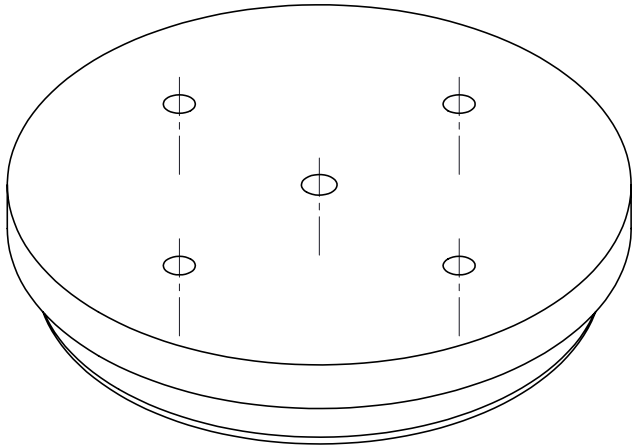

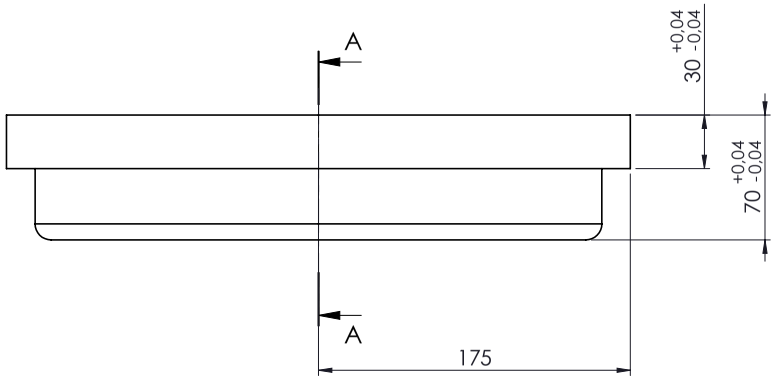

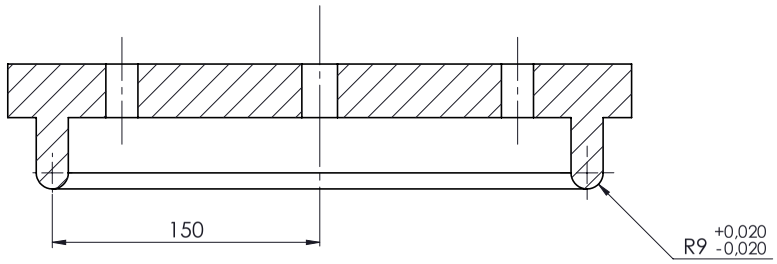

SECTION A-A

Scale: 1:3 on A3	University of Cape Town Department of Mechanical Engineering			
Drawn By: Adebowale Adeniran	All un-toleranced dimensions to adhere to ISO 2768-m	Title: Support ring		
Checked :	Assembly drawing	Drawing Number : 4 of 4	Rev. : A	Sheet : 1 of 1

Appendix B

Convergence Plots

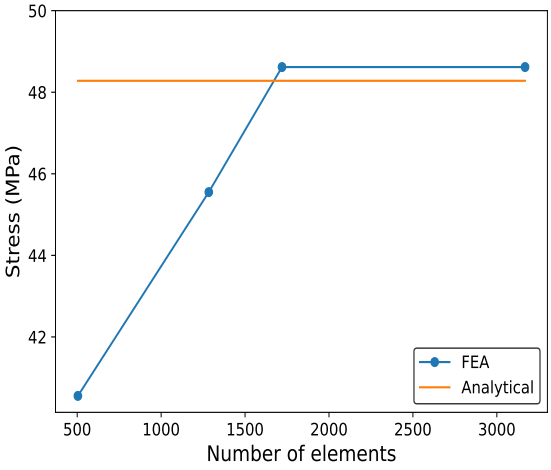

a. FG under small loading span

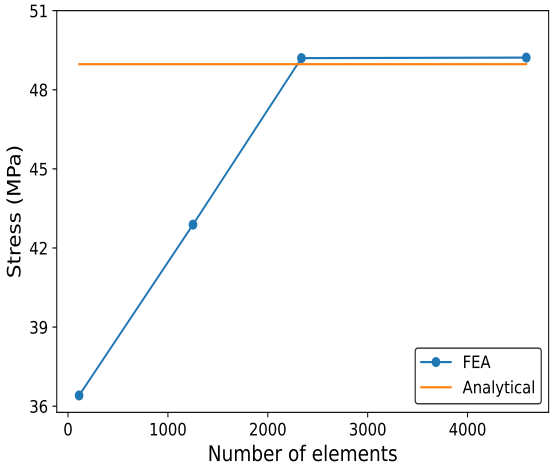

b. LG under small loading span

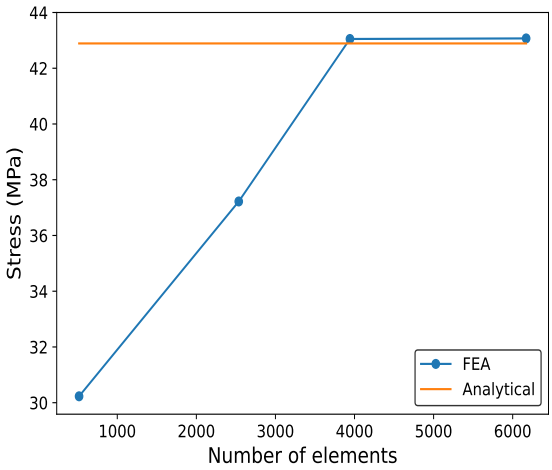

c. FG under medium loading span

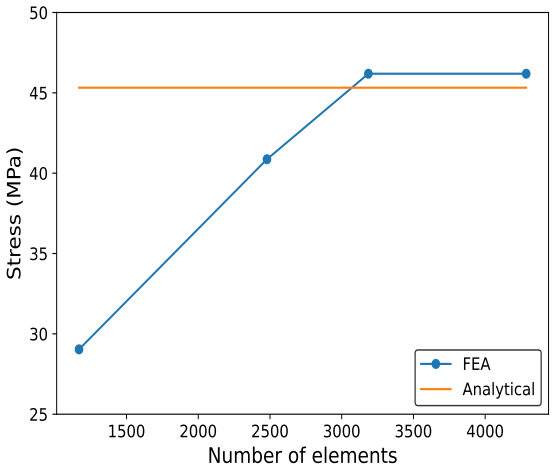

d. LG under medium loading span

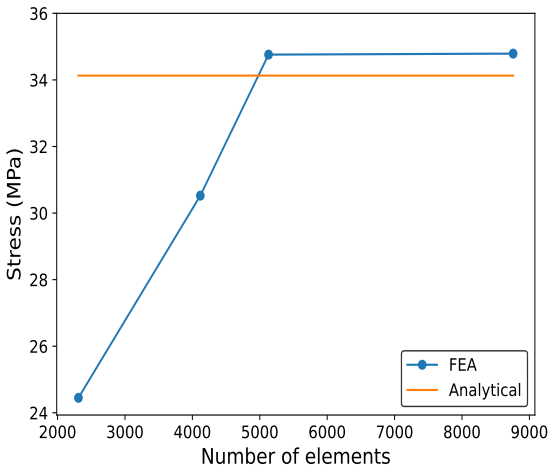

e. FG under large loading span

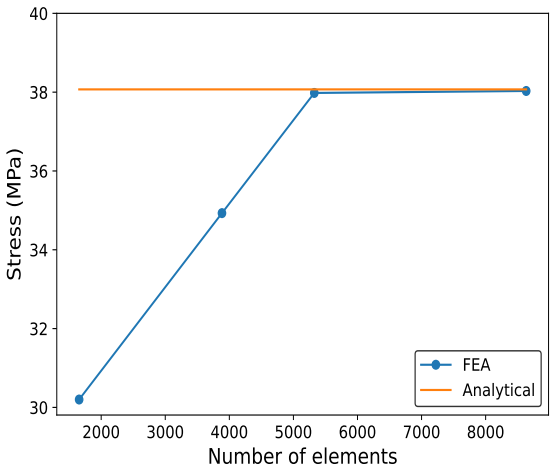

f. LG under large loading span

Figure B.1 Graphs showing FEA stress convergence with the analytical result of FPBT test

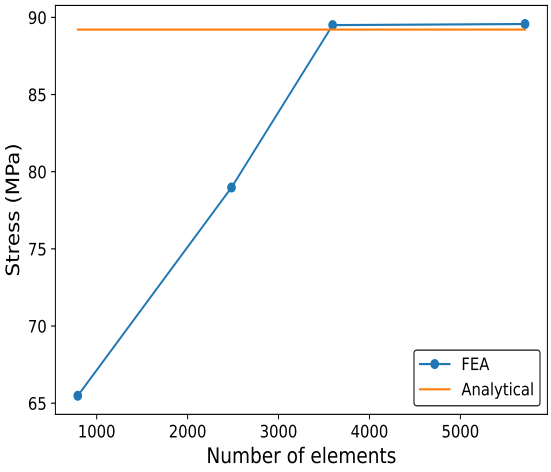

a. FG under small loading span

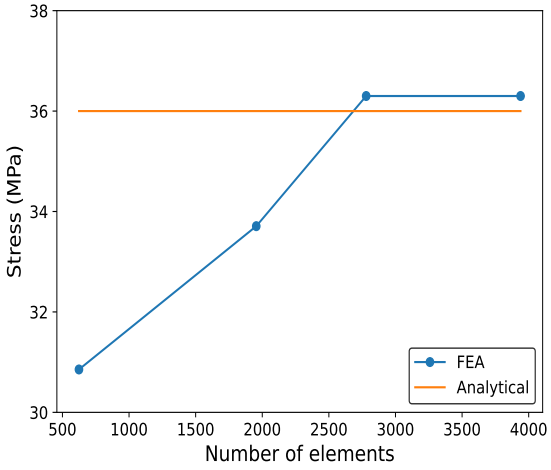

b. LG under small loading span

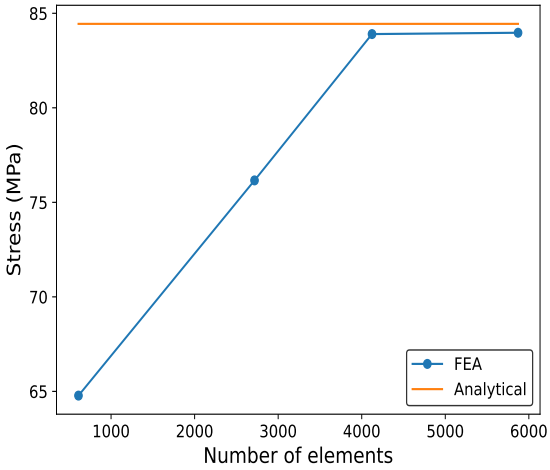

c. FG under medium loading span

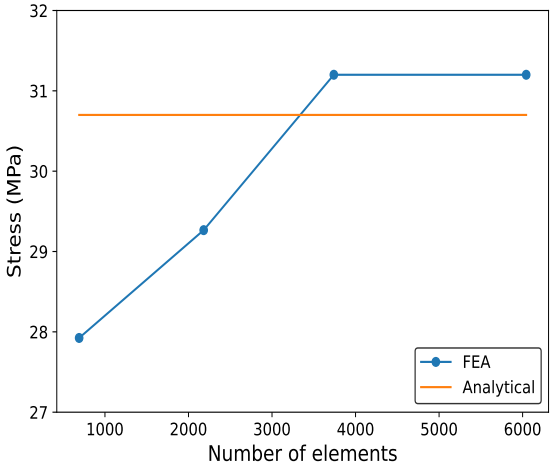

d. LG under medium loading span

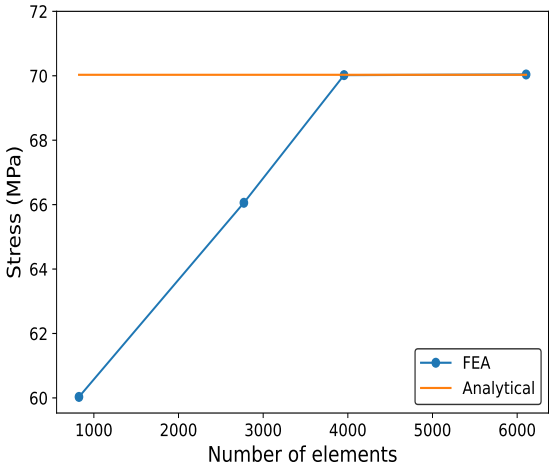

e. FG under large loading span

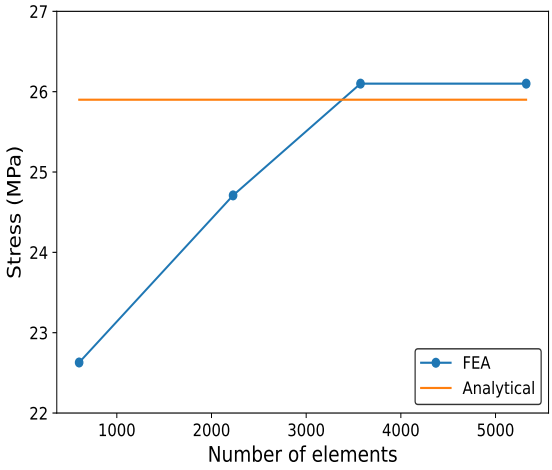

f. LG under large loading span

Figure B.2 Graphs showing FEA stress convergence with the analytical result of ROR test

Appendix C

Confidence Interval (CI) Formula

Since the sample size is small and the population standard deviation is unknown, the t-distribution is used to calculate the 95% confidence interval. The 95% confidence interval was calculated using the following formula:

$$CI = \bar{x} \pm t_{\alpha/2,N-1} \left(\frac{s}{\sqrt{N}} \right) \tag{C.1}$$

where:

- $\bar{x}$ is the sample mean,
- s is the sample standard deviation,
- N is the sample size,
- $t_{\alpha/2,N-1}$ is the t-critical value from the t-distribution.

For a 95% confidence interval, the significance level is $\alpha = 0.05$, which gives $\alpha/2 = 0.025$ for each tail of the distribution. Using the degrees of freedom ($df = N-1$) and the significance level, the t-critical value, $t_{\alpha/2,N-1}$, is obtained from the t-distribution table.

Appendix D

Results in detail

D.1 Quasi-Static Four Point Bend Test Results

The following are the force-displacement graphs of specimens subjected to the four-point bend test.

Force -displacement graphs of specimens subjected to four-point bend test

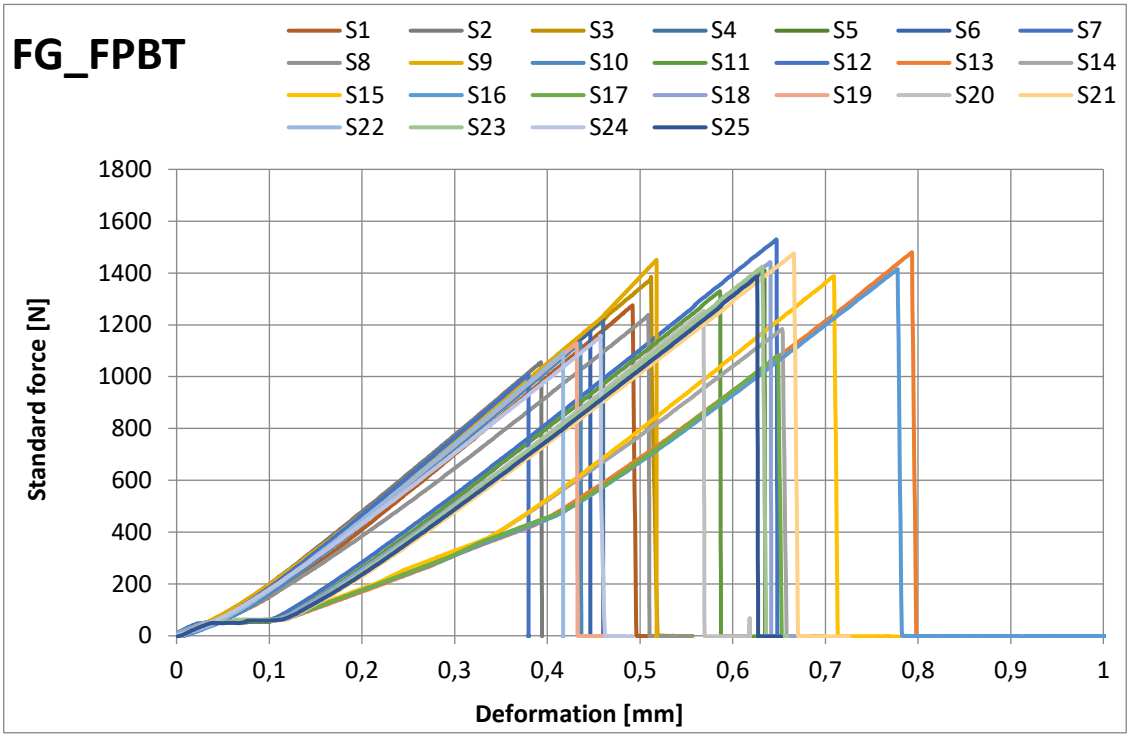

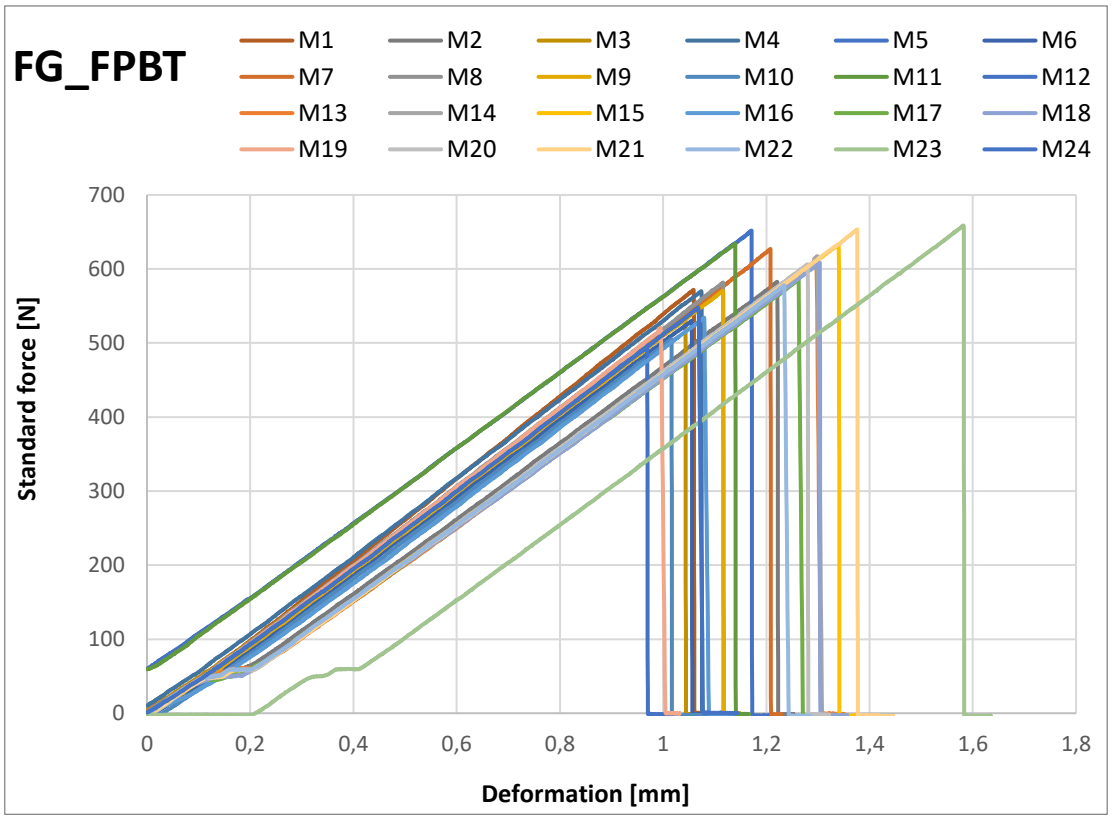

Force -displacement graphs of specimens subjected to four-point bend test

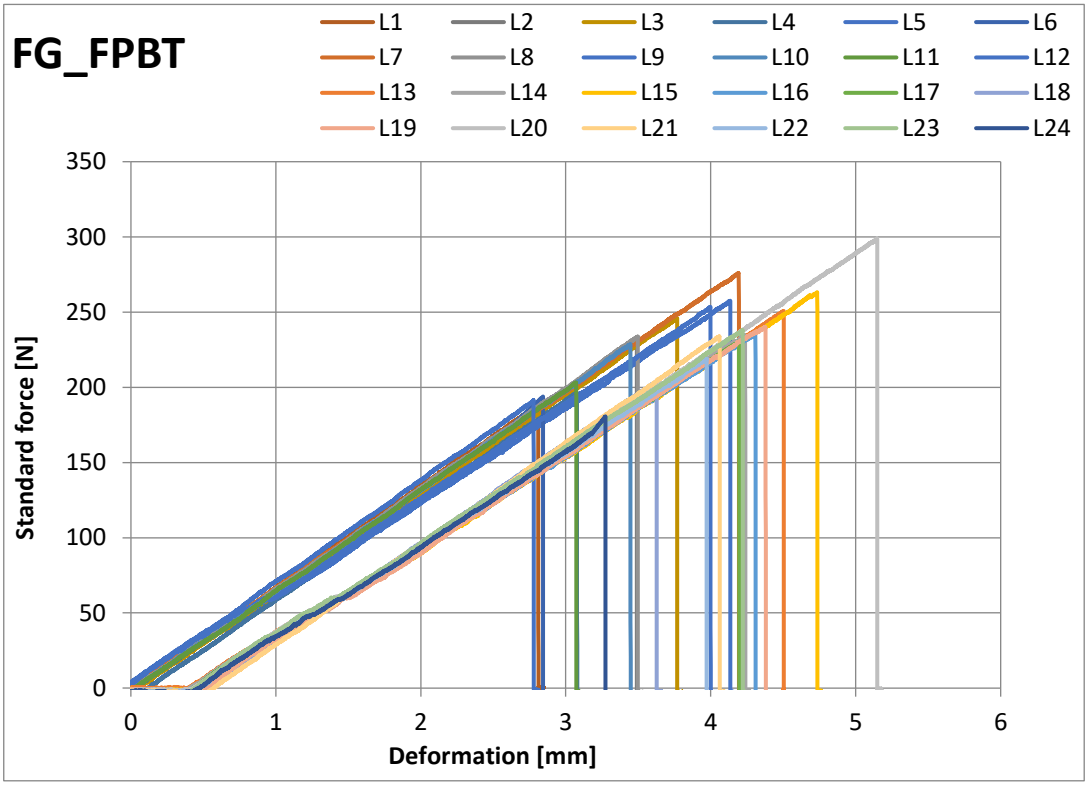

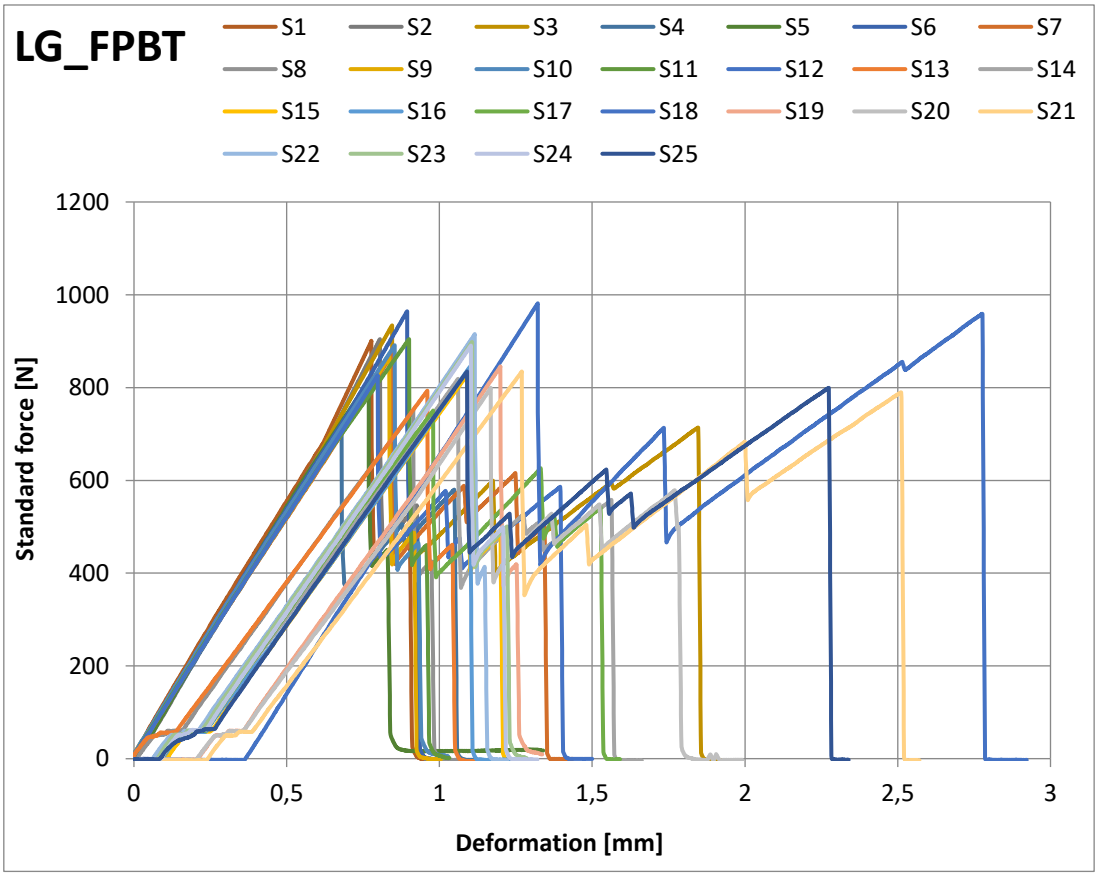

Force -displacement graphs of specimens subjected to four-point bend test

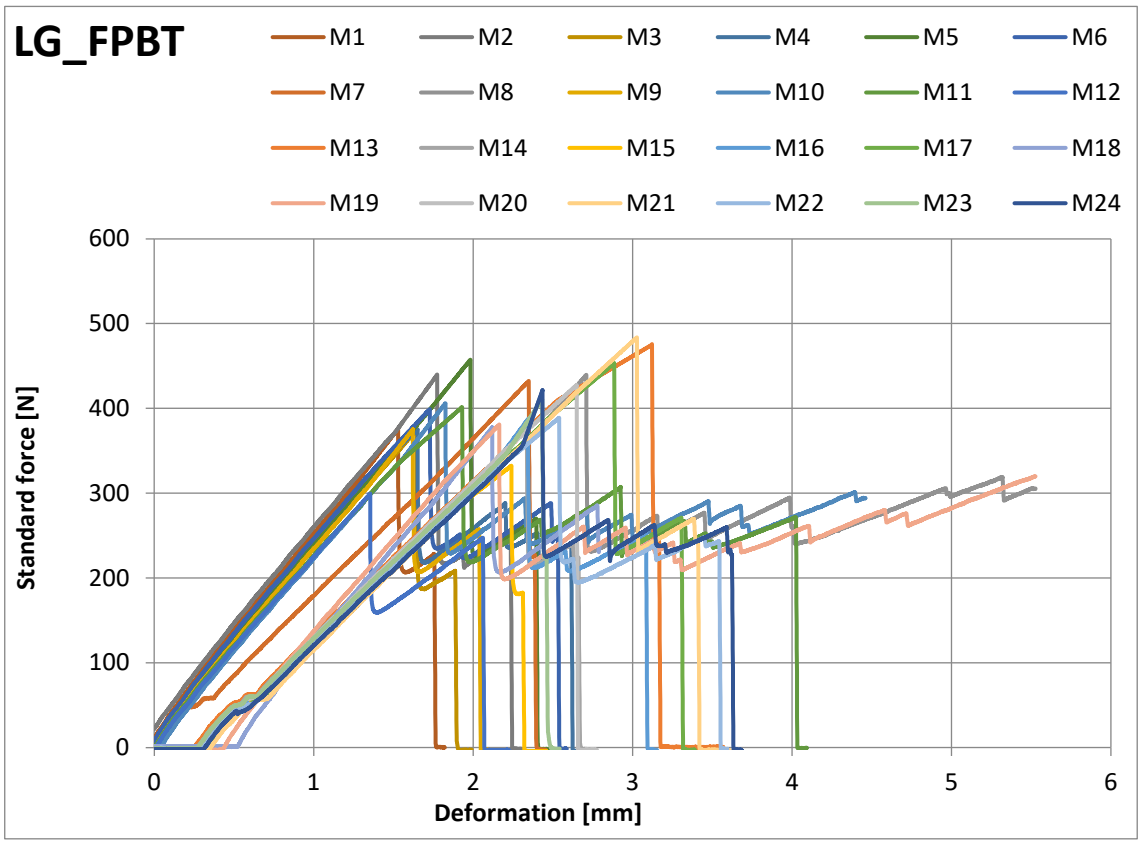

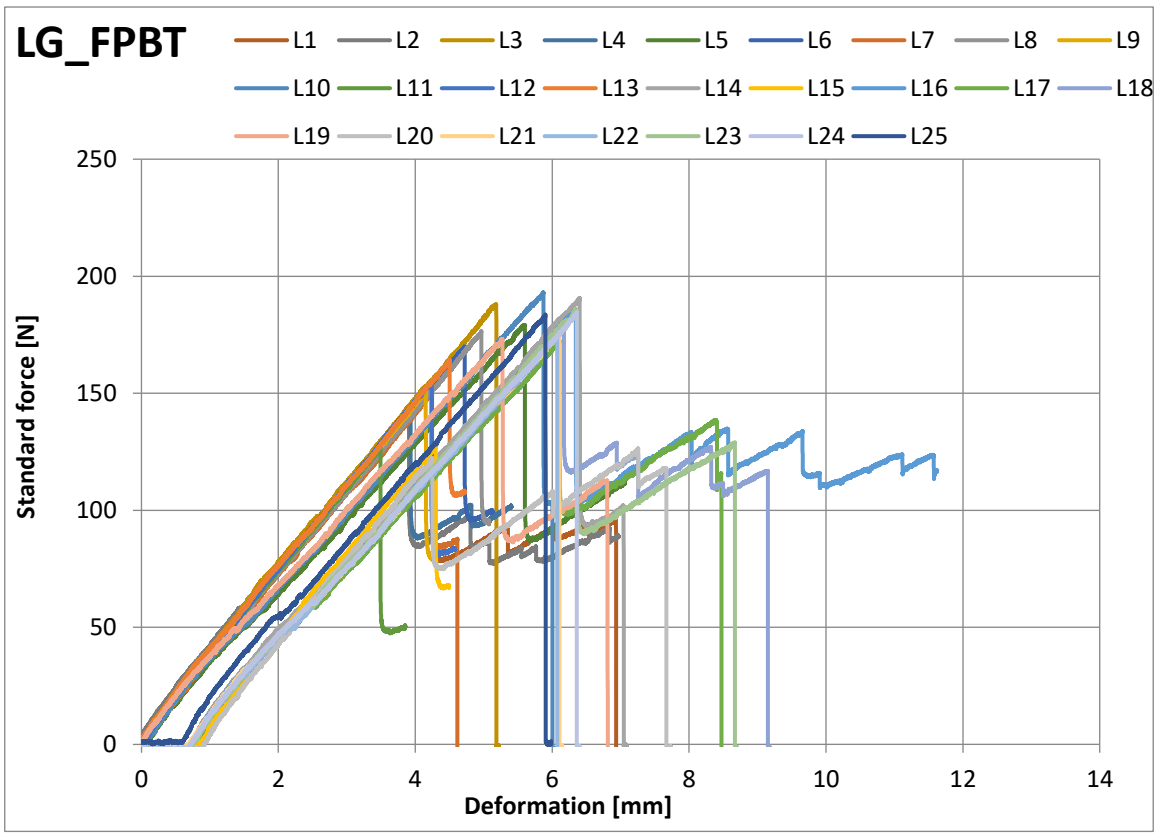

D.2 Quasi-Static Ring-on-Ring Tests Results

The following are the force-displacement graphs of specimens subjected to the ring-on-ring test.

Force -displacement graphs of specimens subjected to ring-on-ring test

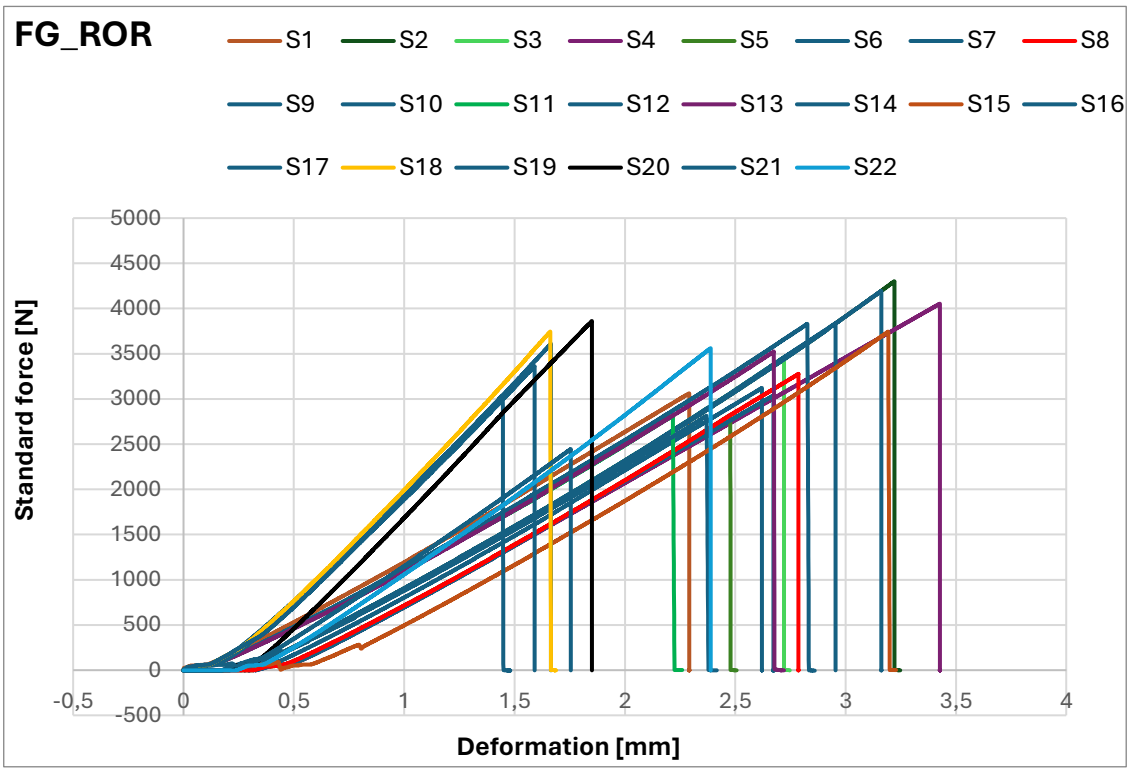

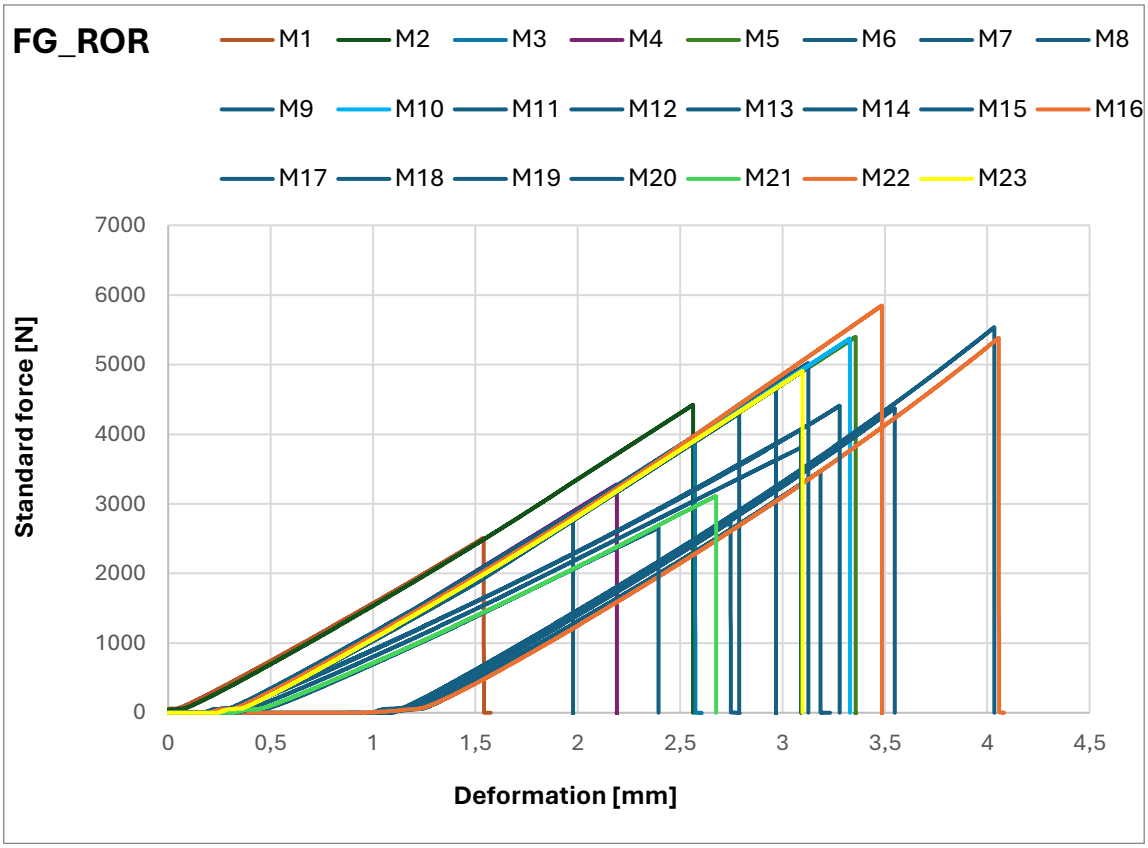

Force -displacement graphs of specimens subjected to ring-on-ring test

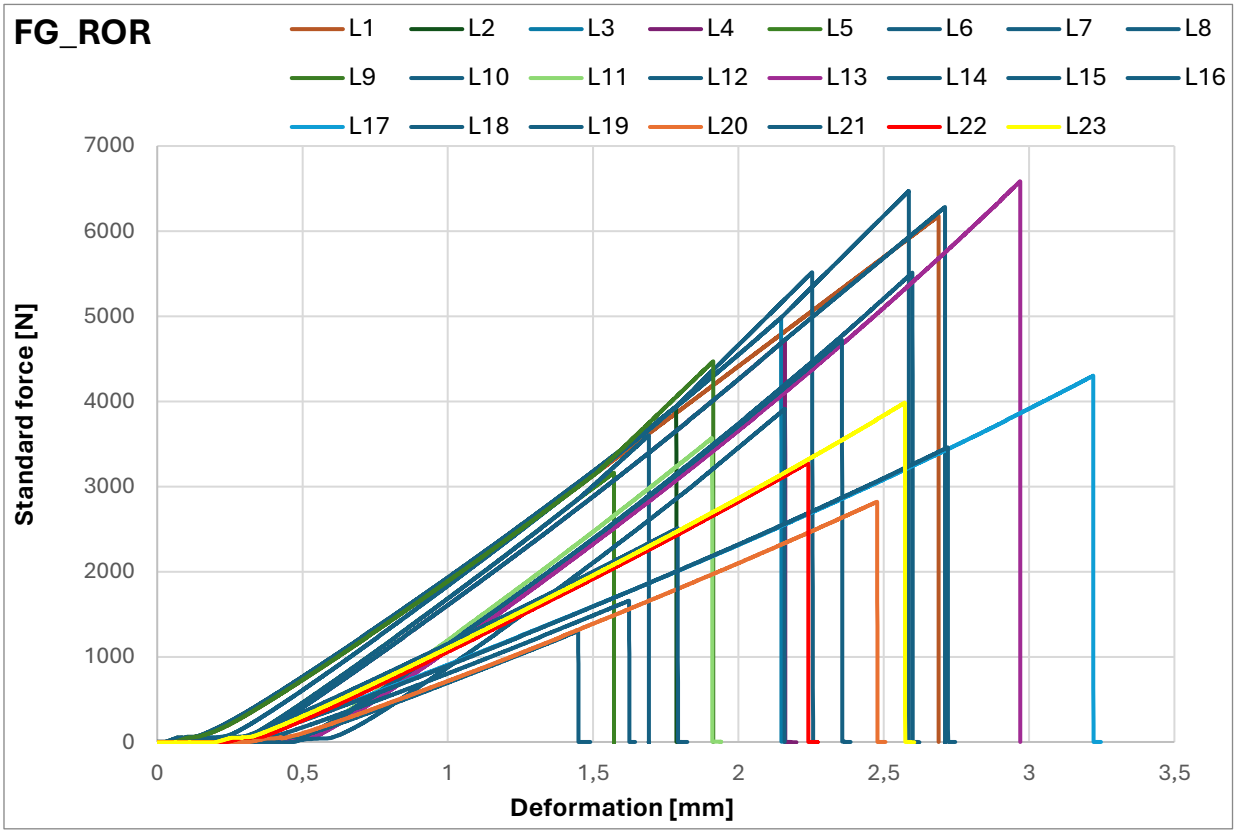

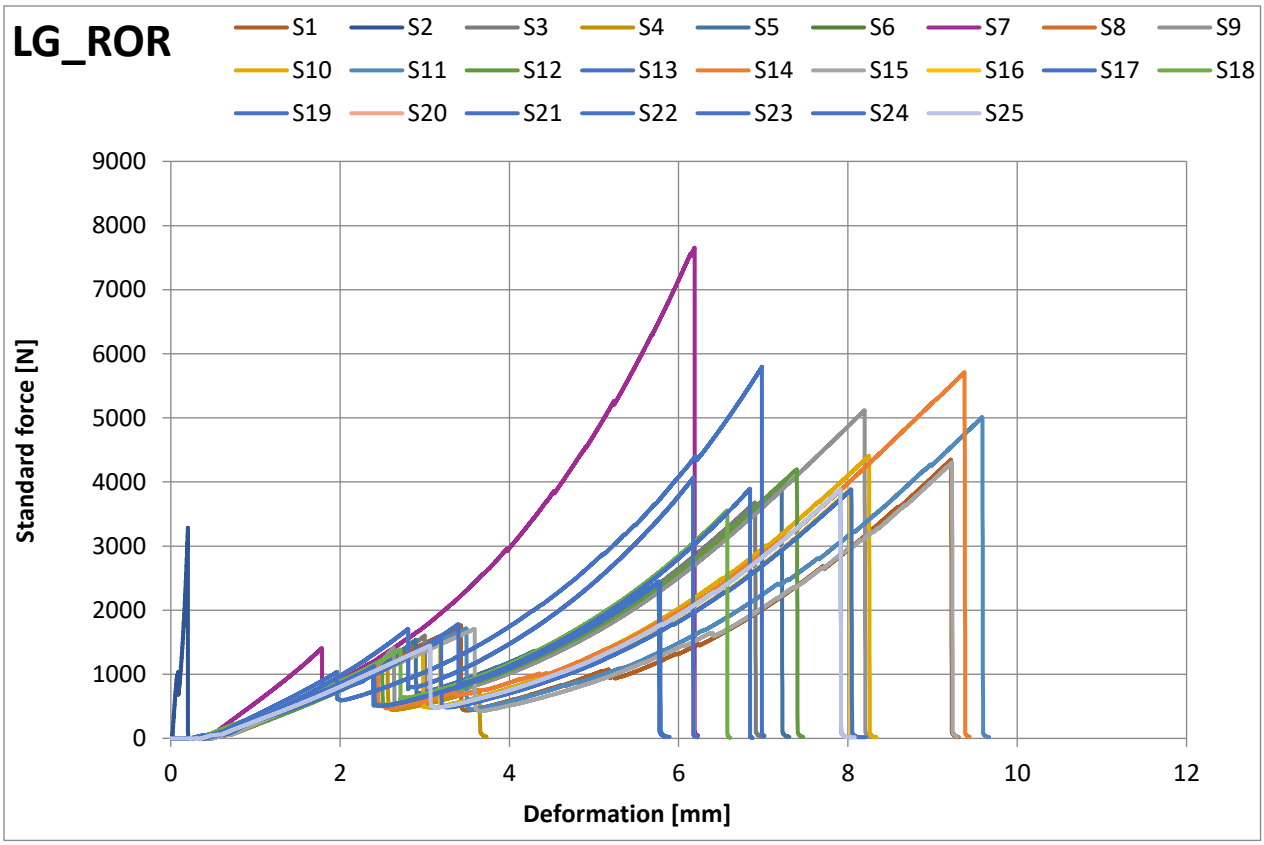

Force -displacement graphs of specimens subjected to ring-on-ring test

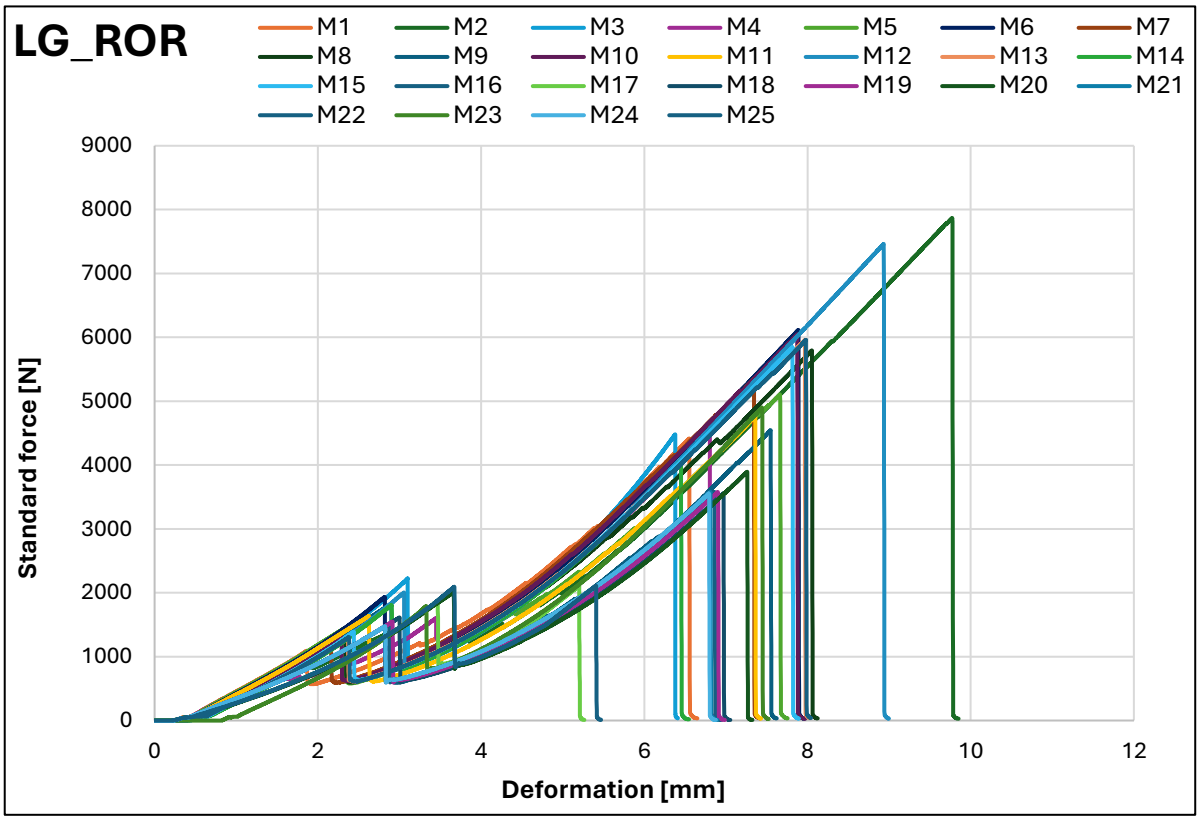

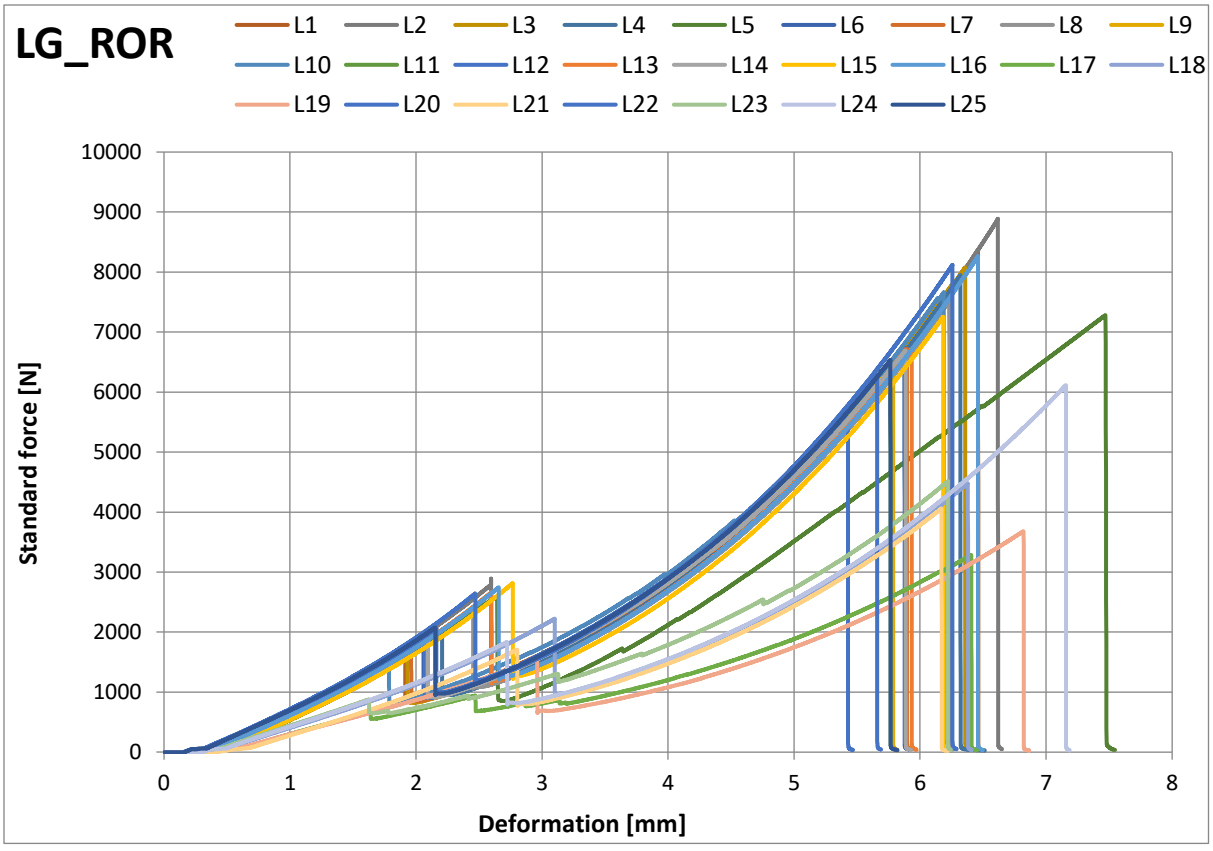

D.3 Results in Tabular Form

The following tables contain the force generated from the Zwick machine and the calculated fracture strength for float glass and laminated glass subjected to small, medium and large loading areas of the FPBT and ROR test.

Table D.1 *Recorded failure load and calculated failure stress of float glass specimens subjected to FPBT*

Specimens	Failure Load (N)	Failure Stress (MPa)	Specimens	Failure Load (N)	Failure Stress (MPa)	Specimens	Failure Load (N)	Failure Stress (MPa)
FG_S1	1275.08	47.91	FG_M1	571.89	42.11	FG_L1	189.64	28.50
FG_S2	1056.06	39.68	FG_M2	582.48	42.89	FG_L2	229.27	34.46
FG_S3	1384.30	52.01	FG_M3	536.59	39.51	FG_L3	246.16	36.99
FG_S4	1221.22	45.88	FG_M4	569.83	41.96	FG_L4	196.45	29.52
FG_S5	1409.63	52.96	FG_M5	651.71	47.99	FG_L5	257.58	38.71
FG_S6	1176.30	44.20	FG_M6	530.14	39.04	FG_L6	193.98	29.15
FG_S7	1529.92	57.48	FG_M7	627.21	46.19	FG_L7	256.06	38.48
FG_S8	1238.16	46.52	FG_M8	581.60	42.83	FG_L8	233.80	35.14
FG_S9	1450.52	54.50	FG_M9	570.61	42.02	FG_L9	253.54	38.10
FG_S10	1130.36	42.47	FG_M10	504.97	37.19	FG_L10	228.80	34.39
FG_S11	1330.03	49.97	FG_M11	634.11	46.70	FG_L11	203.25	30.55
FG_S12	1008.56	37.89	FG_M12	497.26	36.62	FG_L12	191.49	28.78
FG_S13	1480.97	55.64	FG_M13	605.90	44.62	FG_L13	250.72	37.68
FG_S14	1184.24	44.49	FG_M14	617.25	45.45	FG_L14	234.64	35.26
FG_S15	1388.34	52.16	FG_M15	632.76	46.60	FG_L15	253.33	38.07
FG_S16	1414.82	53.16	FG_M16	534.20	39.34	FG_L16	235.54	35.40
FG_S17	1080.98	40.61	FG_M17	589.26	43.39	FG_L17	230.81	34.69
FG_S18	1442.64	54.20	FG_M18	608.44	44.81	FG_L18	203.95	30.65
FG_S19	1129.98	42.46	FG_M19	520.80	38.35	FG_L19	240.01	36.07
FG_S20	1254.23	47.12	FG_M20	606.24	44.64	FG_L20	219.09	32.93
FG_S21	1475.12	55.42	FG_M21	653.37	48.11	FG_L21	234.01	35.17
FG_S22	1094.46	41.12	FG_M22	577.96	42.56	FG_L22	249.44	37.49
FG_S23	1424.90	53.54	FG_M23	658.79	48.51	FG_L23	238.06	35.78
FG_S24	1157.82	43.50	FG_M24	548.11	40.36	FG_L24	180.62	27.14
FG_S25	1386.90	52.11	-	-	-	-	-	-

Table D.2 *Recorded failure load and calculated failure stress of LG specimens subjected to four-point bend test*

Specimens	Failure Load (N)	Failure Stress (MPa)	Specimens	Failure Load (N)	Failure Stress (MPa)	Specimens	Failure Load (N)	Failure Stress (MPa)
LG_S1	900.87	51.56	LG_M1	375.88	42.18	LG_L1	153.46	35.21
LG_S2	904.33	51.76	LG_M2	440.04	49.37	LG_L2	143.58	32.94
LG_S3	934.26	53.48	LG_M3	374.40	42.01	LG_L3	188.08	43.15
LG_S4	720.71	41.25	LG_M4	375.40	42.12	LG_L4	142.97	32.80
LG_S5	814.62	46.63	LG_M5	457.39	51.32	LG_L5	179.18	41.10
LG_S6	964.23	55.19	LG_M6	399.21	44.79	LG_L6	170.00	39.00
LG_S7	872.09	49.92	LG_M7	432.54	48.53	LG_L7	150.27	34.47
LG_S8	750.62	42.96	LG_M8	439.39	49.30	LG_L8	176.46	40.48
LG_S9	866.37	49.59	LG_M9	375.18	42.10	LG_L9	150.90	34.62
LG_S10	891.17	51.01	LG_M10	406.03	45.56	LG_L10	193.08	44.29
LG_S11	904.12	51.75	LG_M11	401.60	45.06	LG_L11	127.06	29.15
LG_S12	826.49	47.31	LG_M12	299.29	33.58	LG_L12	155.18	35.60
LG_S13	793.38	45.41	LG_M13	475.88	53.40	LG_L13	164.25	37.68
LG_S14	819.00	46.88	LG_M14	377.86	42.40	LG_L14	190.76	43.76
LG_S15	829.67	47.49	LG_M15	332.21	37.28	LG_L15	127.37	29.22
LG_S16	844.76	48.35	LG_M16	387.38	43.47	LG_L16	185.84	42.63
LG_S17	750.80	42.97	LG_M17	453.39	50.87	LG_L17	172.66	39.61
LG_S18	981.80	56.20	LG_M18	377.81	42.39	LG_L18	177.97	40.83
LG_S19	846.00	48.42	LG_M19	380.92	42.74	LG_L19	173.17	39.73
LG_S20	799.84	45.78	LG_M20	427.54	47.97	LG_L20	122.07	28.00
LG_S21	834.53	47.77	LG_M21	483.87	54.29	LG_L21	175.84	40.34
LG_S22	915.76	52.42	LG_M22	389.10	43.66	LG_L22	175.31	40.22
LG_S23	898.55	51.43	LG_M23	411.00	46.12	LG_L23	185.92	42.65
LG_S24	890.45	50.97	LG_M24	421.41	47.28	LG_L24	184.55	42.34
LG_S25	834.65	47.77	-	-	-	LG_L25	182.96	41.97

Table D.3 *Recorded failure load and calculated failure stress of float glass specimens subjected to ROR test*

Specimens	Failure Load (N)	Failure Stress (MPa)	Specimens	Failure Load (N)	Failure Stress (MPa)	Specimens	Failure Load (N)	Failure Stress (MPa)
FG_S1	3061.34	79.58	FG_M1	2509.80	51.00	FG_L1	6176.15	86.87
FG_S2	4300.70	111.79	FG_M2	4421.73	89.86	FG_L2	3939.69	55.41
FG_S3	3459.77	89.93	FG_M3	3983.82	80.96	FG_L3	4981.96	70.08
FG_S4	4053.70	105.37	FG_M4	3278.69	66.63	FG_L4	4722.99	66.43
FG_S5	2820.83	73.32	FG_M5	5399.75	109.73	FG_L5	3162.44	44.48
FG_S6	3120.83	81.12	FG_M6	2869.92	58.32	FG_L6	5514.90	77.57
FG_S7	3037.67	78.96	FG_M7	4793.63	97.41	FG_L7	6470.79	91.02
FG_S8	3276.38	85.17	FG_M8	5020.07	102.02	FG_L8	3601.06	50.65
FG_S9	4194.18	109.02	FG_M9	4297.73	87.34	FG_L9	4472.09	62.90
FG_S10	3835.88	99.71	FG_M10	5375.40	109.24	FG_L10	6282.34	88.37
FG_S11	2811.93	73.09	FG_M11	2744.66	55.78	FG_L11	3569.42	50.21
FG_S12	3830.88	99.58	FG_M12	3471.02	70.54	FG_L12	5512.86	77.54
FG_S13	3523.54	91.59	FG_M13	5536.97	112.52	FG_L13	6584.36	92.61
FG_S14	2814.64	73.16	FG_M14	4373.83	88.88	FG_L14	3909.05	54.98
FG_S15	3742.75	97.29	FG_M15	3282.96	66.71	FG_L15	4723.06	66.43
FG_S16	3361.34	87.37	FG_M16	5383.27	109.40	FG_L16	3001.00	42.21
FG_S17	3610.07	93.84	FG_M17	3815.11	77.53	FG_L17	6092.19	85.69
FG_S18	3743.26	97.30	FG_M18	2659.09	54.04	FG_L18	4017.24	56.51
FG_S19	3037.67	78.96	FG_M19	4408.04	89.58	FG_L19	5178.44	72.84
FG_S20	3860.65	100.35	FG_M20	3112.13	63.24	FG_L20	6213.96	87.40
FG_S21	2445.50	63.57	FG_M21	4070.92	82.73	FG_L21	4527.50	63.68
FG_S22	3560.65	92.56	FG_M22	5849.24	118.87	FG_L22	6848.40	96.33
FG_S23			FG_M23	4909.27	99.76	FG_L23	5004.90	70.40

Table D.4 *Recorded failure load and calculated failure stress of laminated glass specimens subjected to ROR test*

Specimens	Failure Load (N)	Failure Stress (MPa)	Specimens	Failure Load (N)	Failure Stress (MPa)	Specimens	Failure Load (N)	Failure Stress (MPa)
LG_S1	1763.69	45.09	LG_M1	1092.69	20.92	LG_L1	1597.04	21.16
LG_S2	1092.28	27.92	LG_M2	1381.50	26.44	LG_L2	2889.51	38.28
LG_S3	1608.73	41.13	LG_M3	2223.07	42.55	LG_L3	1562.07	20.70
LG_S4	1188.21	30.38	LG_M4	1603.47	30.69	LG_L4	2016.45	26.72
LG_S5	1539.66	39.36	LG_M5	1446.94	27.70	LG_L5	2599.75	34.44
LG_S6	1114.22	28.49	LG_M6	1935.95	37.06	LG_L6	1844.79	24.44
LG_S7	1401.03	35.82	LG_M7	1231.02	23.56	LG_L7	1625.71	21.54
LG_S8	1706.40	43.62	LG_M8	1336.00	25.57	LG_L8	2407.79	31.90
LG_S9	1414.98	36.17	LG_M9	1829.13	35.01	LG_L9	1917.48	25.41
LG_S10	1342.80	34.33	LG_M10	1316.21	25.19	LG_L10	1274.51	16.89
LG_S11	1714.66	43.84	LG_M11	1635.95	31.32	LG_L11	2077.04	27.52
LG_S12	1062.07	27.52	LG_M12	2003.25	38.35	LG_L12	1839.12	24.37
LG_S13	1446.03	36.97	LG_M13	1276.30	24.43	LG_L13	2661.13	35.26
LG_S14	1132.64	28.96	LG_M14	1808.86	34.62	LG_L14	1408.82	18.67
LG_S15	1708.35	43.67	LG_M15	1392.46	26.65	LG_L15	1817.21	24.08
LG_S16	1513.82	38.70	LG_M16	1514.93	29.00	LG_L16	2608.41	34.56
LG_S17	1548.93	39.60	LG_M17	1880.26	35.99	LG_L17	918.77	12.17
LG_S18	1337.10	34.18	LG_M18	1414.61	27.08	LG_L18	2261.65	29.97
LG_S19	1126.52	28.80	LG_M19	1549.83	29.67	LG_L19	1599.07	21.19
LG_S20	1171.04	29.94	LG_M20	2009.04	38.46	LG_L20	2015.17	26.70
LG_S21	1727.24	44.16	LG_M21	1473.95	28.21	LG_L21	1753.79	23.24
LG_S22	1167.08	29.84	LG_M22	1307.92	25.04	LG_L22	2538.57	33.63
LG_S23	1752.29	44.80	LG_M23	1794.45	34.35	LG_L23	1435.75	19.02
LG_S24	1111.29	28.41	LG_M24	1477.77	28.29	LG_L24	1975.12	26.17
LG_S25	1464.28	37.43	LG_M25	2096.77	40.14	LG_L25	2180.05	28.88

Appendix E

Effective Thickness of LG for Stress Analysis

In this segment, engineering formulas are presented for the calculation of the effective thickness of laminated glass. Two distinct values for effective laminate thickness can be derived from LG in a specific scenario: (1) deflection-effective thickness, denoted as $h_{\mathrm{ef;w}}$, used in calculations of laminated glass deflection, and (2) stress-effective thickness, denoted as $h_{1,\mathrm{ef};\sigma}$, employed in calculations of laminated glass stress [93]. These effective thickness values are applicable in conjunction with standard engineering formulas or finite element methods to calculate both the deflection and stress of LG under a load. This technique is suitable for 2-ply laminates made from glass plies of both equal and unequal thickness [93, 99].

In accordance with literature [9, 130], transfer shear stress between the glass panes of a rectangular shape of the four-point bend test is introduced as:

$$\Gamma = \frac{1}{1 + \frac{9.6 h_{pvb} E}{G b^2} \frac{h_{g1} h_{g2}}{h_{g1} + h_{g2}}} \tag{E.1}$$

For the circular shape of the ring-on-ring test, the transfer shear stress is introduced as [9]:

$$\Gamma = \frac{1}{1 + \frac{9.6 h_{pvb} E}{G D^2} \frac{h_{g1} h_{g2}}{h_{g1} + h_{g2}}} \tag{E.2}$$

The symbol Γ represents the shear transfer coefficient, indicating the extent to which shear stresses are transferred within the interlayer [130], E is the Young's modulus for glass, h_{pvb} is the thickness of the interlayer, h_{g1} is the thickness of the glass ply 1, h_{g2} is the thickness of the glass ply 2, b represents the width of the LG beam, D is the diameter of the LG plate, G is the shear modulus of the interlayer.

The Young's modulus value of 70,000 MPa and the shear modulus, G, of 12 MPa are assigned to glass and PVB interlayer, respectively.

To calculate the LG deflection, the deflection-effective thickness of LG, denoted as $h_{\mathrm{ef;w}}$, is determined as follows [9, 130]:

$$h_{\text{eff};w} = \sqrt[3]{h_{g1}^3 + h_{g2}^3 + 12\Gamma \frac{h_{g1} h_{g2}}{h_{g1} + h_{g2}} H^2} \tag{E.3}$$

$$H = 0.5\,(h_{g1} + h_{g2}) + h_{pvb} \tag{E.4}$$

To determine the maximum bending stress in glass, the stress-effective thicknesses of LG (one for each ply of glass) are provided as follows [9, 130]:

$$h_{1;\text{eff};\sigma} = \sqrt{\frac{h_{\text{eff};w}^3}{h_{g1} + 2\Gamma\left(\frac{H h_{g2}}{h_{g1}+h_{g2}}\right)}} \tag{E.5}$$

$$h_{2;\text{eff},\sigma} = \sqrt{\frac{h_{\text{eff};w}^3}{h_{g2} + 2\Gamma\left(\frac{H h_{g1}}{h_{g1}+h_{g2}}\right)}} \tag{E.6}$$

The calculation generally applies to the thickest ply, except in cases where different types of glass in the LG have unique allowable stress parameters [93].

The primary factor influencing LG deformation is the complex shear modulus. This modulus serves as a measure of the shear resistance of the plastic interlayer. The effectiveness of coupling and deformation resistance between the two glass plies under loading increases with higher shear resistances [130]. In cases of stiff interlayers, the effective laminate thickness approaches the equivalent monolith thickness ($\Gamma \to 1$), while flexible interlayers lead to the layered limit ($\Gamma \to 0$). An important aspect of using this technique involves accurately determining the interlayer shear modulus [130]. Since all interlayers exhibit viscoelastic properties, it is essential to consider load duration and temperature in relation to the intended use.

To determine the maximum stress ($\sigma_{\max}$) in a LG, engineering formulas for a rectangular beam and circular plate subjected to FPBT and ROR loads, respectively, are utilised by substituting the effective thickness values.

For a rectangular beam subjected to FPBT:

$$\sigma_{\max} = \frac{3PL}{4bh_{1;\text{eff},\sigma}^2} \tag{E.7}$$

For a circular plate subjected to the ROR test:

$$\sigma_{\max} = \frac{3P}{2\pi h_{1;\text{eff},\sigma}^2}\left[(1-\nu)\frac{D_S^2 - D_L^2}{2D^2} + (1+\nu)\ln\frac{D_S}{D_L}\right] \tag{E.8}$$